Correlation between Dynamic Parameters and Device Performance of Organic Solar Cells

Dissertation
zur Erlangung des akademischen Grades
***doctor rerum naturalium* (Dr. rer. nat.)**
in der Wissenschaftsdisziplin Experimentalphysik

Eingereicht an der
Mathematisch-Naturwissenschaftlichen Fakultät
der Universität Potsdam

von

Juliane Kniepert

Potsdam, im September 2015

Published online at the
Institutional Repository of the University of Potsdam:
URN urn:nbn:de:kobv:517-opus4-90087
http://nbn-resolving.de/urn:nbn:de:kobv:517-opus4-90087

Contents

1 Introduction

Modern life is governed by a worldwide increasing energy demand that is currently mainly covered by fossil fuels such as coal, oil or natural gas. Due to limited reserves, a depletion of the fossil resources is inevitable and enforces the search for alternative energy sources that are inexaustibly available. Geothermal, wind and tide energy are some examples for such renewable energy sources. However, by far the greatest and most stable energy source is the sun with a yearly power provision of 23000 TW (see Figure 1.1 for comparison of renewable and conventional energy resources), suggesting that the terrestrial energy future will be solar based.[1]
Solar cells convert the energy provided by the sun directly into electrical power and have the highest potential of any renewable technology.[2] The photovoltaic technology currently dominating the market is based on mono- or polycrystalline silicon with power conversion efficiencies (PCE) up to 25%.[3, 4] However, silicon-based cell modules require a very cost intensive production due to high processing temperatures and large amount of material needed.
Therefore, the alternative material class of organic semiconductors made from conjugated small molecules or polymers, has raised considerable attention. Conductive properties of polymers had already been discovered by Heeger, MacDiarmid and Shirakawa in 1977 awarding them the Nobel Prize in Chemistry.[5] However, the birth of the organic solar cell was a decade later in 1986 when Tang combined an electron donating and an electron accepting material which substantially increased the power conversion efficiency of photovoltaic cells made of organic semiconductors.[6]
Another milestone was the introduction of the bulk heterojunction (BHJ) solar cell consisting of intermixed donor and acceptor small molecules which have been

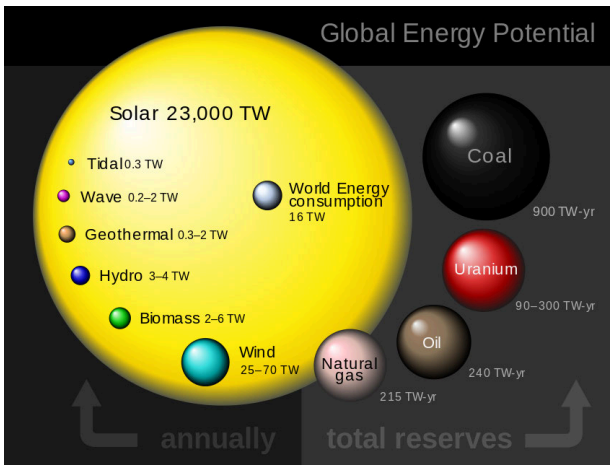

Figure 1.1: Global Energy Potential. Comparison of renewable and conventional energy reserves. For renewables the yearly potential is shown in terawatts (TW) and for the conventional sources the total recoverable reserves are shown in terawatt-years (TW-yr). The volume of the spheres is proportional to the amount of energy they represent. Global solar power of 23,000 TW refers to the earth's total land mass with atmospheric losses taken into account. The worldwide energy consumption was 16 TW in 2009.[1]

coevaporated.[7] With this device architecture the majority of photogenerated excitons were able to reach a donor-acceptor interface within their lifetime, allowing the use of larger layer thicknesses and thereby increasing the absorption efficiency and photocurrent. In 1995 the groups of Heeger and Friend independently demonstrated efficient BHJ devices from polymer-fullerene and polymer-polymer solutions.[8, 9] A few years later the combination of the donor polymer poly(3-hexylthiophene) (P3HT) with the acceptor molecule phenyl-C_{61}-butyric acid methyl ester (PCBM) was shown to achieve an external quantum efficiency (incident photon to electron conversion) of 70%.[10] Morphological optimization of the P3HT:PCBM blends by using high boiling point solvents and thermal annealing pushed the efficiency up to 4.4%.[11] Further efficiency improvements beyond the limit of 5% were achieved by the development of new so called donor-acceptor copolymers, containing electron-rich (donor) and electron deficient (acceptor) subunits. Copolymers show a reduced band gap compared to homopolymers, allowing for increased photon harvesting due to an optimized match to the solar spectrum.

The greatest advantage of all these carbon based molecules or polymers is a comparatively easy chemical synthesis at low temperatures and low costs. Chemical synthesis also enables the fine-tuning of the energetic or optical properties, such as energy levels or the band gap, adjusting to special requirements. Furthermore, most of the compounds are soluble which offers the use of low temperature printing techniques, potentially reducing material consumption and production costs. The flexibility and low weight of the materials compared to inorganic materials open up new possible applications such as solar cells on clothes or bags as mobile cell phone chargers.

The field of organic solar cells has made tremendous progress in the last 15 years (Figure 1.2), even surpassing the 10% benchmark for commercial application with multijunction cell structures.[12, 13] However, for a realistic competition with inorganic solar cells, both the power conversion efficiency (PCE) and the long time stability of the devices need to be further improved. Most of the efficiency improvements in the recent years were based on the development on new donor polymers with optimized energy levels. A fundamental understanding of the exact physical processes leading to photocurrent in organic solar cells only contributed a minor part. However, profound knowledge about the fundamental working principles may enable a more target oriented synthesis of new materials and a faster enhancement of the PCE.

The object of this thesis is to contribute to a deeper understanding of the underlying processes and physical parameters determining the performance of organic solar cells (OSC) and enhance the ability to compete on the market. The output current of solar cells is given by the generation of free charge carriers upon light absorption and their transport to the electrodes in competition to the loss of charge carriers due to recombination. Although, charge carrier generation, recombination and transport individually have been subject to intensive studies in the past years [14–16], there are still inconsistent and conflicting results and conclusions regarding the exact physical mechanisms and, especially, the contribution of the individual

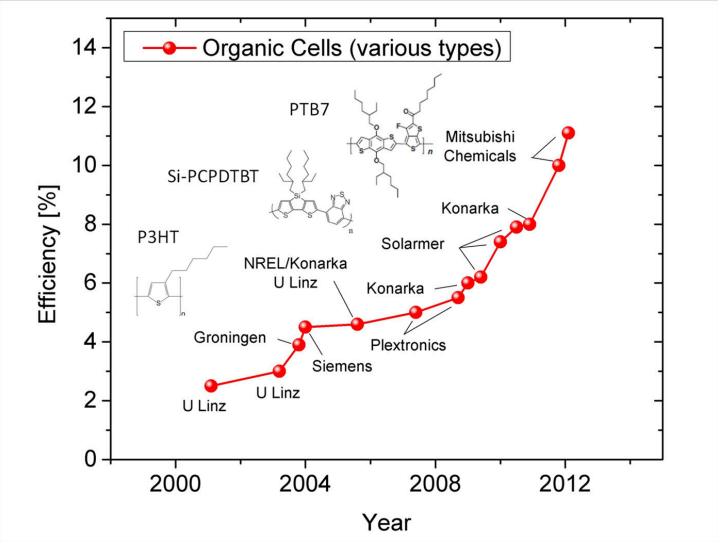

Figure 1.2: Reported timeline for power conversion efficiencies of organic solar cells.[3]

processes to the characteristic current-voltage ($J-V$) output. This can be mainly ascribed to inadequate or missing experimental techniques or to the fact, that not all relevant parameters are considered simultaneously.
As an example, at the beginning of this work, the generation of free charge carriers has been commonly described via an intermediate state of strongly Coulomb bound electron-hole pairs, called *charge transfer* (CT) state. According to this theory the free carrier generation efficiency should strongly depend on the electric field [14], which was justified by a pronounced voltage dependence of the photocurrent found for many devices of the early days. However, the photocurrent of recent high performance OSC shows only a very weak dependence on the voltage similar to inorganic solar cells, which can be soley explained on the basis of losses due to nongeminate recombination of free charge carriers.[17] Also, in some of the generally lower performing polymer-polymer solar cells, fill factors in the order of 70% have been observed.[18] Obviously, efficient generation of free charge carriers is also possible without the need of an electric field. This questions the general role of such an intermediate CT state in the charge generation process.
The critical point is the direct evidence of the effect of an electric field on the free carrier generation process. Transient absorption spectroscopy (TAS) has been used to study the kinetics of CT state formation and dissociation [19–22], however these experiments are usually performed under very high fluences that induce parasitic effects and distort the results. Furthermore, unequivocal distinction of bound charges in CT states and free charge carriers is not straight forward, leading to contradicting results for the same material systems.[19, 21] Beside from TAS measurements, information about the field dependence of CT state splitting was gained indirectly from modelling of $J-V$ curves.[23–25] However, this procedure relies on independent information about the lifetime and spacial extent of CT states which is not readily available.

An elegant way to directly address the field dependence of the free carrier generation and to estimate the relevance of CT states in the generation process is to perform *Time Delayed Collection Field* (TDCF) measurements. TDCF is analogous to a pump-probe experiment with an optical excitation and an electrical probe. In the course of this work, the TDCF method was set up, optimized for improved time resolution and applied for the first time to measure the field dependent free charge generation efficiency in state-of-the-art organic solar cells.
Before the beginning of this work TDCF had only been scarcely reported and a detailed analysis of the method was missing. Therefore, in **Chapter 3** an analytic description of the TDCF photocurrent transients is developed, that allows to analyze the benefits and limits of this method and its applicability under different experimental conditions. In particular, it will be shown that the parameter settings of laser pulse fluence, extraction voltage and delay time have to be carefully chosen to obtain reliable results.
As mentioned before, besides the carrier generation, also the recombination and transport of free charge carriers determines the net current output of OSC. The physical parameters connected to these processes that can be obtained by experiments are the generation rate G, the recombination rate coefficient k or free carrier lifetime τ and the charge carrier mobility μ. In literature often only generation and recombination of charge carriers are investigated and the measured parameters are used to model the $J-V$ characteristics of the devices.[17, 26, 27] However, the transport of the charge carriers may not be ignored. Especially, if the mobilities of electrons and holes diverge, accumulation of the slower charge carrier type hinders the extraction of the faster carrier type. This has an characteristic impact on the shape of the $J-V$ curve that cannot be grasped by considering recombination losses only.
On the other hand, a number of studies concentrate on the transport properties only.[28, 29] These may be able to explain a number of phenomena, however a conclusive picture of the solar cell performance and the charge carrier dynamics can only be obtained when generation, recombination and transport are considered at the same time.
This is examplarily done in **Chapter 4** for two model BHJ systems. P3HT:PCBM has been the most studied model system for a long time and is also sometimes refered to as the 'fruit fly' of organic BHJ solar cells. The blend of PTB7 (thieno[3,4-*b*]thiophene-*alt*-benzodithiophene) with PCBM has reached the record PCE for single junction OSC with 9.2% in 2012.[30] Just recently, even higher efficiencies above 10% have been achieved with a modified version of PTB7.[31] The performance of both systems depends critically on the underlying blend morphology which can be controlled by the preparation conditions. The morphology-performance relation is explored in detail in this chapter and is connected to the charge carrier dynamics. Generation, recombination and transport are primarily investigated by means of TDCF revealing the capability of this method. The results are compared to and complemented by other established techniques.
TDCF is a transient extraction technique that probes the device in a thermody-

namic non-equilibrium state. Therefore, the boundary conditions are different from working solar cells under continuous illumination and bias conditions, which may potentially lead to different results concerning recombination and transport properties. For this reason a new technique is developed and analyzed in **Chapter 5** - *Bias Assisted Charge Extraction* (BACE) - to measure charge carrier densities under steady state conditions more precisely than with established methods. The carrier densities at open circuit conditions can then be used to gain information on nongeminate recombination in the steady state and will be compared to the transient recombination behaviour.
The detailed analysis of charge carrier generation, recombination and transport and the measurement of the relevant parameters provide all ingredients to understand the specific shape of the $J-V$ characteristics of the solar cells. In **Chapter 6** the measured values will be used as input parameters in a numerical device simulation to reproduce the $J-V$ characteristics for a wide range of illumination intensities. The very good agreement between experimental and simulated curves for all investigated devices proves that the measurement techniques and device analysis presented in this work enable a full description of the solar cell characteristics and provide a profound understanding of the dynamic processes in organic solar cells.
The physical framework needed for a discussion of the experimental and analytical results will be provided in **Chapter 2**.

Overall this thesis demonstrates how information on the field dependence of generation, recombination and transport can be accurately obtained from TDCF measurements. Furthermore, a new method (BACE) is introduced for a more precise measurement of charge carrier densities in solar cells under steady state illumination. Altogether, for the first time a conclusive and consistent analysis of all dynamic processes in organic solar cells is provided and enables a fundamental understanding of the performance. This concept may be applied to any new material systems and presents an important contribution to identify the limiting factors of high efficiency organic solar cells.

2 Fundamentals

This chapter presents the most important physical concepts needed for the understanding and discussion of the experimental results of this work. First, the origin of the semiconducting properties of organic π-conjugated systems is discussed to understand how this material class can be utilized in organic solar cells to convert absorbed light into electrical power. This leads to a description of the three fundamental processes in organic solar cells - the generation, recombination and extraction of charges - that will be individually discussed with respect to the most relevant theoretical models in literature. Finally, a short overview of the materials studied in this thesis will be presented along with the most important physical properties that will be important to understand the device performance.

2.1 Organic Semiconductors

The electrical conductive properties of organic, i.e. hydrocarbon based compounds are directly derived from the ability of carbon atoms to form molecules with extended, delocalized π-electron systems. The electronic configuration of a single carbon atom in the ground state is $1s^2 2s^2 2p^2$. However, in chemical compounds, a mixing of the 2s and 2p orbitals leads to new energetic equivalent hybrid orbitals. Most relevant for the conducting properties in organic molecules is the sp^2 hybridization. In this configuration, the 2s and two of the 2p orbitals (p_x and p_y) form three hybrid orbitals which arrange in a plane. The unhybridized p_z orbital stands perpendicular to that plane. Each orbital is occupied with one electron. The overlap of the sp^2 orbitals of two neighbouring carbon atoms (for example in ethylene, see Figure 2.1) leads to the formation of strongly localized covalent σ-bonds along the axis of the nuclei. The overlap of the perpendicular p_z orbitals forms a more delocalized π-bond, leading to a double bond between the carbon atoms.
In an extended chain of carbon atoms the strongly binding σ-bonds build up the backbone of the molecule. Contrary to that, the overlap of the neighbouring p_z orbitals leads to a delocalization of all π-electrons across the entire molecule, which is called *conjugation* and in this way contributes to the electrical conductivity. The electron densities of the π-bonds are located above and below the plane of the sp^2 hybridization and have a much weaker contribution to the molecular binding than the σ-electrons. Therefore, the lowest electronic excitations, where an electron in the highest occupied molecular orbital (HOMO) is excited to the lowest unoccupied molecular orbital (LUMO), are the π-π^* transitions between the highest bonding π-orbital and the lowest antibonding π^*-orbital. The energy difference between the HOMO and the LUMO is defined as the bandgap E_G and determines the semiconducting and optical properties of the molecule (Figure 2.1).
The chain shall now be extended to an infnite number of carbon atoms. In the simplified picture of a *particle in a box*, with the π-electron system being the box and the number of carbon atoms determining the length of the box, the bandgap decreases continuously with increasing conjugation length, approaching 0 for infinite chain lengths. However, according to the *Peierls Theorem* such one dimensional pe-

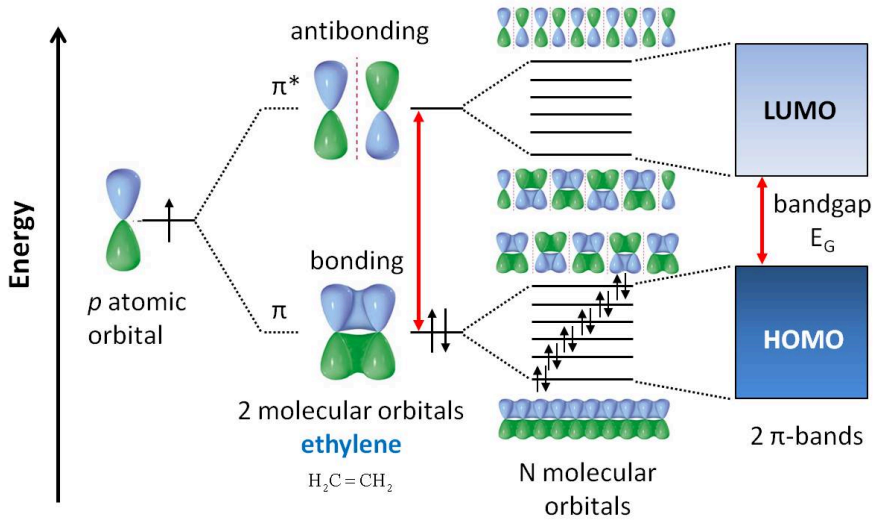

Figure 2.1: Scheme of the formation of molecular π-orbitals in organic conjugated semiconductors. Linear combination of the atomic p_z-orbitals leads to a splitting into bonding π and antibonding π^* orbitals. With increasing number of contributing carbon atoms, the number of states in the orbitals increases and the bandgap decreases until two 'π bands' are formed, denoted as HOMO and LUMO. Due to the Peierls instability they are separated by a finite bandgap in the order of one to three eV.

riodic structures are unstable and a redistribution of the bond lengths leads to a distortion of the symmetry.[32] As a result two bands are formed that are separated by a finite bandgap. The lower energy band is fully occupied with electrons and corresponds to the valence band in inorganic semiconductors. The higher energy band is unoccupied and corresponds to the conduction band.
In reality, in highly extended conjugated systems such as polymers, kinks and twists of the chain as well as chemical defects lead to interruptions of the π-electron system, eventually breaking down the chain into different conjugation lenghts. Therefore, the wavefunctions of the electrons are limited by the size of the conjugated chain segments and the π-electron system of polymers can rather be described in the picture of discrete sites than in the classical semiconducting picture of band transport in inorganic crystals.
The variation of the conjugation lengths in an ensemble of polymer chains leads to different energetic values of the sites. In addition, each site has a slightly different energetic environment due to intramolecular influences such as different conformations, distortions of the chain or substituents and sidechains [33] as well as intermolecular interactions with surrounding molecules. This leads to a broad distribution of the HOMO and LUMO energy values in the semiconductor, denoted as energetic disorder. Since the broadening of the density of states (DOS) distribution is mostly due to statistical effects, it is usually described by a Gaussian or exponential function. The characteristic broadening of the DOS (energetic disorder) becomes relevant for the physical processes if it exceeds the thermal energy kT.

Light Absorption and Exciton Formation in Organic Semiconductors

Since the bandgap of molecular and polymeric semiconductors is in the order of a few eV, excitation of a molecule to a higher energy state is possible through the absorption of light with energy equal to or larger than the bandgap, which promotes one electron from the fully occupied HOMO to the LUMO. However, photoexcitation does not lead immediately to a freely moving electron in the LUMO, as the excited electron still feels the presence of the positively charged hole left behind in the HOMO and forms a quasiparticle, called *exciton*.
In the inorganic counterparts a relatively high dielectric constant ($\varepsilon > 10$) enables effective polarization of the surrounding material leading to a screening of the Coulombic attraction between electron and hole. Therefore, excitons in inorganic semiconductors are loosely bound and delocalized over several lattice constants. This type of exciton is called Wannier-Mott exciton and exhibits a small binding energy, that can usually be overcome by thermal energy at room temperature.
In contrast, in organic semiconductors the dielectric constant is significantly lower, of the order of $\varepsilon \approx 3 - 4$, indicating weak polarizability. Therefore, the Coulombic attraction between electron and hole is not significantly screened and strongly bound Frenkel excitons are formed that are usually localized on the same conjugated chain segment. The binding energy of Frenkel excitons is in the order of 0.5eV - 1eV, by far exceeding the thermal energy.[34] Therefore, no free charge carriers are generated upon light absorption.
As a consequence, an optical excitation cannot be simply described by a transition of an electron from the HOMO to the LUMO, but rather by an exciton state that is lower in energy than the HOMO-LUMO splitting by the binding energy of the exciton. The minimum energy to generate an exciton is sometimes denoted as the *optical* bandgap to differentiate from the energy difference of the HOMO and LUMO states, which is then referred to as the *electrical* or single carrier bandgap.[35] In the course of this work, the term bandgap refers to the electrical bandgap, if not otherwise stated.
The formation of strongly bound Frenkel excitons has important consequences for organic solar cells, where free moving charges upon photoexcitation are needed for generating electric current. The ways to overcome this issue will be discussed in the next section.

2.2 Working Principle of Organic Solar Cells

A solar cell is a device that converts optical power of absorbed light into electrical power which can be extracted from a generated current in the external circuit. As discussed in the previous section, the absorption of light in organic semiconducting materials does not lead to free moving charge carriers contributing to electrical current, but rather to strongly bound excitons.
It was first shown by C. W. Tang [6] that the combination of two organic materials with a sufficient difference in energy levels largely increases the generated photocurrent. This can be understood as follows. Following the convention, the

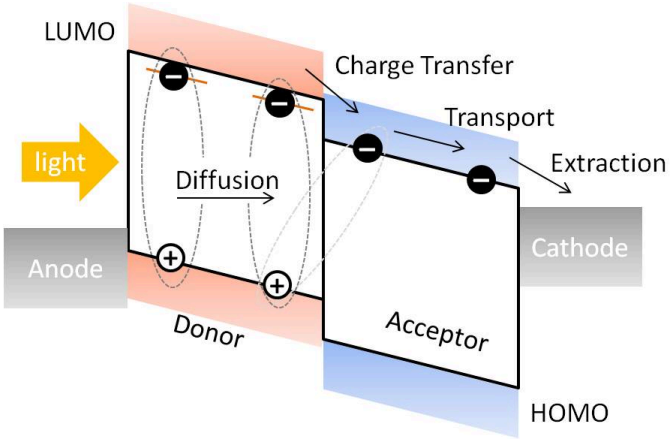

Figure 2.2: Energy diagram of a donor/acceptor heterojunction. Excitons formed in the donor polymer move by diffusion and can be dissociated by a charge transfer of the electron to the acceptor LUMO. Free electrons and holes are transported to the electrodes by drift and diffusion.

semiconductor with the higher LUMO energy is called *donor* as it is able to donate an electron to the material with the lower lying LUMO which is called the electron *acceptor* (see Figure 2.2). Excitons that reach such a donor/acceptor heterojunction by diffusion are dissociated by a charge transfer process. This charge transfer is motivated by a more favorable energetic state for the electron on the acceptor LUMO. The result of the exciton dissociation can either be a more loosely bound charge transfer (CT) state or free electrons and holes, depending on the specific material and energy configurations. The exact mechanism of free charge carrier generation and the role of the intermediate CT state in this process will be discussed in more detail in the next section.
There are several possible arrangements of the donor and acceptor materials. The obvious one is a simple bilayer device architecture providing a defined model system. However, due to the short lifetime of singlet excitons in the order of 1 ns [36, 37], the layer thickness of the absorbing materials is limited by the exciton diffusion length which is typically in the order of 5 - 15 nm in disordered organic materials.[38–40] The device architecture studied in this work is the bulk heterojunction (BHJ) solar cell, where both components interpenetrate each other leading to a spatially distributed interface. This morphology is for example implemented by spin coating a polymer-fullerene blend or by coevaporating conjugated small molecules. The advantage of the BHJ is a very efficient exciton dissociation over the whole extend of the solar cell, which consequently leads to a higher extractable photocurrent.
The most important parameter of a solar cell is its power conversion efficiency (PCE) which is defined as the ratio of the maximum extractable electrical power density P_{el} and the power density of the incident light P_{L}. The extractable electrical power density P of a solar cell depends on the applied voltage V:

$$P = V \times J(V), \tag{2.1}$$

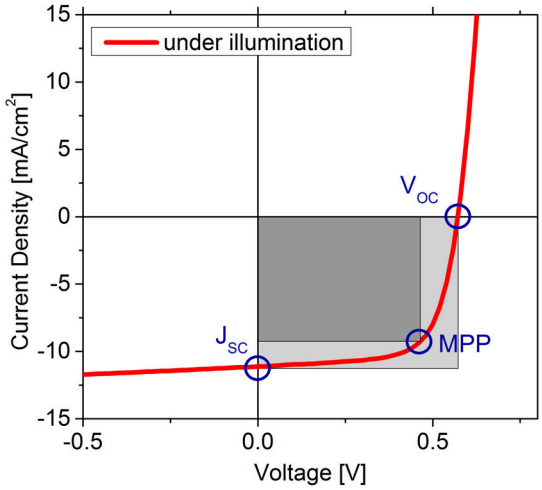

Figure 2.3: $J-V$ curve under illumination of a typical P3HT:PCBM solar cell. Marked are the points of zero current (V_{OC}), zero bias (J_{SC}) and the maximum power point (MPP) with V_{MPP} and J_{MPP}.

with J being the generated current density. Hence, the performance of a solar cell is best characterized by the current density versus voltage ($J-V$) curve under illumination, which is examplarily shown in Figure 2.3. The important parameters in this figure are the short circuit current density J_{SC}, defined as the current density measured at 0 V applied bias, and the open circuit voltage V_{OC}, defined as the voltage at which no net current is flowing in the external circuit. The PCE of the solar cell is then calculated by:

$$PCE = \frac{P_{\mathrm{el}}}{P_{\mathrm{L}}} = \frac{V_{\mathrm{OC}} \times J_{\mathrm{SC}} \times FF}{P_{\mathrm{L}}}. \tag{2.2}$$

The fill factor FF is defined as the ratio of the maximum extractable power (product of current density and voltage at the maximum power point MPP, dark grey square in Figure 2.3) and the product of J_{SC} and V_{OC} (light grey square):

$$FF = \frac{V_{\mathrm{MPP}} \times J_{\mathrm{MPP}}}{V_{\mathrm{OC}} \times J_{\mathrm{SC}}}. \tag{2.3}$$

The fill factor describes the deviation from an ideal rectangular J_V curve and is therefore a measure of the quality of the solar cell.
To achieve the best reliable comparison between different solar cells, it is agreed that the $J-V$ characteristics are taken under the same illumination conditions, which are 100 mW/cm^2 under an AM1.5G spectrum with an active layer temperature of 25°C. Under steady state bias and illumination conditions the photogenerated free charge carriers in the device are either extracted to the external circuit or they recombine non-geminately in the layer and are lost for photocurrent. Therefore, at each point of the $J-V$ curve the following rate equation is valid:

$$J = e \int (R-G)\mathrm{d}x, \tag{2.4}$$

with G being the free carrier generation rate and R the non-geminate recombination rate. The current density J implies the transport properties of charge carriers. Hence, for a complete picture of the device physics of organic solar cells a fundamental understanding of the origin and magnitude of all involved rate constants is essential and represents the main purpose of this thesis. The underlying physics of the involved processes leading to photocurrent generation will be discussed in the following sections.

2.3 Charge Generation and Geminate Recombination

In the previous two sections it has been established that the primary photoexcitations in organic semiconductors are strongly bound excitons and that the combination of a donor and an acceptor component is necessary to dissociate the excitons via a charge transfer of the electron. Although being highly interesting and crucial for the field of organic solar cells, the charge transfer process itself is not subject of this thesis. Charge transfer of an electron from an excited donor site to an acceptor site usually happens on a time scale below 100 fs [41, 42] and could therefore not be resolved with the experimental techniques presented in this work. Hence the discussion is mainly focused on the processes following the charge transfer and leading to free extractable charge carriers.

Including the excited donor state (D*) there are four relevant energetic states involved in the charge generation process, mainly characterized by the separation distance of the electron and the hole, see Figure 2.4. Immediately after charge transfer from the donor site to an acceptor site, the electron populates a charge transfer state (CTS) that is still radiatively coupled to the ground state (GS) and therefore electron and hole are still in close vicinity, however in general less tightly Coulomb bound than the exciton. The existence of the CTS is confirmed by the appearence of sub bandgap absorption and emission features in blends of donor and acceptor materials [43–45] and by electron spin resonance measurements.[46–49] The quasiparticle connected to the CTS is sometimes called charge transfer exciton [50] or geminate pair [51], although both concepts are strictly valid only for tightly bound electron-hole pairs that originate from the same excitation. The dissociation of the CTS into free charge carriers is in direct competition to geminate recombination to the GS with rate k_f.

The energetic state connected to spatially-separated electrons and holes with negligible Coulomb interaction (free polarons) is the charge separated state (CSS). Some authors propose an additional bound polaron state (BPS) as an intermediate state between CTS and CSS, associated with loosely bound polaron pairs.[52] The BPS is a Coulomb bound electron-hole state, however in contrast to the CTS it is not radiatively coupled to the ground state and can therefore not be directly excited. This state has been observed in blends of amorphous donor and acceptor materials and exhibited a much longer lifetime (on the 100 ns time scale) compared to the CTS (τ_{CTS} <20 ns).[52]

The exact energies of the involved states are hard to access. In general they depend

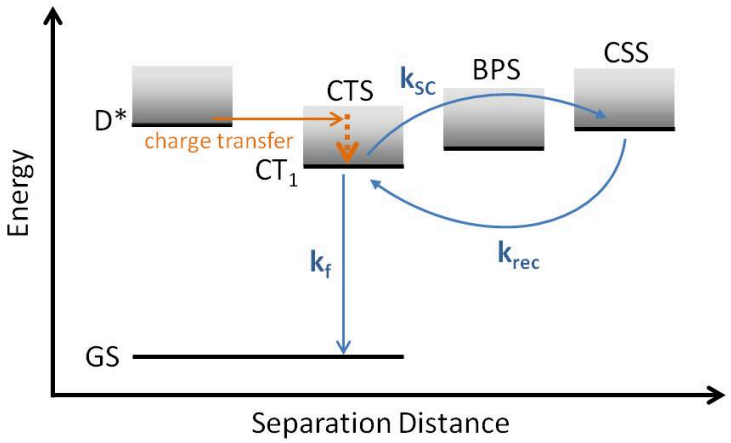

Figure 2.4: Energy diagram with the relevant states at a D/A interface. Upon photon absorption the electron populates an excited donor state (D*). Charge transfer into an (excited) charge transfer state (CTS) is indicated by the horizontal arrow and subsequent relaxation to the lowest lying CT_1 is indicated by the dotted arrow. Charge generation proceeds via dissociation of the CTS into a charge separated state (CSS). In some blends a bound polaron state (BPS) as an intermediate state has been observed. Also shown in blue are the relevant rates k_f, k_{SC} and k_{rec} for the Braun-Onsager model.

on domain size, purity and crystallinity of the donor and acceptor phases and the morphological structure directly at the interface. However, there is clear evidence that the relative energetic positions of the involved states significantly determine the efficiency of free charge generation. Figure 2.4 depicts an example of a strongly bound CTS and a relative large energetic offset (> kT at room temperature) between CTS and CSS. In this case an additional electric field is necessary to fully separate electron and hole and prevent geminate recombination back to the ground state. In fact, the electric field dependence of free carrier generation has been widely proposed as the key factor limiting the performance [53], since especially the early stage organic solar cells mostly showed low fill factors and concomitant strongly field-dependent photocurrents. A theoretical model to describe the field-dependent separation process via a BPS was first developed by Onsager in 1930s [54] and was later extended to the explicit existence of a CTS by Braun.[14]

2.3.1 Braun-Onsager-Model

The model originally proposed by Onsager calculates the probability that two oppositely charged ions in a weak electrolyte, undergoing Brownian random motion, will escape their Coulomb attraction and generate free charges. The ion pair is assumed to thermalize at a certain distance a (thermalization length). The recombination of such a thermalized geminate pair back to the ground state is defined as geminate recombination and directly competes with its dissociation. Here, the presence of an electric field lowers the Coulomb potential barrier in the downfield direction and thereby enhances the fraction of escaping ions. This model has been applied to

explain the field dependent dissociation of photogenerated bound polaron pairs in organic semiconductors. However, it uses the boundary condition that the geminate pair irreveribly disappears once the separation distance becomes zero, which led to unrealistic large thermalization lengths in some cases.
Braun modified the model by introducing a defined CT state in donor-acceptor systems with a finite lifetime. The possible pathways from the CT state are sketched in Figure 2.4. It can either dissociate into free charge carriers with an electric field (and temperature) dependent rate constant k_{CS} or decay to the ground state with the geminate recombination rate constant k_f. However, during the lifetime (f_f^{-1}) of the CT state, many attempts to dissociate may occur and subsequent (nongeminate) recombination might regenerate the CT state with a rate constant k_{rec}. The probability for the CTS to completely dissociate into spatially separated charges is then given by the ratio of the respective rates (Figure 2.4):

$$P(E,T) = \frac{k_{\mathrm{CS}}(E,T)}{k_{\mathrm{CS}}(E,T) + k_f}, \tag{2.5}$$

where the field-dependent dissociation rate constant k_{CS} is given by:

$$k_{\mathrm{CS}}(E,T) = \nu \exp[-\Delta E/kT](1 + b + \frac{b^2}{3} + \frac{b^3}{18} + ...), \tag{2.6}$$

with the separation attempt frequency

$$\nu = \frac{3\langle\mu\rangle e}{4\pi\langle\varepsilon\rangle\varepsilon_0 a^3}, \tag{2.7}$$

and the effective field parameter

$$b = \frac{e^3 E}{8\pi\langle\varepsilon\rangle\varepsilon_0 (kT)^2}, \tag{2.8}$$

where $\langle\mu\rangle$ is the spatially averaged sum of the electron and hole mobilities, $\langle\varepsilon\rangle$ is the spatially averaged dielectric constant and the thermalization length a denotes the initial distance between electron and hole. The dissociation barrier ΔE is given by the Coulomb binding energy of the charges after thermalization and is usually found to be of the order of 0.1 to 0.5 eV.[53, 55–58]
Figure 2.5 shows the electric field dependence of the CT state dissociation probability $P(E)$, which is directly proportional to the yield of free charge carriers, determined for different thermalization lengths a. For the applied parameters, the dissociation probability strongly depends on the thermalization distance. However, at low fields the yields are all low and efficient free charge generation is predicted only for significant electric fields in the order of $\sim 10^8$ V/m, corresponding to an applied voltage of 10 V for a 100 nm thick device. These low predicted charge generation yields in the relevant field regime of organic BHJ solar cells ($\sim 10^6 - 10^7$ V/m) are in contradiction to recent developments of high efficiency OSC with fill factors exceeding 70% and internal quantum efficiencies approaching 100%.[30, 59] Interestingly,

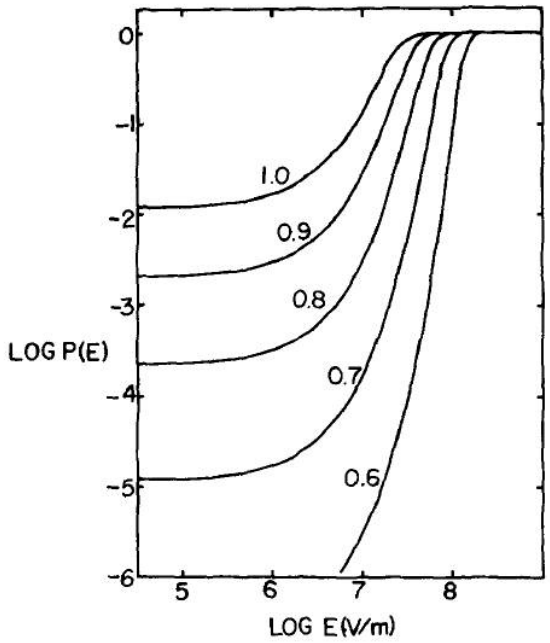

Figure 2.5: Electric field (E) dependence of the CT state dissociation probability (P) for different thermalization lengths a in nm. From Ref. [14]

Blom et al. were able to successfully describe the $J - V$ characteristics of several polymer:fullerene devices utilizing a numerical model based on the Braun-Onsager theory. However, this analysis required CTS lifetimes in the order of 1 μs, in case of annealed P3HT:PCBM even 50 μs, to match the relatively high photocurrents at low fields.[23–25] These are in sharp contrast to CT lifetimes gained from photophysical data for donor/acceptor systems, which are of the order of several picoseconds to a few nanoseconds.[21, 50, 60–63] Inconsistencies may originate from approximations within in the Braun-Onsager model. Most importantly, the model assumes point charges in an effective, homogeneous and isotropic medium and neglects any electronically or vibronically excited ('hot') CT states. Also the explicit morphological structure of the interface is not taken into account by the Braun-Onsager theory. Therefore, the applicability to phase separated donor-acceptor blends is questionable and the influence of charge delocalization, for example in crystalline domains, on the dissociation efficiency is rather unclear and currently strongly debated. Recently, alternative models (see next section) have been suggested to explain the high quantum efficiencies despite the existence of thermalized CT states.

2.3.2 Hot CTS versus relaxed CTS mediated charge generation

Conservation of energy requires that charge transfer mainly occurs into electronically or vibronically excited ('hot') CT states. Those higher lying CT levels have been proposed to show a higher degree of delocalization compared to the lowest lying, thermalized CT_1 state, which might enhance the probability of charge

dissociation.[42, 64, 65] Therefore, a charge generation model has been suggested whereby the excess (thermal or electronic) energy of electrons injected into the fullerenes enables them to overcome their Coulomb attraction to the polymer polaron, thereby avoiding forming a strongly bound, relaxed CTS.[66, 67] Consistent with this theory, correlations have been found between the free polaron yield and the energetic driving force, defined as $\Delta E_{CS}^{\text{eff}} = E_{D*} - E_{CSS}$.[52] These findings suggest that $\Delta E_{CS}^{\text{eff}}$ is the primary determinant of the initial charge generation efficiency. However, for this mechanism to be efficient, charge separation from a hot CTS needs to proceed much faster than vibrational relaxation within the CT manifold. Indeed, recent ultrafast pump-probe experiments [42, 64, 68] observed efficient charge separation on timescales (<100 fs) much faster than previously reported for CTS thermalization (ps-range).[69] This was taken as evidence that hot CTS are the main precursors of free charge carriers.

In contrast, strong evidence was found that charge generation is as efficient from lower energetic CT states as for higher energy excitations.[70, 71] The field dependence and absolute value of the quantum yield in these measurements showed little dependence on whether or not the initially generated excited state had energy in excess of the CT_1. Even though ultrafast transient spectroscopy has shown the existence of higher energy, faster dissociating pathways, quantum efficiency measurements on working solar cells suggest that hot CTS are not responsible for most of the generated free charge carriers. Rather, due to ultrafast relaxation within the CT band, most photoexcitations into higher energy states reach thermal equlibrium with CT_1 before being dissociated and energy released upon exciton split-up does not considerably promote free carrier generation.

In particular, for blends of P3HT:PCBM it has been shown, that the internal quantum efficiency measured by direct photocurrent spectroscopy [43] and the charge carrier dynamics measured by photo-CELIV [72] are independent of the excitation wavelength over a wide range of photon energies, including those that directly excite low lying CT states. These results indicate that relaxed and not hot CTS mediate the conversion between excitons and free charge carriers in these blends.

Yet, internal quantum efficiencies above 80% have been measured for P3HT:PCBM. [43] Apparently, the thermalized CT_1 does not neccessarily have to be strongly bound but can also be sufficiently delocalized and easily dissociate. It has been proposed that free charge generation proceeds via split-up of low lying CT states, irrespective of the initial excitation energy, and that the ability of the CTS to split up is rather dictated by the energetic offset between the relaxed CTS and the CSS.[71] Accordingly, the generation efficiency decreases and becomes field-dependent if the energy difference between CTS and CSS becomes large, which is related to a binding energy of the relaxed CTS exceeding thermal energy.

The models and results discussed in this section are subject of current research and are highly debated in literature. They are in contradiction to the conventional Braun-Onsager formalism as they predict, that the existence of charge transfer states as intermediate precursors do not necessarily limit efficient generation of free charge carriers. The clarification of the exact charge generation mechanism will not be

considered in detail in this work. Instead, this thesis is rather focused on an overall understanding of the solar cell performance. Independent of the exact generation process, the experimental and analytical methods developed in this work are able to distinguish whether the free carrier generation yield is dependent or independent of an electric field and whether the device performance is limited by the free carrier generation or other processes. Identification of the limiting processes is highly important for a systematic device improvement.

Throughout this work, whenever the term *generation* or *generated charge* is used, the whole process from light absorption to fully dissociated, free moving electrons and holes is considered. After successful charge generation, the free charge carriers can either be extracted through the device electrodes or they are lost due to nongeminate recombination back to the ground state. These processes, each of them also potentially dependent on electric field, temperature and morphology will be discussed in the following sections.

2.4 Non-geminate Recombination

Recombination describes the relaxation of an excited electron back to the ground state. The term *non-geminate* recombination denotes the recombination of free, statistically independent, electrons and holes. Here, the electron needs to approach a hole, i.e. a vacant state in the HOMO, within the vicinity of the Coulomb capture radius which is defined as the distance where thermal energy and Coulomb attraction are equal.
The recombination process is mainly characterized by its reaction order. Depending on the number of particles involved, it is distinguished between monomolecular (first order), bimolecular (second order) and higher order recombination processes.

2.4.1 Monomolecular Recombination

As suggested by the name only one particle at a time, for example a quasiparticle like an exciton or a geminate pair, is involved in the recombination process. For statistical reasons the recombination rate then depends linearly on the particle concentration n:

$$\frac{dn}{dt} = -k_{\mathrm{MR}} n, \tag{2.9}$$

with k_{MR} being a monomolecular rate constant. The temporal evolution of the particle density then follows an exponential function:

$$n(t) = n_0 \exp[-\frac{t}{\tau}], \tag{2.10}$$

with the time constant $\tau = k_{\mathrm{MR}}^{-1}$.
While monomolecular recombination kinetics are typically observed for excitons and CT states, they are also seen if statistically independent charge carriers recombine via one recombination center. In organic semiconductors a recombination center

can for instance be a deep state occupied by an electron, which recombines with a mobile hole. This trap assisted recombination was first described by Shockley, Read and Hall (SRH) for inorganic semiconductors.[73, 74] In thermal equilibrium of electron and hole capture and release, the recombination rate R_{SRH} is given by:

$$R_{\mathrm{SRH}} = \frac{C_e C_h N_t np}{C_e n + C_h p}, \tag{2.11}$$

where C_e and C_h are the electron and hole capture coefficients, respectively, N_t is the density of trap states and n and p are the photogenerated (or injected) electron and hole densities. Equation (2.11) assumes that the photogenerated (injected) carrier densities are much higher than the intrinsic carrier density. Although SRH recombination is most important in inorganic semiconductors, it has also been occasionally observed in organic solar cells.[75, 76]

2.4.2 Bimolecular Recombination

If recombination involves two free charge carriers it is called bimolecular recombination, which is by far the most relevant loss process in organic solar cells. In case of photogenerated charge carriers, electron and hole densities are approximately equal ($n = p$) and the recombination rate depends on the second power of the carrier density n:

$$\frac{dn}{dt} = -k_{\mathrm{BR}} n^2, \tag{2.12}$$

where k_{BR} is the bimolecular rate coefficient. In low mobility materials such as most organic semiconductors, the rate limiting step is not the recombination event itself, but the probability of two oppositely charged carriers to find each other. This process was first described by Langevin [77] for the recombination of ions in gases and is often applied to free polaron recombination in organic semiconductors. According to this theory recombination inevitably takes place as soon as the distance between the positive and the negative charge falls below the Coulomb capture radius $r_C = e^2/4\pi\varepsilon\varepsilon_0 kT$. This assumption is valid if the mean free path of the charge carriers is lower than the Coulomb capture radius. The recombination is then viewed as the drift of the two charges in their mutual Coulomb field. Following the derivation of Pope and Swenberg [34] the Langevin recombination coefficient k_L is given by:

$$k_L = k_{\mathrm{BR}} = \frac{e}{\varepsilon\varepsilon_0}(\mu_e + \mu_h). \tag{2.13}$$

Although this theory was originally developed for homogeneous isotropic media, it is often applied to describe recombination in donor/acceptor blends, where electrons and holes are each confined to separated material phases and recombination occurs only at the interface. Not surprisingly, in most cases deviations are found in form of a reduced Langevin recombination coefficient.[18, 78–81] Sometimes a reduction factor ξ is introduced according to:

$$k_{\mathrm{BR}} = \xi k_L, \tag{2.14}$$

which is typically found of the order of 10^{-1} to 10^{-3}.[82, 83] However, the exact value of the reduction factor critically depends on the specific material combinations and preparation conditions. Up to now it has not been possible to predict the reduction factor for a given BHJ device. The most common approaches are to consider the lower charge carrier mobility instead of the sum of both mobilities [84] or energy activated recombination due to spatial fluctuations in the potential landscape [85]. Other effects, like energy gradients due to a more amorphous morphology close to the interface that potentially lead the charge carriers away from the interface and hinders recombination, may also influence this prefactor.[86]
As Langevin theory does not apply well to the studied BHJ solar cells, in this work the general bimolecular recombination coefficient k_{BR} will be used to compare the recombination kinetics for different systems.

2.4.3 Higher Order Recombination

In some cases a rate dependence on carrier density of order α higher than two has been observed [87, 88] in the general form:

$$\frac{dn}{dt} \sim n^{\alpha}. \tag{2.15}$$

The involvement of more than two charge carriers in the predominant loss mechanism seems highly improbable for organic materials. In inorganic semiconductors an Auger-type recombination process leads to trimolecular recombination with $\alpha = 3$. In this case, one electron in the conduction band recombines with a hole in the valence band and the released energy is taken up by a third-particle electron in the conduction band, which is excited to an higher energy level.[34] After the interaction, the third electron either thermalizes back to the band edge or, if close enough to the surface, leaves the crystal. This process is only significant for very high carrier densities.
For organic devices it has been proposed that the bimolecular rate constant k_{BR} itself depends on the carrier density.[87] Although recombination is still bimolecular in this case, in experiments a higher order is measured. Following Langevin theory, k_{BR} depends on the carrier mobilities and these may in highly disordered systems potentially depend on the carrier density (see next section). Other factors, such as a inhomogeneous charge carrier distribution, have also been reported to lead to apparent higher recombination orders [89, 90] and will be discussed in more detail in Chapter 5.

2.5 Charge Transport

Charge carriers that have successfully escaped geminate and non-geminate recombination may be extracted at the electrodes to contribute to the photocurrent in the external circuit. However, the critical step is the transport of the charge carriers from the place of generation to the electrodes. The key parameter of charge transport is the charge carrier mobility μ. Considering drift in the influence of an

effective electric field, the mobility is defined as the ratio of the drift velocity v and electric field E:

$$\mu = \frac{v}{E}. \tag{2.16}$$

Perfect conjugation of infinite polymer chains would suggest a band-like transport along the chains as found in inorganic crystalline semiconductors. However, it has been pointed out in Section 2.1, that disruptions and defects break down the chain into smaller conjugated units leading to an ensemble of localized sites with slightly varying energetic levels and distances. Due to the finite conjugation lengths, the charge carriers are constrained in space and the concept of band transport is not applicable. As a consequence, charge carrier mobilities in organic semiconductors are typically several orders of magnitude lower than in inorganic semiconductors and present a limiting factor to device performances.
A number of models exist that relate the mobility to macroscopic parameters such as electric field, temperature and charge carrier density. Among these, the two most relevant for polymeric semiconductors, the Gaussian disorder model (GDM) and the multiple trapping and release (MT) model, will be discussed in more detail.

2.5.1 Gaussian Disorder Model

The GDM considers transport of charges via thermally activated tunneling, i.e. *hopping*, between the localized sites. The hopping rate ν_{ij} between two sites i and j with energies E_i and E_j can be described with the Miller-Abrahams [91] model:

$$\nu_{ij} = \nu_0 \exp(-\gamma r_{ij}) \begin{cases} \exp(-\frac{E_j - E_i}{kT}) & \text{if } E_j > E_i \text{ (upward hop)} \\ 1 & \text{if } E_j < E_i \text{ (downward hop),} \end{cases} \tag{2.17}$$

where ν_0 is the attempt to hop frequency, r_{ij} is the distance between the sites and γ is the inverse localization radius. The first exponential is a measure of the electronic wavefunction overlap and describes the tunneling contribution of the hopping process. As expected the hopping rate decreases exponentially with increasing intersite distance. For jumps upward in energy an additional Boltzmann factor is used describing the thermally activated process. Increasing temperature therefore increases the hopping probability.
To account for the spread in energies and distances of the transport sites, Bässler and coworkers included Gaussian distributions for the site energies and hopping distances, with characteristic widths σ and Σ.[16] σ and Σ are also often denoted as the energetic and spatial disorder parameters, respectively.
Application of these assumptions in Monte Carlo simulations yielded an empirical expression describing the charge carrier mobility as a function of temperature (T) and electric field (E):

$$\mu(E,T) = \mu_0 \exp\Big(-(\frac{2\sigma}{3kT})^2 + C\Big[(\frac{\sigma}{kT})^2 - \Sigma^2\Big]\sqrt{E}\Big) \text{ for } \Sigma \geq 1.5, \tag{2.18}$$

where μ_0 is the zero field and infinite temperature mobility and C is an empirical constant. The GDM successfully predicts a number of experimental observations,

such as a $1/T^2$ temperature dependence of mobility, rather than an Arrhenius type $1/T$ dependence, and a Poole-Frenkel like field dependence of the mobility:

$$\mu(E) \sim \exp(\beta\sqrt{E}) \tag{2.19}$$

It should be noted that according to this model also a negative dependence of mobility on electric field is possible, if $\Sigma > \sigma/kT$, i.e. if spatial disorder is larger than energetic disorder.
Notably, Equation (2.18) does not account for a dependence of mobility on charge carrier density, which has, however, been occasionally observed.[92, 93] Intuitively, charge carriers in the tail of the Gaussian distribution find only a limited number of unoccupied sites accessible by hopping, which drastically reduces the charge carrier mobility. As the density of states (DOS) is filled by an increasing charge carrier density more charge carriers occupy sites close to the center of the DOS where a larger number of sites in energetic and spatial vicinity are available. Thus, the average mobility might increase with increasing carrier density.
In a similar approach to the GDM, Pasveer et al. simulated and parameterized charge transport with a hopping master equation, yielding an empirical description, sometimes called extended GDM.[94] This model predicts an explicit density dependence of the mobility, however due to the rather large number of microscopic parameters it is difficult to apply for data analysis.

2.5.2 Multiple Trapping and Release Model

An alternative way to describe the charge transport in disordered systems is the MT model adopted from amorphous inorganic semiconductors. In this model the so-called mobility edge separates transport states with rather high carrier mobility from localized states which act as traps, see Figure 2.6. In contrast to the GDM, hopping between the localized trap states is not considered in the MT model. While charge carriers in the band-like states move freely with a constant mobility μ_0, trapped charges are immobile ($\mu = 0$) and do not contribute to transport. Only thermal activation back to the transport band, i.e. detrapping, revives the charge carriers for transport. Thus, the average drift mobility is controlled by the trapping

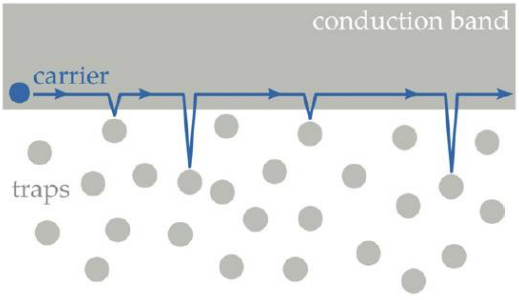

Figure 2.6: A sketch of the multiple trapping process. Figure taken from [95].

and detrapping processes and can be written as [96, 97]:

$$\mu_D = \mu_0 \frac{n_{\text{free}}}{n_{\text{total}}} \tag{2.20}$$

Remarkably, both the GDM and the MT model predict a time dependent mobility after photoexcitation, as the charge carriers thermalize into the deeper lying states of the underlying DOS. This effect has to be taken into account when comparing experimental results from transient and steady state measurements, as they might potentially reveal different results for the mobility and recombination behaviour.
At this point it might be interesting to note that the MT model has also been used to describe bimolecular recombination in the presence of an exponential trap distribution.[98] At long times the diffusional encounter of electrons and holes becomes limited by trapping and detrapping of the charges and the recombination dynamics follow a power law:

$$n(t) \sim t^{-\alpha}, \tag{2.21}$$

where is exponent $\alpha = T/T_0$ is determined by the temperature T and the charateristic temperature of the trap distribution T_0. In the case of trap limited recombination α is smaller than one and gives information about the trap distribution.

2.5.3 Space Charge Limited Currents

It has been shown that charge carriers can move via hopping between localized states or by coherent band transport in the presence of a trap density. However, the microscopic structure is not the only factor controlling the charge transport in semiconducting devices. If a voltage is applied to the device, charge carriers move from one electrode to the other in the influence of the external electric field. However, if the injected charge in a unipolar device becomes equal or even exceeds the charge on the electrodes the applied electric field is screened and the current drawn between the electrodes is limited by the forming space charge. In this case the current density, also known as *space charge limited current* (SCLC) density can be expressed by the Mott-Gurney law [99, 100]:

$$J(V) = \frac{9}{8} \varepsilon \varepsilon_0 \mu \frac{V^2}{d^3}. \tag{2.22}$$

Since the current depends only on the voltage V, the mobility μ and the active layer thickness d, the evaluation of $J(V)$ curves with Equation (2.22) can be used in a straight forward way to determine the charge carrier mobility in organic layers.
Importantly, Equation (2.22) is only valid, if the current is truly limited by the space charge in the device and not by the injection of charges at the contact, i.e. if the injecting contacts are Ohmic and provide an infinite number of charge carriers. This implies that the electric field at the injecting contact is completely screened ($E = 0$). This important requirement can be confirmed by varying the device thickness to verify the $1/d^3$ dependence.

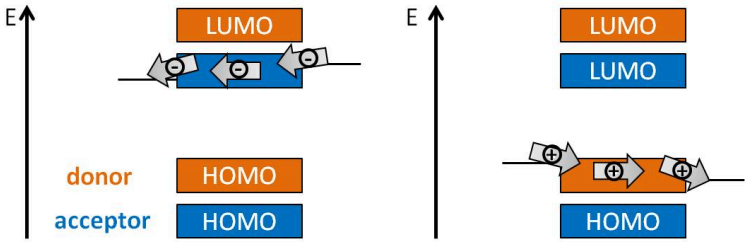

Figure 2.7: Schematic band diagram for single carrier devices: (left) electron-only and (right) hole-only.

Furthermore, Equation (2.22) has been developed for unipolar devices, i.e. only one charge carrier type (electrons or holes) is present in the device. This can be realized by the choice of specific electrodes matching the LUMO or HOMO of the material to measure electron or hole transport, respectively (see Figure 2.7). As a consequence, the electrodes for the mobility measurements are different from the electrodes used for solar cell devices, where efficient injection and extraction of both carrier types is desired. It cannot be ruled out that the choice of electrodes could influence the microscopic layer morphology and with that the macroscopic transport properties.[101]
Remarkably, the Mott-Gurney law predicts a quadratic dependence of current density on voltage. However, in many cases a higher order dependence has been observed. Two models have been proposed to account for the higher order dependence. First, Mark and Helfrich considered trap-limited transport in the presence of an exponential trap distribution, similar to the MT model approach, which revealed the following expression for the current density [99, 100]:

$$J(V) = e\mu N_f \left(\frac{2l+1}{l+1}\right)^{l+1} \left(\frac{l}{l+1}\frac{\varepsilon\varepsilon_0}{eN_t}\right)^{l} \frac{V^{l+1}}{d^{2l+1}}, \tag{2.23}$$

where N_f is the effective density of states in the transport band, N_t is the total trap density and $l = E_t/kT$ with E_t as the characteristic energy of the exponential trap distribution. For mobility measurements Equation (2.23) cannot be straight forwardly used, since the total trap density and the exact shape of the trap distribution are usually not known and have to be determined with independent measurements. On the other hand, the assumption of an explicitly field-dependent mobility also leads to a slope higher than 2 in the log$J$-log$V$-plot, especially at higher voltages [102]:

$$J(V) = \frac{9}{8}\varepsilon\varepsilon_0\mu_0 \exp(0.89\beta\sqrt{E})\frac{V^2}{d^3}. \tag{2.24}$$

Here, μ_0 is the zero-field mobility and β is the Poole-Frenkel factor, describing the field dependence of the mobility.
Practically, it is very hard to distinguish between those two processes from simple current-voltage measurements and additional information from independent measurements has to be taken into account.

2.6 Charge Carrier Injection

Besides charge generation, recombination and extraction, the injection of charge carriers from the electrodes into the device is also an important process in organic solar cells and influences the performance. Although charge injection is not explicitly investigated in this work, it has a significant influence on the steady state carrier density in the dark and hence plays an important role in the transient as well as steady state recombination dynamics of photogenerated charge carriers. Therefore, the most important concepts of charge injection shall be briefly discussed.
The ideal condition for charge injection are Ohmic contacts, i.e. charge carriers can freely enter the organic layer in the absence of an energetic barrier. However, in many cases an offset is found between the electrode Fermi level and the HOMO or LUMO band edge of the semiconductor, which is then defined as the energetic injection barrier Φ_B (Figure 2.8 left).
Two relevant models have been developed for inorganic semiconductors to describe the injection limited dark current through the device. The Richardson-Schottky model considers injection of single carriers from the metal into the semiconductor via thermionic emission across an effective barrier Φ_{eff} that is reduced by the image charge potential and the applied electric field (Figure 2.8 right).[103] The resulting injection current follows:

$$J = A_G T^2 \exp(-\frac{\Phi_{\text{eff}}}{kT}), \tag{2.25}$$

where A_G is the effective Richardson constant and T is temperature. According to this expression the injection efficiency increases with decreasing barrier height. Remarkably, the Boltzmann approximation instead of the Fermi-Dirac distribution is used to describe the temperature and barrier dependence of the thermally injected electrons which indirectly implies high barriers ($\Phi_B \gg kT$).
In contrast, the Fowler-Nordheim model considers quantum dynamic tunneling through the barrier, that is usually approximated with a triangular shape.[104] Here, the electric field mainly reduces the tunneling distance (Figure 2.8 right). The resulting

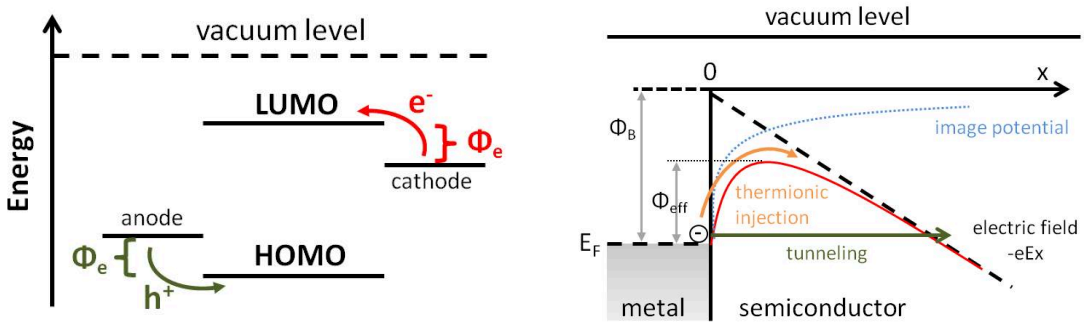

Figure 2.8: Left: Definition of the electron and hole injection barriers, Φ_e and Φ_h, respectively. In case of a broadened DOS due to energetic disorder, the definition of the barriers is more problematic. Right: Lowering of the effective injection barrier Φ_{eff} due to the image potential and applied electric field.

injection current has a similar dependence on the barrier height as Equation (2.25), however the dependence on temperature and electric field differs.
Both models were deloped for band transport with high carrier mobilities and do not account for the specific properties of organic semionductors such as molecular structure and disorder. Modifications by Scott and Malliaras consider back recombination of charge carriers at the interface via hopping in the image potential. This is rationalized by the low mobilities and longer dwell times near the interface.[105] In addition, Arkhipov et al. took into account a barrier lowering due to energetic disorder.[106]
Both modifications describe charge injection into organic semiconductors more realistically and have been confirmed by Monte Carlo simulations.[107, 108] However, these models have been developed for the limit of high injection barriers ($\Phi_B > 0.3$ eV) and might not be a priori applicable to high efficiency solar cells, where low barriers and efficient injection are promoted.
On the other hand, even in the regime of low injection barriers, electrode and semiconductor are in thermodynamic equlibrium and the amount of thermally injected charge carriers at the contact can be described by the convolution of the Fermi-Dirac distribution with the distribution of states in the semiconductor $g(E)$ [109]:

$$n = \int_{-\infty}^{\infty} \frac{1}{1 + \exp[(E - E_F)/kT]} g(E) dE. \tag{2.26}$$

Since in the case of vanishing barriers the charge carrier density at the contact is very high (in the order of the underlying DOS $\approx 10^{26} - 10^{27}$ m^{-3}) a space charge region forms close to the contact. If this density is high enough, it will supply all carriers needed for establishing the steady state current. Then, and only then is the current through the device not injection limited anymore, but determined by the bulk properties.
In either case, in a first approximation the height of the injection barriers - and with that the amount of injected charge carriers - is related to the charge carrier density in the device at a certain applied voltage in the dark. The total amount of dark charge in the device as a function of bias can be estimated with transient extraction experiments as it will be shown in Section 4.3.1. However, the exact distribution of the injected carriers across the layer cannot be directly probed by experiments. Since the spatial distribution of carriers plays an important role for understanding dynamic processes such as recombination and extraction, the aid of numerical device simulations has to be consulted.

2.7 Numerical Simulations

In the course of this work two different types of numerical simulations have been used to support the experimental results and shall be briefly introduced in the following section. A steady state device simulation was used to understand the influence of different bias and illumination conditions on the charge carrier densities and distributions in the solar cells. This device simulation was also utilized to generate

whole $J-V$ curves with experimentally determined dynamic parameters as input parameters.
On the other hand, a transient drift diffusion simulation was applied to understand the physics of the TDCF transients and to compare simulated transients with an analytic solution. Furthermore, the transient simulation served as a fit routine for experimental TDCF transients to extract physical parameters as for example the charge carrier mobility.

2.7.1 Steady State Device Simulation

The code for the steady state device simulation has been kindly provided by Prof. Jan Anton Koster and has been described in detail in reference [110].
The device is described as an effective medium with the LUMO of the acceptor and the HOMO of the donor placed between two metal electrodes. The energy difference between the acceptor LUMO and donor HOMO is defined as the effective bandgap E_g. The model contains drift and diffusion of charge carriers and the effect of space charge on the electric field in the device.
Non-geminate recombination is implemented as a bimolecular process. A Braun-Onsager mechanism to describe free carrier generation and geminate recombination can be optionally applied. As default, carrier generation is assumed to be homogeneous across the active layer, however user-defined generation profiles may be applied.
The basic equations to be solved are the Poisson equation:

$$\frac{\partial^2}{\partial x^2}\psi(x) = \frac{q}{\varepsilon\varepsilon_0}[n(x) - p(x)], \tag{2.27}$$

relating the electrostatic potential $\psi(x)$ to the electron and hole densities $n(x)$ and $p(x)$, respectively, and the current continuity equations:

$$\frac{\partial}{\partial x}J_{n(p)}(x) = (-)qU(x), \tag{2.28}$$

where $J_{n(p)}(x)$ is the electron (hole) current density and $U(x)$ is the net generation rate, i.e. the difference between generation and recombination of free charge carriers. Only one spatial dimension is considered.
The scheme used to solve these equations follows the work by Gummel [111] and is sketched in Figure 2.9. Here, first a guess is made for the potential and the carrier densities from which a correction $\delta\psi$ is calculated from the Poisson equation. The new potential is then used to update the carrier densities with the continuity equations. The process is repeated until convergence is reached.
For boundary conditions the carrier densities are specified for $x = 0$ and $x = L$, where x is the position in the device and L is the layer thickness. The contacts are assumed to be in thermodynamic equilibrium and Boltzmann statistics are used to determine the carrier densities at the first grid point of the device. For the top contact they are

$$n(0) = N_c \exp(-\frac{\Phi_{Be}}{kT}) \quad \& \quad p(0) = N_c \exp(-\frac{E_g - \Phi_{Be}}{kT}) \tag{2.29}$$

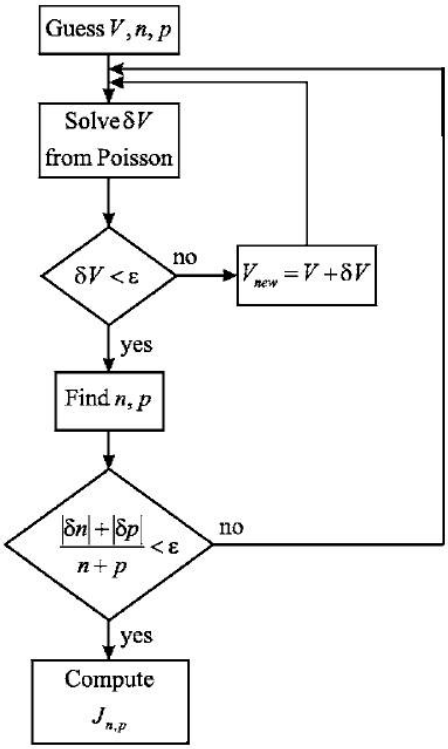

Figure 2.9: Flow diagram of the simulation program. The Gummel iteration is used to solve the basic equations as described in the text and in reference [110]. Figure taken from reference [110].

and for the bottom contact they are

$$p(L) = N_c \exp(-\frac{\Phi_{Bh}}{kT}) \quad \& \quad n(L) = N_c \exp(-\frac{E_g - \Phi_{Bh}}{kT}), \tag{2.30}$$

where N_c is the effective density of states of both the conduction and the valence band. Since the exact values of the effective densities of states of valence and conduction band are not known, one value for both bands is used.[110] Φ_{Be} and Φ_{Bh} are the injection barriers for electrons and holes, respectively, defined as the difference of the respective band edge and the electrode Fermi level. To be precise, for vanishingly small injection barriers the Fermi-Dirac statistics should be used, see Equation (2.26) in the previous section. However, the maximum factor by which the carrier density is overestimated when using the Boltzmann approximation is 1.44 (for $\Phi_B \equiv 0$). For injection barriers above 0.1 eV the error drops below 1%.

2.7.2 Transient Drift Diffusion Simulation

The transient drift diffusion simulation was developed by Dr. Sebastian Bange during his PhD at Potsdam University and is in detail described in his PhD Thesis.[112] Similar to the steady state simulation the device is described as an effective medium

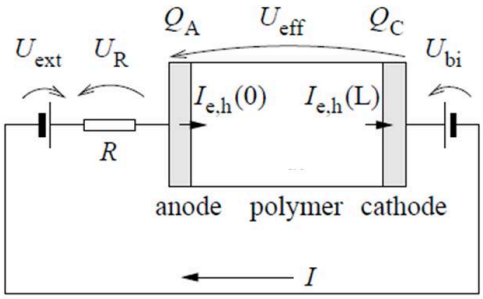

Figure 2.10: The model for the external electrical circuit used in the numerical transient simulations by S. Bange. The external resistance R determines the current I that charges the anode and cathode electrodes. More details in reference [112]. Figure taken from reference [112].

between two conducting electrodes. The basic equations to be solved are again the Poisson equation (2.27) and the continuity equation for the charge carrier densities $n_{e,h}$, however in this model all parameters depend explicitly on time:

$$\frac{\partial}{\partial t} n_{e,h}(x,t) = \pm \frac{1}{e} \frac{\partial}{\partial x} j_{e,h}(x,t) - \frac{e}{\varepsilon \varepsilon_0} (\mu_e(x,t) + \mu_h(x,t)) n_e(x,t) n_h(x,t), \qquad (2.31)$$

where the current densities $j_{e,h}(x,t)$ include the contributions of drift and diffusion of the charge carriers. Recombination of charge carriers is treated in terms of the Langevin meachanism and the field dependence of the mobilities is assumed to follow a Poole-Frenkel type behaviour. The boundary conditions for the current densities at the contacts $x = 0$ and $x = d$, are treated with the injection model by Scott and Malliaras (see Section 2.6). Here, disorder and space charge effects at the interface are neglected and an effective resulting interface current is calculated.
In the model of the external circuit, the total resistance is given by the resistance of the active layer and the (ohmic) series resistance R, which mainly includes the ITO traces of the sample and the input resistance of the oscilloscope. According to Figure 2.10 the potential drop at the resistor R:

$$U_R = U_{ext} - U_{bi} - U_{eff}, \qquad (2.32)$$

is calculated from the external applied voltage U_{ext}, the built-in potential U_{bi} due to the work function difference of the electrodes and from the effective potential in the active layer due to the internal field distribution:

$$U_{eff} = \int_0^d E(x,t) dx. \qquad (2.33)$$

The electrical current flowing in the external circuit, charging and discharging the electrodes, is then calculated by $I = U_R/R$ and the temporal evolution of the current is implemented as follows:
At a time $t = 0$ a certain charge carrier distribution $n_{e,h}(x,t)$ is inserted into the

device, which then evolves with time due to drift, diffusion and bimolecular recombination. According to the Poisson equation the carrier distribution determines the internal electric field distribution $E(x,t)$ and with that also determines the local mobilities in the layer. Using Equation 2.33 the potential drop across the active layer is calculated, which sets U_R and the current $I = U_R/R$.
After a timestep δt the charge carriers are redistributed according to drift, diffusion and recombination. The altered carrier distribution $n_{\mathrm{e,h}}(x,t)$ implies a change in $E(x,t)$ and U_{eff}. If U_{ext} is constant, Equation 2.32 requires that U_R changes, accompanied with a change of the output current I. For details of the numerical methods and algorithms see ref. [112].
In the course of this work, a number of refinements to the code described in [112] have been done in collaboration with Steffen Seckler, to adjust the simulation to the special requirements of this work. For example, the injection of charge carriers can now alternatively be allowed in terms of a thermodynamic equilibrium, i.e. with Boltzmann statistics, or can be completely forbidden. Such blocking contacts are usually required for the analytic description of transient experiments. In addition, to probe the influence of selective contacts on the recombination dynamics, the charge carriers can either be allowed to diffuse out of the device at both contacts or only at the specified contact.
Since the Langevin recombination mechanism seems not to be applicable in most investigated organic solar cells, a general bimolecular recombination mechanism with rate constant k_{BR} was implemented instead. For the verification of the iterative analysis scheme of the recombination dynamics in the presence of dark charge (Section 4.3.1), also the optional generation of a background carrier density in dynamic equlibrium was implemented.
Furthermore, the original program only allowed the insertion of charge carriers, i.e. to simulate photogenerated charge carriers after a laser pulse, at t=0 and with a homogeneous or exponential carrier profile. We extended the insertion of photoinduced charge carriers at any time delay and with arbitrary density profile. The delayed carrier insertion is important for the simulation of TDCF transients at different pre-bias conditions. On the other hand, the arbitrary carrier profile can be used to simulate extraction currents after steady state illumination, as for example in a BACE experiment (see Chapter 5), using the simulated carrier profiles from the steady state simulation.
Last but not least, in some TDCF experiments a very fast decay of the photocurrent at very short times has been observed. To account for this fast initial decay, a time dependent mobility was introduced with an either eponential or linear dependence on time. This feature allows better fit results in some cases.

2.8 Materials

Here a short introduction to the blend systems studied in this work, P3HT:PCBM and PTB7:PCBM, will be given with the most important properties and features. The detailed sample preparation and device structures can be found in the appendix A.2. The chemical structures of the components are shown in Figure 2.11.

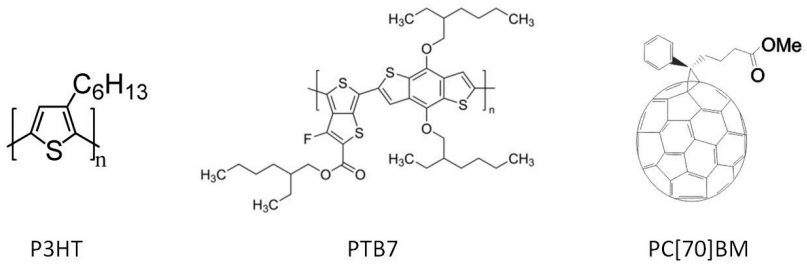

Figure 2.11: Chemical structures of the donor polymers P3HT (poly(3-hexylthiophene)) and PTB7 (thieno[3,4-*b*]thiophene-*alt*-benzodithiophene) and the acceptor molecule PC[70]BM ([6,6]-phenyl C_{71} butyric acid methyl ester).

2.8.1 P3HT:PCBM

Bulk heterojunction (BHJ) solar cells comprising P3HT and PCBM are among the most studied organic photovoltaic devices to date. Most of the success of this material combination can be attributed to the strong tendency of regioregular P3HT to self-organize into a microcrystalline structure leading to a high hole mobility.[113, 114] However, the presence of PCBM seems to disrupt the crystallization of P3HT [115] and the initial morphology of as prepared chloroform (CF)

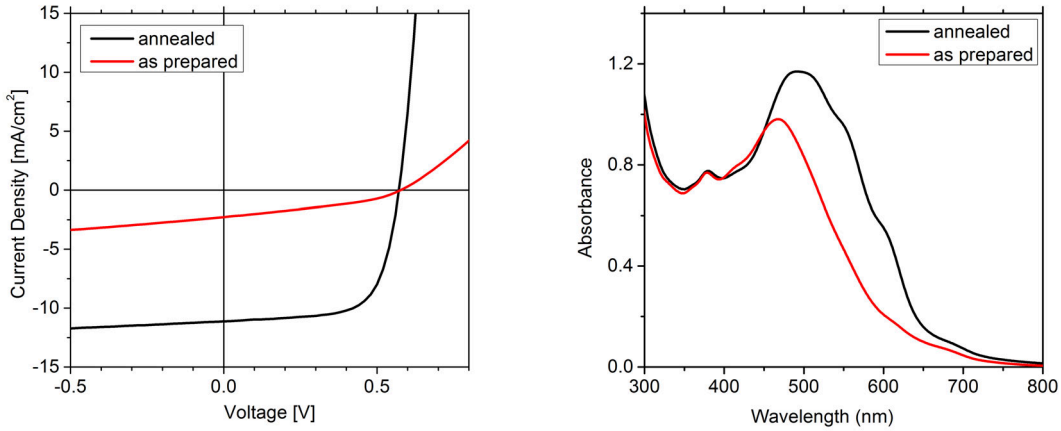

Figure 2.12: Left: $J-V$ characteristics for P3HT:PCBM blends cast from CF under AM1.5G illumination. The FF are 67.8% for the thermally annealed (at 140°C for 10 min) and 35.2% for the as prepared device. Right: Absorbtion spectra of as prepared and annealed 200 nm blends on glass.

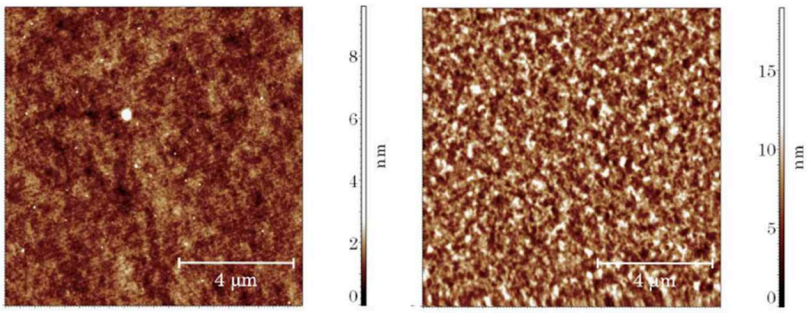

Figure 2.13: AFM images of as prepared (left) and thermally annealed at 140°C for 10 min (right) P3HT:PCBM films cast from CF. Images taken from [118].

cast 1:1 blends shows a very low total film crystallinity [116–118] and a very fine intermixing of donor and acceptor domains. This results in a rather poor solar cell performance with a PCE of 0.5% (Figure 2.12 left).
It has been shown that thermal annealing leads to a coarsening of the domain structure (Figure 2.13) with an increase in size and order of the crystalline P3HT domains, accompanied by aggregation of PCBM molecules.[114, 116–119] The improved crystallinity of annealed blends becomes visible in the absorption spectra (Figure 2.12 right) and the resulting morphology comprises an interpenetrating network of rather pure nanometer-sized crystalline domains. This leads to an overall efficiency improvement by almost one order of magnitude with a PCE of 4.1%.

2.8.2 PTB7:PCBM

Among the novel high efficiency donor polymers with purposefully engineered energy levels, PTB7 stands out with the highest certified PCE for single junction OSC to date in a 1:1.5 blend with PCBM.[30, 31] PTB7 consists of alternating ester substituted thieno[3,4-*b*]thiophene and benzodithiophene units.[120] This concept of donor-acceptor copolymers with alternating electron-rich and electron-deficient repeat units significantly reduces the bandgap compared to homopolymers.[121] In the case of PTB7 an electrochemical bandgap of 1.84 eV was measured [120], which results in an optimized match of the absorption spectrum to the solar spectrum and to a concomitant larger photon harvesting, compared to P3HT with an electrochemical bandgap of 2.28 eV.[122] In addition, the introduction of an electron-withdrawing fluorine atom in the polymer backbone decreases both HOMO and LUMO. In sum these effects lead to an increased V_{OC} and J_{SC} in the blend with PCBM and to an overall higher performance (Figure 2.14), compared to P3HT.
It has been shown, that the device properties of PTB7:PCBM blends cast from chlorobenzene (CB) largely depend on the processing conditions. In particular, the addition of 1,8-diiodooctane (DIO) significantly increases the FF and J_{SC}, which was mainly attributed to an optimized phase-separated morphology.[120] A study by Collins et al. reported large agglomerated fullerene domains of the order of 100-200 nm in the layers prepared without DIO, embedded in a polymer-rich matrix.[123]

In blends processed with DIO the domain size was found in the order of 30 nm (Figure 2.15, left). In addition a more recent study by Hedley et al. [124] showed that the large fullerene domains in the devices without DIO consist of smaller very pure PCBM spheres with diameters of 20-60 nm (Figure 2.15, right). However, the complex morphological structure in these blends and the impact of DIO is yet not fully understood and is still subject to current research studies.

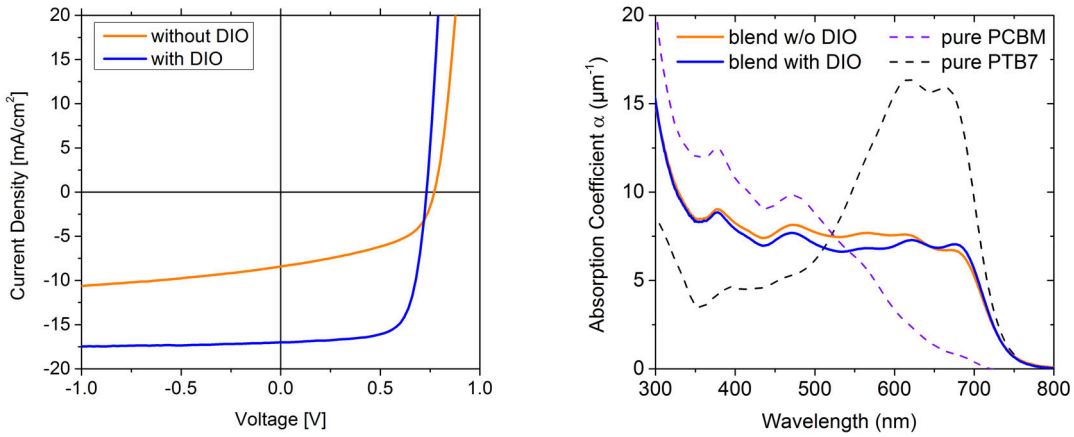

Figure 2.14: Left: $J-V$ characteristics for PTB7:PCBM blends under AM1.5G illumination. The FF and PCE are 71.5% and 9.1% with DIO and 49.7% and 3.3% w/o DIO, respectively. Right: Absorbtion spectra of blends with and without DIO and pure PCBM and PTB7 layers.

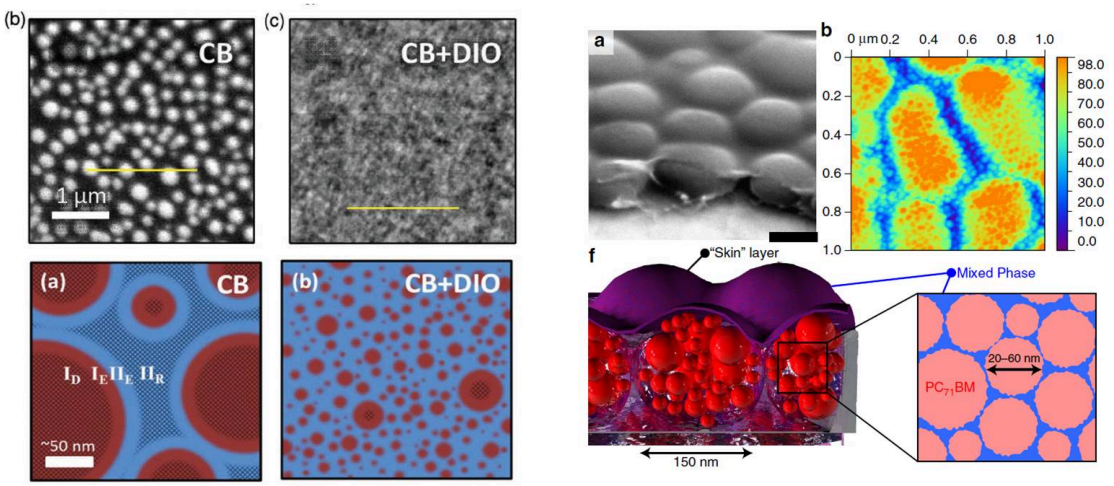

Figure 2.15: Left: Film composition maps (upper panel) measured with resonant microscopy from [123]. Light regions indicate PCBM-rich domains and dark regions are PTB7-rich domains. The lower panel shows the structural model (brown are pure PCBM agglomerates and blue is the mixed PTB7-rich matrix phase). Right: SEM (a), AFM (b) in combination with time-resolved photoluminescence studies by Hedley et al. [124] reveal that the large fullerene-rich domains in blends w/o DIO are comprised of smaller pure PCBM spheres (f).

3 Time Delayed Collection Field - Theoretical Description and Analysis

3.1 Introduction

One of the central issues in the description of the current-voltage ($J-V$) characteristics of organic solar cells is the origin of the field-dependent photocurrent. Commonly, a field-dependent photocurrent has been attributed to a field-dependent charge generation process.[23, 25] As was discussed in the previous chapter, there is strong evidence that charge generation proceeds via the split-up of thermalized CT states. If these states are strongly Coulomb bound, i.e. there is a large energetic barrier between the CT state and the charge separated state, an additional electric field is necessary to generate free charge carriers (compare Section 2.3). Consequently, at low external fields most CT states might recombine geminately back to the ground state and are lost to the photocurrent. In this case the photogenerated current is expected to depend on the applied electric field.
Alternatively, Shuttle et al. showed that the $J-V$ characteristics of annealed P3HT:PCBM can be entirely explained by the competition between nongeminate recombination and extraction, without the need of a field-dependent generation.[17] In practice it is nontrivial to decide whether the field dependence of the photocurrent is due to geminate or non-geminate recombination losses. Since the origin of these losses is important for a complete understanding and target-oriented improvement of organic solar cells, the field dependence of the photocurrent is a central topic of this thesis.
A critical point at the beginning of this work was the lack of available experimental techniques to directly measure the effect of the electric field on free charge carrier generation. Information on the kinetics of CT formation, dissociation and recombination had been mainly gained from time resolved transient absorption spectroscopy (TAS). While most of these measurements were taken in the absence of an electric field [21, 22, 125], more recently TAS studies on working devices with applied biases have been published.[19, 20] A general problem in TAS measurements is the simultaneous presence of different neutral and charged excitations, which often complicates the unequivocal distinction of bound charges in CT states and free, extractable polarons. More importantly, the change in absorbance due to excitons or polarons is rather small. Therefore, to obtain suitable signal-to-noise-ratios, high fluences are required, usually in a regime where nonlinear effects begin to dominate the processes.
An elegant way to directly measure photogenerated charges and the influence of an electric field on the charge generation process is the *Time Delayed Collection Field* (TDCF) method which was advanced and refined in the course of this work. TDCF is analogous to a pump-probe experiment, however, using optical excitation and an electrical probe. Figure 3.1 shows the schematic timeline of the TDCF experiment. The sample is illuminated by a short laser pulse while being kept at a constant prebias voltage V_{pre}. After the delay time t_{d}, a rectangular pulse with voltage V_{coll}

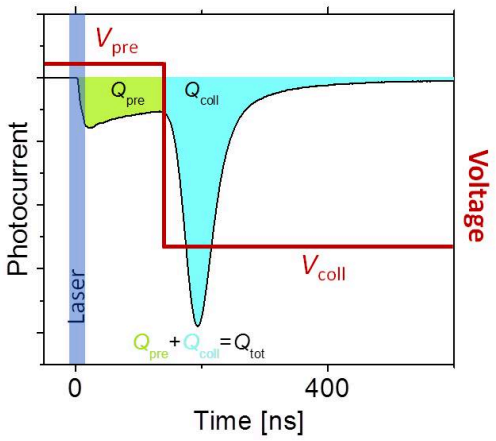

Figure 3.1: Schematic timeline of the TDCF experiment. At t=0 the sample is illuminated by a short laser pulse, while being kept at a constant pre-bias voltage V_{pre}. At t=t_d a rectangular voltage pulse (red line) of V_{coll} is applied to collect the photogenerated charge carriers from the layer. The black line indicates the corresponding photocurrent transient.

is applied to extract all remaining free charge carriers. The motion of the photogenerated charge carriers causes a photocurrent as indicated by the black line in Figure 3.1. In contrast to steady state current-voltage measurements, classical time-of-flight experiments or the photo-CELIV (charge extraction by linearly increasing voltage) technique, TDCF allows to apply different biases during generation and collection of the charge carriers. This enables a direct study of the field-dependence of charge carrier generation and extraction.

Before the beginning of this work, TDCF measurements on organic materials had been scarcly reported. Experiments on single-component organic layers were for the first time performed in the 1980's and revealed a pronounced dependence of the relative photoresponse of the sample on the prebias during illumination.[126, 127] In this set-up a minimum delay time of 100 ns could be realized due to rise time limitations of the collection voltage pulse. In 1996 and 2002 the same set-up was used to study the field-dependent generation in single polymer layers of poly(*p*-phenylene vinylene) (PPV) and poly(para-phenylene) (MeLPPP), respectively. In both cases a strong field-dependence of the relative photoresponse was found.[128, 129]

In 2006, TDCF was used to study the recombination of photogenerated charges in a blend of PCBM with a soluble PPV-derivative.[130] These experiments suggested that the photogenerated electrons and holes escaped the mutual Coulomb potential within the time resolution of the set-up, which was 3 μs. Here, for the first time the integral of the photocurrent was evaluated to gain the amount of photogenerated charge.

We took up and refined this approach in 2011 to study the field dependence of charge carrier generation and recombination in the benchmark system P3HT:PCBM with an improved and exceptional short pulse rise time of 20 ns and a delay time of

100 ns.[131] During the time of this thesis, pulse rise time and time delay have been further improved both to 10 ns.[1] As a legacy of this work, TDCF is now a well established method to characterize the charge generation process in organic BHJ solar cells, proven by the number of publications in the past three years.[18, 26, 70, 71, 132–144] Before the beginning of this work, publications were few and a detailed analysis of the photocurrent transients was missing. Importantly, this technique is entirely based on the determination of charge carrier densities at different applied fields, illumination intensities and time delays by evaluating photocurrent transients. Therefore, a detailed understanding of the origin, shape and dependence on experimental parameters of a transient is essential for the correct interpretation of the experimental results. This will be the focus of this chapter.

3.2 Understanding TDCF Transients

3.2.1 In the dark

In this section the current in the device and in the external circuit, that is induced by the application of an external voltage, will be analyzed. Before providing a description of the photocurrent transients after the laser pulse, the processes in the dark will be investigated. These are of great importance since the dark measurements always serve as a reference to the light measurements to negate capacitance effects. Even more importantly, the analysis of the dark current transients yields important information about the actual time resolution of the experimental set-up.

In the specific device structure of organic BHJ solar cells, an effective medium composed of an intermixed blend of the donor and acceptor material, is placed between two conducting electrodes (see appendix A.2 for details). In this structure the sample can be approximately described as a parallel plate capacitor of capacitance $C = \varepsilon\varepsilon_0 A/d$, with layer thickness d and electrode area A, filled with a dielectric with relative permittivity ε. Therefore, in an electric circuit (see inset of Figure 3.2) with an external voltage source the familiar equations for capacitor charging and discharging can be used.
If a constant external DC voltage U_0 is applied and the capacitor is initially uncharged, the electrodes will be charged and a charging current I is flowing in the external circuit following the differential equation:

$$R\frac{dI}{dt} + \frac{I}{C} = 0, \tag{3.1}$$

which has the solution:

$$I(t) = I_0 \exp(-t/RC), \tag{3.2}$$

with $I_0 = U_0/R$. The voltage trace of an ideal rectangular voltage pulse, and the charging current according to Equation (3.2) are depicted in Figure 3.2 left. Because of the series resistance R, the charging process takes a finite time. This is

[1] mainly by the work of Jona Kurpiers

characterized by the RC time constant, the time at which the current drop reaches $1/e$ of its maximum. Thus, the RC time represents a lower limit for the temporal resolution of the set-up.
Typical values for the sample capacitance of devices used in this work are in the order of 350 pF, assuming $\varepsilon = 4$, $A = 1$ mm^2 and $d = 100$ nm. The series resistance in the circuit is mainly determined by the input resistance of the oscilloscope (50Ω), the resistance of the operational amplifier (10Ω) and the ITO traces on the substrate. Assuming $R = 60\Omega$ leads to an RC time constant of only 21 ns. Such low RC time constants (compared to earlier studies) are mainly attributed to the very small electrode areas and short ITO traces to the active area used in this set-up.
A further limitation of the experimental time resolution is given by the actual shape of the voltage pulse. In reality, the voltage pulse must be described by a ramp with a finite rising time (Figure 3.2 middle). The function generator used in these TDCF experiments (Agilent 81150A) has a specified rise time of only 2.5 ns. However, the voltage signal at the sample is determined by the operational amplifier enhancing the output signal of the function generator. This amplifier has a specified rise time in the order of 20 ns. This is still far below typical rise times reported in earlier studies [128–130], however, it already has a significant influence on the shape

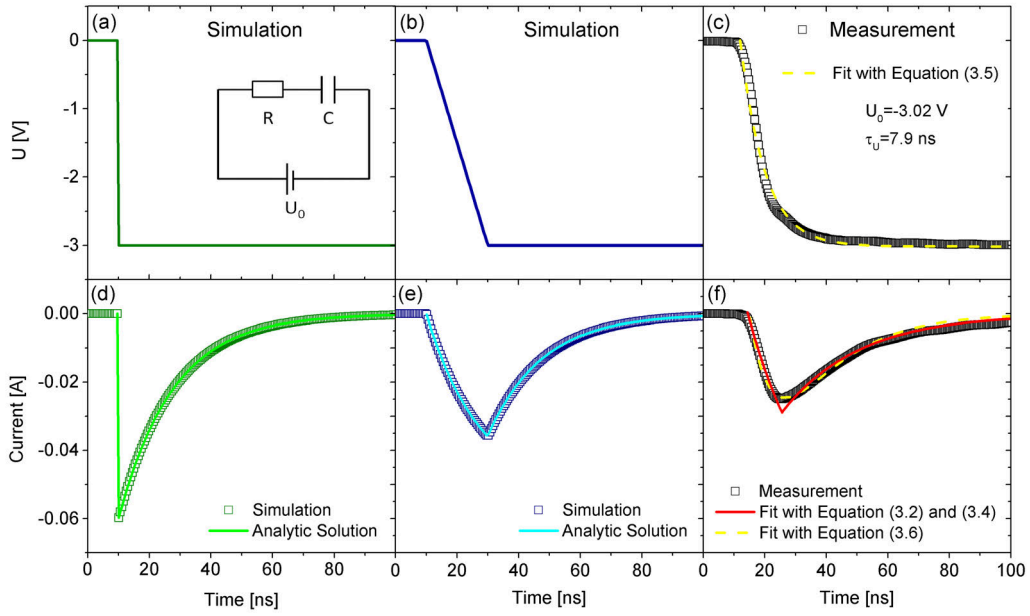

Figure 3.2: (a)-(c) show time traces of an ideal rectangular voltage pulse (green), a voltage pulse with a linear ramp of 20 ns (blue) and a measured voltage pulse (black symbols). The corresponding simulated (green and blue symbols) and measured (black symbols) dark current transients are shown in (d)-(f). The best fit to the measured curve with Eqs. (3.2) and (3.4) (red line) yields $R = 71\Omega$ and $C = 280pF$ and with Eq. (3.6) (dashed yellow line) $R = 64\Omega$ and $C = 280pF$ for this particular sample. The inset shows the RC-circuit that serves as the basis for the analytic calculations.

of the current signal (Figure 3.2 (e)), which is visible mainly as a total delay of the current maximum and a finite current increase before the subsequent decay. The current increase stems from the time dependent voltage signal and can be analytically described using Equations (3.3) and (3.4) and the boundary condition $I(t = 0) = 0$.

$$\frac{dI}{dt} + \frac{I}{RC} = \frac{\dot{U}}{R} \tag{3.3}$$

$$I(t) = C\dot{U}(1 - \exp(-t/RC)). \tag{3.4}$$

Note, that in Equation (3.4) the time dependent voltage signal was approximated by a linear ramp $U(t) = \dot{U}t$. The solution is displayed in Figure 3.2 (e). For comparison Figure 3.2 also displays the numerically simulated dark current transients (green and blue symbols), using the transient simulation program described in Section 2.7.2. There is perfect agreement between the simulation and the analytic solution. Therefore, either the numeric or the analytic description can be used to determine the RC time constant of the set-up from the measured dark current transients.
An example for an experimental voltage trace and the corresponding dark current transient for a typical solar cell used in this work is shown in Figure 3.2 (c),(f). It is obvious, that the real voltage pulse does not show a linear ramp, but follows a more complicated function leading to a rounded edge in the vicinity of the maximum voltage.
A good fit (red line) with Equations (3.4) and (3.2) can still be achieved using $R = 71\Omega$, $C = 280$ pF ($RC = 20$ ns) and an approximated linear voltage ramp with a rise time of 12 ns. These values are very close to the theoretically expected ones. It indicates that the additional resistance due to ITO traces is in the order of 10 Ω. Furthermore, from the measured capacitance $C = 280$ pF and the layer thickness $d = 126$ nm and electrode area $A = 1$ mm^2 of this particular sample the relative permittivity of the donor-acceptor blend can be calculated. The value for this blend (PTB7:PCBM with DIO) is exactly 4 and will be used in the numerical simulations throughout this thesis.
Alternatively, the measured voltage signal can be approximated by Equation (3.5)

$$U(t) = U_0(1 - \exp(-t/\tau_U)), \tag{3.5}$$

with τ_U being the characteristic rise time. Figure 3.2 (c) shows that Equation (3.5) is a good approximation with τ_U=7.9 ns. Solving the differential equation arising from (3.3) and (3.5) leads to a description of the entire current transient with a single equation:

$$I(t) = \frac{U_0 C}{\tau_U - RC}(\exp(-\frac{t}{\tau_U}) - \exp(-\frac{t}{RC})). \tag{3.6}$$

The best fit of the measured current transient in Figure 3.2 (f) (yellow dashed lines) with Equation (3.6) yields the parameters $R = 64\Omega$ and $C = 280$ pF, implying an RC time of 18 ns. The similarity of both parameter sets indicates that both approaches yield an equivalent good description of the physical processes.
In conclusion, this section shows that the current flow through an organic solar cell

device in the dark in response to the application of a time dependent reverse voltage pulse can be described as an electrode charging of a capacitor with capacitance C in series with resistance R. The analysis of the dark transient reveals information about the RC time constant of the circuit, which is important for the time resolution of the set-up. Furthermore, the numerical simulation described in Section 2.7.2 perfectly reproduces the physical processes in the dark and is, therefore, also a trustworthy basis for the analysis of the processes under illumination which will be discussed in the next section.

3.2.2 Under Illumination

If photogenerated charge carriers are introduced in the organic layer, an additional current flow is measured upon the application of a voltage pulse due to the motion of the charges. By subtracting the pure capacitive response of the specific sample in the dark ('Dark Transient') from the transient under illumination, the contribution of the free charge carriers moving across the device can be separated. This contribution will in the following be called 'Photocurrent Transient' and shall now be described analytically.
It is assumed that at $t = 0$ the density of holes and electrons is equal ($n_e = n_h = n$) and independent of the position within the layer. These assumptions are reasonable, if the charge carriers are generated by a short laser pulse. Furthermore it is initially assumed that only one charge carrier type is mobile (here, the electron mobility is much larger than the hole mobility, $\mu = \mu_e \gg \mu_h$) and that bimolecular recombination and diffusion of charge carriers during extraction can be neglected. This is true for low carrier densities and gradients as will be shown later. Upon the application of an external voltage U_0, the electrons start moving across the layer with velocity v:

$$v = \frac{dl}{dt} = E(l)\mu, \tag{3.7}$$

leaving behind a charged layer of holes up to the time dependent extraction depth $l(t)$, see Figure 3.3. This charged layer induces an electric field which is time depen-

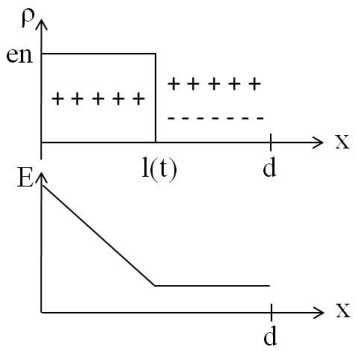

Figure 3.3: Schematic charge distribution and resulting electric field in the device for the case of mobile electrons and immobile holes.

dent. The time dependent field across the layer can be calculated from the Poisson equation $dE/dx = en/\varepsilon\varepsilon_0$ to:

$$E(x,t) = \begin{cases} E(0,t) - \frac{enx}{\varepsilon\varepsilon_0} & 0 < x < l(t) \\ E(d,t) & l(t) < x < d. \end{cases} \tag{3.8}$$

The potential drop across the sample is then:

$$U_0 = \int_0^d E(x)dx \tag{3.9}$$

By combination of Equations (3.7), (3.8) and (3.9) a differential equation is obtained for the extraction depth $l(t)$ in the form:

$$\frac{dl(t)}{dt} = U_0\frac{\mu}{d} - \frac{en\mu}{2\varepsilon\varepsilon_0 d}l^2(t). \tag{3.10}$$

This equation has been derived earlier in reference [145] for the general case of a time dependent voltage $U(t)$. In this general case the differential equation cannot be solved analytically. However, here, in the case of a time independent voltage signal an analytic solution can be obtained, which is:

$$l(t) = a\tanh(bt), \tag{3.11}$$

with $a = \sqrt{\frac{2\varepsilon\varepsilon_0 U_0}{ne}}$ and $b = \sqrt{\frac{e\mu^2 nU_0}{2d^2\varepsilon\varepsilon_0}}$ and the boundary condition $l(0) = 0$. The current density due to the moving charges can then be calculated by averaging Ohm's law:

$$j(t) = \frac{1}{d}\int_0^d \sigma(x,t)E(x,t)dx = \frac{ne\mu}{d^2}(d - l(t))(U_0 - \frac{en}{2\varepsilon\varepsilon_0}l^2(t)). \tag{3.12}$$

The solutions for $l(t)$ and $I(t) = Aj(t)$ for typical experimental parameters are depicted in Figure 3.4. It is obvious, that at high charge carrier densities and low voltages, when the internal electric field due to the remaining holes is larger than the external field due to the applied voltage, $l(t)$ never reaches the value of the layer thickness d. In this case, which can be approximated by the relation $U_0 < \frac{ned^2}{\varepsilon\varepsilon_0}$, a part of the photogenerated charge carriers is left in the device and is not accounted for in the photocurrent. Therefore the integral of the photocurrent transient will be lower than the true amount of photogenerated charge. This effect is demonstrated in the inset of Figure 3.4. The integrated photocurrent (for constant n) increases as a function of applied voltage U_0. It saturates if U_0 is large enough to extract all charge carriers.
Note, that the current density according to Equation (3.12) is solely the contribution of the moving charge carriers and *not* the current measured in the external circuit through the resistance R. Therefore, the maximum current is flowing at $t = 0$ (Figure 3.4).

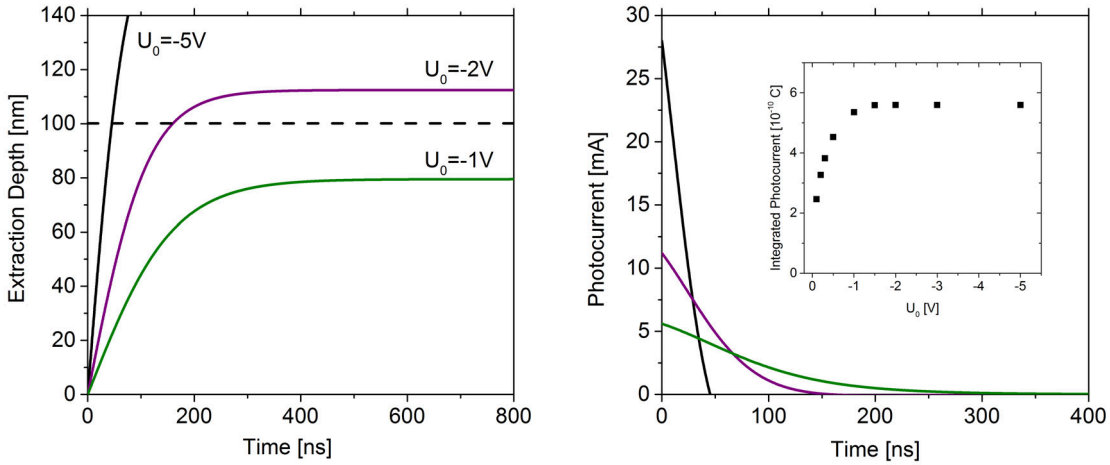

Figure 3.4: Left: Extraction depth $l(t)$ according to Equation (3.11) for the parameters $n = 7{\times}10^{22}$ m^{-3}, $\mu = 5{\times}10^{-4}$ cm^2/Vs, $d = 100$ nm and extraction voltage U_0 as indicated in the graph. The dashed line indicates the layer thickness d. Right: Corresponding photocurrent for the same parameters. Inset: Integrated photocurrent for different extraction voltages. For low voltages the integral is lower than the photogenerated charge.

From Figure 3.4 it is obvious that low carrier densities or high extraction voltages are required to obtain reasonable results. Remarkably, in the limit of $n \ll \frac{U_0 \varepsilon \varepsilon_0}{ed^2}$, the electric field contribution of the space charge can be neglected and the solution of the photocurrent simplified. The current due to the drift of charge carriers in the constant external field is then calculated as:

$$I(t) = \frac{A}{d} \int_0^d en(x,t)\mu \frac{U_0}{d} dx, \tag{3.13}$$

with

$$n(x,t) = \begin{cases} 0 & 0 < x < l(t) \\ n & l(t) < x < d. \end{cases} \tag{3.14}$$

and

$$l(t) = \frac{\mu U_0}{d} t. \tag{3.15}$$

For sake of simplicity here only the current due to motion of the electrons is considered. However, in the approximation of low carrier densities and negligible internal field, the total photocurrent is the sum of the electron and hole photocurrent transients $I(t) = I_e(t) + I_h(t)$. The solution to Equations (3.13) - (3.15) is given by

$$I_e(t) = \frac{Q_0}{t_{tr}} (1 - \frac{t}{t_{tr}}), \tag{3.16}$$

where $Q_0 = Aend$ is the initial photogenerated charge and $t_{tr} = d^2/\mu U_0$ is the transit time, defined as the time needed for one charge carrier to travel through the whole layer in the influence of the uniform external field U_0/d. Figure 3.5 shows,

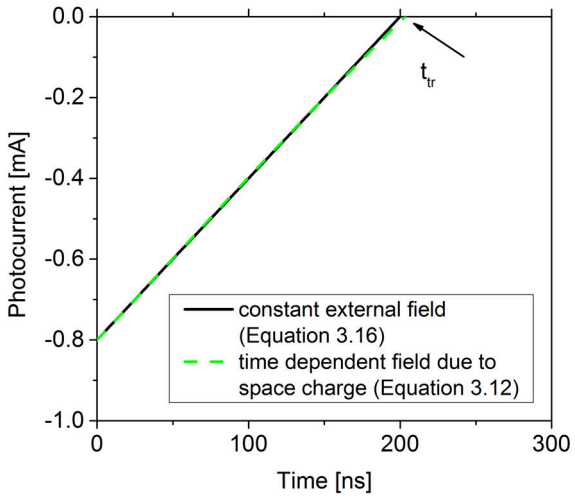

Figure 3.5: Photocurrent due to drift in a constant external field according to Equation (3.16), compared to the solution for a time dependent field due to build-up of space charge (Equation (3.12)). For typical experimental parameters ($n = 1 \times 10^{22}$ m^{-3}, $U_0 = -5$ V, $\mu = 1 \times 10^{-4}$ cm/Vs, $d = 100$ nm) the two solutions coincide.

that the two solutions, considering a constant field (Equation (3.16)) and a time dependent field due to the build up of space charge (Equation (3.12)) are almost identical for typical experimental parameters, fulfilling the condition $n \ll \frac{U_0 \varepsilon \varepsilon_0}{ed^2}$. The intercept with the time axis corresponds to the transit time of the charge carriers t_{tr}.[2]

So far only the contribution of the moving charges across the layer was considered, which will in the following be denoted as I_{int}. Next, the current I_{ext}, which is measured in the external circuit with a series resistance R shall be calculated. It will be shown, that the maximum of the photocurrent will be delayed due to the delayed recharging of the electrodes.
First, it is assumed that the external voltage U_0 has been applied a considerable time ($t \gg RC$) before the charge carriers are inserted, so that the sample electrodes are fully charged and no current is flowing. This is the case in the TDCF experiment, when the charge carriers are photogenerated under pre-bias conditions (compare Figure 3.1).
In an equivalent circuit diagram (see inset of Figure 3.6) the internal current I_{int} can be understood as an additional current source (e.g. a photodiode with $C = 0$) in parallel to the sample capacitance C. The total voltage in the circuit is in this case still given by:

$$U_0 = U_R + U_C = I_{ext}R + Q_C/C, \tag{3.17}$$

[2]Here and in the following the current transients are plotted on a negative current axis, for better comparison with measured transients. The polarity in our TDCF set-up is such that a reverse bias causes a negative current signal.

where Q_C is the charge on the sample electrodes. The current provided by the current source is first used to recharge the capacitor plates as a result of the moving internal charge. If the electrodes are charged the internal current contributes to the external current which can be measured across the resistor. In this model the external current is given by:

$$I_{ext} = I_{int} + \frac{dQ_C}{dt} \tag{3.18}$$

Using Equations (3.17) and (3.18) and the boundary condition $dU_0/dt = 0$ then leads to the following differential equation:

$$\dot{I}_{ext} + \frac{1}{RC} I_{ext} = \frac{1}{RC} I_{int}(t), \tag{3.19}$$

where $I_{int}(t)$ is the current due to the drift of the charges, given by Equation (3.16)[3]. Using the boundary condition $I(0) = 0$, the solution to Equation (3.19) is given by:

$$I_{ext}(t) = \frac{Q_0}{t_{tr}}(1 - \frac{t}{t_{tr}} - \exp(-\frac{t}{RC})) + \frac{Q_0}{t_{tr}^2} RC(1 - \exp(-\frac{t}{RC})). \tag{3.20}$$

A physically meaningful solution is obtained for $0 < t < t_{tr}$. In Figure 3.6 (left) the analytic solution of the photocurrent transient from Equation (3.20) is compared to

[3]Here it is implicitly assumed that I_{int} depends only on U_0 over the whole time period. In reality it will depend on $U_C = U_0 - U_R$ as soon as current flows in the external circuit. For simplicity it is assumed that $U_R \ll U_C$. For realistic parameters: $I \sim 1$ mA, $R = 50\Omega$, $U_R = 50$ mV.

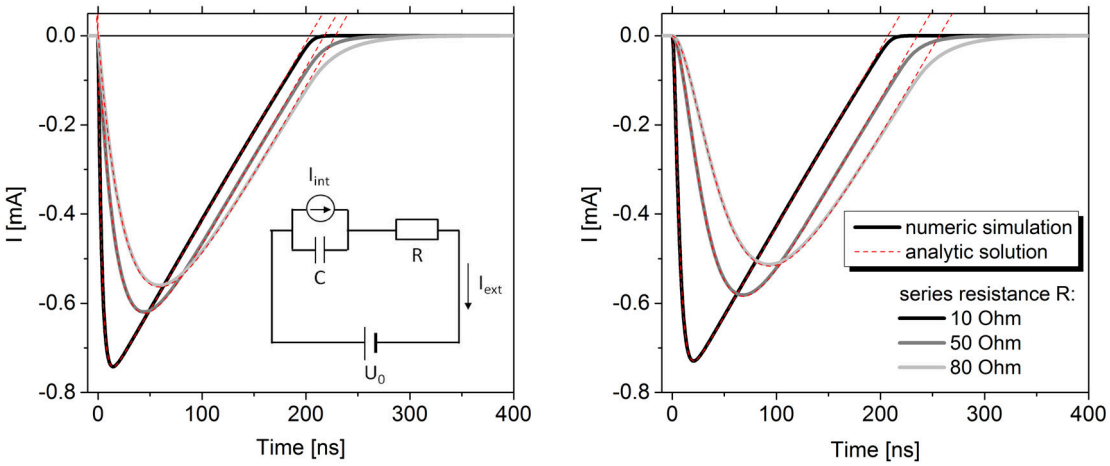

Figure 3.6: Analytic solution (red) and numerical simulation (black and grey) of photocurrent transients using the parameters: $\mu = 1 \times 10^{-4}$ cm/Vs, $n = 10^{22}$ m^{-3}, $U_0 = -5$ V, $C = 354$ pF and series resistance R as indicated in the graphs. Left: Constant voltage U_0 is applied before charge carriers are inserted at $t = 0$. Right: Charge carriers are inserted before the application of U_0 at $t = 0$ (with $U = 0$ for $t < 0$). The charging process of the sample electrodes slows down the motion of carriers at the beginning and further delays the extraction time. Inset: Equivalent circuit diagram for the derivation of the external photocurrent.

the numerical simulation, using the same input parameters for R, C, μ, n and U_0. The values for these parameters are given in the graph. For the chosen parameters, which are typically found in the experiments, the analytic solution perfectly matches the simulation. The analytic solution can now be used to study the influence of certain parameters, as for example the RC time, on the transient.
From Equation (3.20) it is obvious, that the photocurrent is a complex function of the series resistance, sample capacitance, mobility, charge carrier density and applied voltage. However, in the limit of $t \gg RC$, e.g. at long times or low RC time constants, Equation (3.20) simplifies to

$$I(t) = \frac{Q_0}{t_{tr}}(1 - \frac{t}{t_{tr}}) + \frac{Q_0}{t_{tr}^2}RC, \tag{3.21}$$

which is similar to Equation (3.16) except for the constant offset proportional to RC, which is caused by the retarded current flow through the resistor. The characteristic maximum occurs at

$$t_{\max} = RC\ln(\frac{t_{tr}}{RC} + 1) \tag{3.22}$$

and is determined by RC and t_{tr}. At times $t < t_{\max}$ the internal current I_{int} is needed to recharge the electrodes and only at times $t > t_{\max}$ the current leaves the device to the external circuit. The slope at short times and the height of the maximum are also determined by the initial charge carrier density n_0.

In the next step, the situation shall be investigated, where the external voltage U_0 is applied after the insertion of charge carriers (i.e. $U = 0$ for $t < 0$). In the TDCF experiment this describes the situation when the voltage is changed from pre-bias to collection bias after a certain time delay. In this case, the current rise will be delayed, since at short times ($t \ll RC$) the external electric field U_0/d is not completely available due to a finite charging time of the sample electrodes. Consequently, the time dependent voltage drop across the sample is approximately given by

$$U(t) = U_0(1 - \exp(-\frac{t}{RC})). \tag{3.23}$$

In this case Equation (3.16), which implies a constant drift velocity of the charge carriers, is not valid anymore. Rather the charge carriers move with a time dependent velocity given by the time dependent field:

$$v(t) = \frac{dl}{dt} = \mu E = \frac{\mu U(t)}{d} = \frac{\mu}{d}U_0(1 - \exp(-\frac{t}{RC})) \tag{3.24}$$

Integrating Equation (3.24) and using the boundary condition $l(0) = 0$ gives the solution for $l(t)$:

$$l(t) = \frac{\mu U_0}{d}(t + RC(\exp(-\frac{t}{RC}) - 1)). \tag{3.25}$$

Now, using Equations (3.13), (3.14) and (3.25) gives the internal current flow due to the drift of the charges in the time dependent external field:

$$I_{int}(t) = \frac{Q_0}{t_{tr}}(1 - e^{-\frac{t}{RC}}) + \frac{Q_0}{t_{tr}^2}(t - RC + 2RCe^{-\frac{t}{RC}} - te^{-\frac{t}{RC}} - RCe^{-\frac{t}{RC}}) \tag{3.26}$$

Putting this into Equation (3.19) and solving the resulting differential equation finally gives the measured photocurrent transient:

$$I_{ext}(t) = \frac{Q_0}{t_{tr}}(1 - e^{-\frac{t}{RC}}(\frac{t}{RC} + 1)) + \frac{Q_0}{t_{tr}^2}(-t + 2C - 2te^{-\frac{t}{RC}} + \frac{t^2}{2RC}e^{-\frac{t}{RC}} - RCe^{-\frac{2t}{RC}} - RCe^{-\frac{t}{RC}}) \tag{3.27}$$

The analytic and numerical solutions are displayed in Figure 3.6 (right). It is clearly visible that the charging process of the sample electrodes slows down the voltage increase across the active layer and with that the motion of the charges at short times ($t < RC$). In this time regime, the current is a quadratic function of time. The form of the transient at long times ($t \gg RC$) will be discussed in more detail in the following section and yields important information about the apparent transit time.

3.2.3 Extrapolation of the Photocurrent Decay

The current due to drift of charges in a constant electric field (Equation 3.16) follows a linear decay, intersecting the time axis at the transit time $t_{tr} = d^2/\mu U_0$. Motivated by this approach, commonly the extrapolation of the initial linear photocurrent decay (caused by the motion of the faster charge carrier type) to zero is used to determine the charge carrier mobility of the mobile charge carriers.[133, 135, 146, 147]
However, as has been shown in the previous section, in the case of a capacitive response across a resistor the motion of the charges is delayed with respect to the RC time constant of the circuit. In the limit of $t \gg RC$ Equation (3.27) simplifies to

$$I(t) = \frac{Q_0}{t_{tr}}(1 - \frac{t}{t_{tr}} + \frac{2RC}{t_{tr}}). \tag{3.28}$$

This expression becomes 0 at $t = t_{tr} + 2RC$. Hence, it follows that the time determined by extrapolating the initial photocurrent decay is larger than the true transit time by a constant offset of $2RC$ and the calculated mobility will be erroneous. In this approach, the true transit time should be greater than $40RC$ to keep the error of the mobility below 5%. This condition is not easy to meet in the field of thin film devices and increasing charge carrier mobilities.
Typical layer thicknesses for high efficiency organic solar cells are in the order of 100 nm [36, 148] and charge carrier mobilities are in the range of $10^{-4} \sim 10^{-3}$ cm^2/Vs [92]. For typical RC time constants of the set-up of $\sim$ 20 ns this requires extraction voltages as low as 0.123 V $\sim$ 1.25 V and consequently, to meet the condition of negligible internal field, charge carrier densities $n < 2.8 \times 10^{21}$ m^{-3}. The consequences, if these conditions are not clearly met, are shown in Figure 3.7. Here, the transit times were calculated according to $t_{tr}^{meas} = \frac{d^2}{\mu U_0} + 2RC$, using a constant input mobility of $\mu_{in} = 5 \times 10^{-4}$ cm^2/Vs, RC = 20 ns, d = 100 nm and different extraction voltages U_0. The plot shows the apparent mobilities extracted from t_{tr}^{meas}

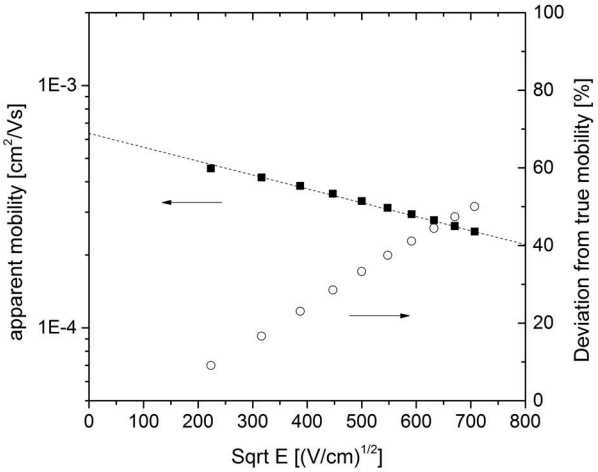

Figure 3.7: Apparent mobilities determined with $\mu = d^2/t_{tr}^{meas}U_0$ and $t_{tr}^{meas} = \frac{d^2}{\mu_{in}U_0} + 2RC$ for different collection voltages U_0. The constant input mobility was $\mu_{in} = 5 \times 10^{-4}$ cm^2/Vs. The apparent negative field dependence of the extrapolated mobility is due to the constant offset of $2RC$ in Equation (3.28). The deviation from the true mobility becomes large at high extraction fields.

as a function of $\sqrt{E}$. An apparent negative field dependence of the mobility appears, even though the input mobility was field independent and the true transit time was more than one order of magnitude higher than the RC time constant. The error of the measured mobility is up to 50% for high voltages and low transit times. From the plot in Figure 3.7 an apparent Poole-Frenkel factor of field dependent mobility of $\beta = -0.0013\sqrt{cm/V}$ (compare Section 2.5) can be calculated, which is purely due to the incorrect determination of t_{tr}. Indeed, Poole-Frenkel factors in this order have been reported [133, 135] and could be a consequence of a too small t_{tr}/RC ratio.
To determine the true carrier mobility it is necessary to determine the correct RC time constant of the set-up, e.g. from the dark transients as described in Section 3.2.1 and subtract $2RC$ from the extrapolated transit time.

3.2.4 The Photocurrent Integral

As discussed in the beginning of this chapter, TDCF has been primarily developed to measure charge carrier densities under different pre-bias and time delay conditions. In general the photocurrent is a displacement current caused by the motion of electrons and holes travelling in opposite directions towards the collecting electrodes. Since photogeneration creates electrons and holes in close vicinity to each other, this process does initially not alter the electric field or electric polarization inside the layer. As a result, the charge stored on the electrodes is unchanged. The motion of electrons and holes in opposite direction then causes a redistribution of the electrode charge, which is seen as an external displacement current. However, after all charge is extracted the active layer returns to its initial state and the electrode

charge is the same as before the extraction of the photogenerated charge. Conservation of charge then requires that the charge that has flown in the external circuit is the same as the photogenerated charge that has been extracted at the electrodes. Therefore, if no charge carriers are lost within the active layer, the integral of the photocurrent over a significantly long time interval is equal to the photogenerated charge:

$$Q_{photo} = \int_0^t I_{photo}(t)dt. \tag{3.29}$$

This is also true if electron-hole pairs were generated inhomogeneously across the layer, since in total each pair still travels the full distance d. In case that one charge carrier type is completely immobile, as was assumed in the transient analysis in Section 3.32, the mobile charge carriers travel in average only half the distance of the layer thickness $d/2$. The integral of the (electron) current then yields only half the photogenerated charge $Q/2$.
Importantly, so far two important loss mechanisms have been neglected, bimolecular recombination of free charge carriers and diffusion. As discussed in Section 2.4 the rate of bimolecular recombination is given by

$$\frac{dn}{dt} = -k_{\mathrm{BR}} n^2, \tag{3.30}$$

with k_{BR} being the bimolecular recombination constant. From that an average charge carrier lifetime can be defined as the time at which the charge carrier density is reduced to $1/e$ of its initial value:

$$\tau = \frac{1}{k_{\mathrm{BR}} n}. \tag{3.31}$$

The charge carrier lifetime inversely depends on the carrier density and the experimental conditions should be chosen such to keep the extraction time much smaller than the lifetime ($t_{extr} = t_{tr} + 2RC \ll \tau$). This can be achieved for low carrier densities and low transit times, i.e. high collection voltages. Under such conditions, the RC time constant significantly prolongs the extraction time and should therefore be minimized. Otherwise, significant losses of photogenerated charge carriers due to recombination during extraction should be expected and the photocurrent integral does not correspond to the initial photogenerated charge. Recombination losses can be neglected, if they are lower than the experimental error, for example given by pulse-to-pulse laser fluctuations. The photocurrent integral should then increase linearly with increasing photogenerated charge carrier density, i.e. with increasing laser pulse fluence.
Diffusion of charge carriers has to be considered as a loss process only, if charge carriers happen to leave the device and recombine at the wrong electrode. However, at high collection fields, the charge carriers move away from the electrodes fast enough and diffusion losses can be neglected. Under pre-bias conditions, where the effective fields are usually much lower, diffusion losses can be avoided by applying very short delay times. If longer delay times at low fields are applied, for instance to probe

nongeminate recombination (see Section 4.3), and non-selective electrodes are used, diffusion losses at the wrong contact might alter the results.
If any losses of charge carriers are negligible Equation (3.29) is valid, independent of the applied bias and whether different biases are applied during extraction. Therefore, one can also write:

$$\begin{array}{rcccccl} \int_0^{t_{\mathrm{end}}} I_{photo} dt & = & \int_0^{t_{\mathrm{d}}} I_{photo} dt & + & \int_{t\mathrm{d}}^{t_{\mathrm{end}}} I_{photo} dt & & \\ Q_{\mathrm{photo}} & = & Q_{\mathrm{pre}} & + & Q_{\mathrm{coll}} & = & Q_{\mathrm{tot}}, \end{array} \tag{3.32}$$

see Figure 3.1 for comparison.

3.3 Summary

Within the context of this work, a Time Delayed Collection Field experiment with unprecedented high time resolution was set up, implying a voltage pulse rise time below 10 ns and a circuit RC time constant in the order of 20 ns. With that it is possible to study photogenerated charge carrier densities at different electric fields and after time delays in the order of a few ns to several μs.
A detailed theoretical analysis revealed that the shape of the photocurrent transient is largely influenced by external experimental parameters such as circuit RC time, height and rise time of the voltage pulse and charge carrier density, but also by intrinsic sample properties such as charge carrier mobilities and bimolecular recombination constants.
The integral of the photocurrent transient is equal to the photogenerated charge as long as the loss of carriers due to bimolecular recombination during the extraction time and time delay is negligible. To meet this important condition, it is necessary to choose the external parameters such that the photocurrent integral increases linearly with increasing carrier density. In general this is true for low carrier densities, i.e. low laser pulse fluences and high collection voltages.
Special attention has to be paid if extrapolation of the photocurrent decay is used to determine charge carrier mobilities, since the RC time constant of the external circuit significantly influences the effective extraction time. It has been shown that the true carrier transit time can be obtained by correcting the measured extraction time by $2RC$. Therefore, knowledge of the exact RC time of the set-up including the particular sample structure is of vast importance. Here, two different routines were presented to obtain the RC constant from the TDCF dark transients.
Furthermore, it has been shown that the numerical simulation described in Section 2.7.2 perfectly reproduces the considered physical processes. This provides a powerful tool to analyse photocurrent transients even under conditions that may not be analytically attackable anymore, i.e. when bimolecular recombination and diffusion become important or time dependent mobilities or recombination constants occur.
The theoretical framework delivered in this chapter is the basis for the experimental analysis of charge carrier generation, recombination and transport processes in organic solar cells, which will be discussed in the upcoming chapter.

4 TDCF - Experimental Applications

4.1 Introduction

The characteristic *J-V* response of organic solar cells is determined by the free charge carrier generation via dissociation of charge transfer states in competition with geminate recombination and by the efficiency of carrier extraction in competition with non-geminate recombination. Earlier work on the dynamic processes in solar cells have often focused on only one or two of these parameters, e.g. only generation and recombination [17, 26, 27] or only charge carrier mobilities [28, 29]. This has often lead to incomplete and contradictory descriptions of the physical processes. However, here it will be shown that the thorough analysis of all three parameters in one device is essential to gain a deep understanding of the charge carrier dynamics and to identify the most relevant loss channels.

The Time Delayed Collection Field (TDCF) method, extensively discussed in Chapter 3, can be used to separately measure charge carrier generation, recombination and transport in organic photovoltaic devices. In the following this will be shown for two relevant material systems, P3HT:PCBM and PTB7:PCBM. A short summary of the chemical structures, solar cell performance and morphological features for these blends can be found in Section 2.8.

P3HT:PCBM has, for many years, been the most-studied benchmark system in the field of organic photovoltaics. With a total of over 1500 publications in the last 10 years it is the 'fruit-fly' among the donor-acceptor bulk heterojunction (BHJ) solar cells.[149] However, this system is also particularly interesting as thermal or vapor annealing leads to a huge increase in the short circuit current density (J_{SC}) and fill factor (FF), along with an overall efficiency improvement by up to one order of magnitude.

Extensive studies in recent years have been devoted to the influence of annealing on the the morphology of the blend. Thermal treatment has been shown to cause a coarsening in size and order of the crystalline P3HT domains, accompanied by aggregation of PCBM molecules. The resulting morphology can be best described by an interpenetrating network of rather pure nanometer-sized crystalline domains.[114, 116–119, 150, 151] Alternative annealing techniques such as slow drying or vapor annealing were shown to result in a similar phase separation of the components.[11, 117, 152, 153] However, the origin of the beneficial effect of annealing on the solar cell performance, especially on the charge generation process, was still controversially discussed at the beginning of this work.

BHJ solar cells comprising the low bandgap donor polymer PTB7 and the fullerene acceptor PCBM yielded a record power conversion efficiency of 9.2% [30], which was the highest certified efficiency for single junction organic solar cells to date. However, also for this material combination the device properties depend largely on the processing conditions. In particular, the photovoltaic performance improves dramatically when adding 1,8-diiodooctane (DIO) to the blend solution [120] which is attributed to an optimized phase-separated structure. Although the change in nanomorphology upon addition of DIO has already been extensively discussed in

literature [123, 124, 154–156], a conclusive picture is still under debate. On the other hand, comparatively few publications so far have dealt with the impact on the charge carrier dynamics.[26, 28, 157]
In this chapter the influence of processing conditions on charge carrier generation, recombination and transport in these two highly relevant OPV material systems is investigated. One of the main goals of this work is to understand the $J-V$ characteristics from Figure 2.12 and 2.14 on the basis of the charge carrier dynamics. The results are discussed with respect to previous literature studies and also in terms of the specific blend morphologies.

4.2 Charge Carrier Generation

As discussed in the beginning of Chapter 3, TDCF was originally developed to investigate the charge carrier generation process. By applying different voltages relevant for solar cell operation during laser excitation (pre-bias, V_{pre}) and subsequent collecting the photogenerated charge carriers, the bias dependent efficiency of free carrier formation can be probed. The active area of all devices investigated in this chapter was 1 mm^2.
As already pointed out, the integral of the total current transient over delay time and collection time corresponds to the photogenerated charge as long as non-geminate recombination during delay and collection time is negligible. To meet this condition, in all generation experiments the delay time was chosen sufficiently short (between 10 and 20 ns) and the collection bias was chosen high enough to extract all charge carriers ($V_{\mathrm{coll}} = -5$ V for the 200 nm P3HT:PCBM device and $V_{\mathrm{coll}} = -2.5$ V for the

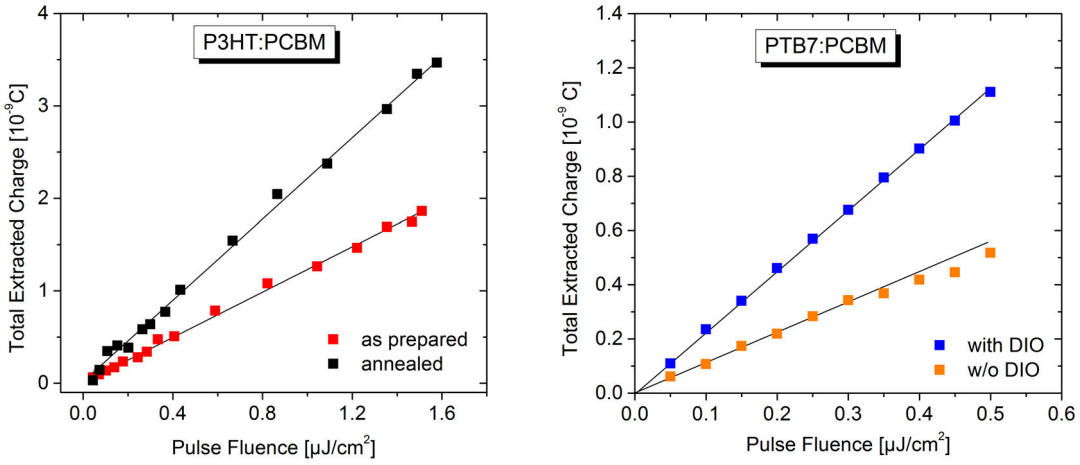

Figure 4.1: Total extracted charge measured with TDCF as a function of laser pulse fluence for P3HT:PCBM (left) and PTB7:PCBM (right) devices. The straight lines are guides to the eye. The strict linear increase in all cases indicates that bimolecular recombination losses during extraction can be excluded under the chosen experimental conditions (P3HT:PCBM: $V_{\mathrm{pre}} = 0.55$ V, $V_{\mathrm{coll}} = -5$ V, $t_{\mathrm{d}} = 20$ ns; PTB7:PCBM: $V_{\mathrm{pre}} = 0.7$ V, $V_{\mathrm{coll}} = -2.5$ V, $t_{\mathrm{d}} = 10$ ns).

100 nm PTB7:PCBM device). The collection time was sufficiently long (between 2 and 5 μs), so that the photocurrent signal has well dropped below the noise level, to make sure that all free moving charge carriers are collected. Figure 4.1 shows the photocurrent integral as a function of laser pulse fluence for as prepared and thermally annealed P3HT:PCBM devices (left) and PTB7:PCBM blends, prepared with and without the solvent additive DIO (right). In this measurement V_{pre} was chosen close to the open circuit voltage (V_{OC}) at one sun illumination. The strict linear increase of the total extracted charge with pulse fluence in all cases indicates that non-geminate recombination is absent during the experiment for the chosen parameters and the measurement is sensitive for bias-dependent geminate recombination losses.

4.2.1 P3HT:PCBM

In this section the results for as prepared and annealed CF-cast P3HT:PCBM devices are summarized and discussed. Figure 4.2 shows the total extracted charge as a function of the applied pre-bias during generation. In this experiment the time delay was 20 ns and the pulse fluence was 0.7 μJ/cm^2. It is obvious that the photogenerated charge is independent of the bias for both blends within an experimental error of 10%. Therefore, the presence of an electric field does not suppress geminate recombination or increases the number of free charge carriers. This analysis presumes that the generation of free charge carriers is completed within the delay time, meaning that all CT states are either separated or have recombined. This presumption is justified by the short CT lifetimes of several ps to a few ns determined by optical measurements.[21, 50, 60–63]

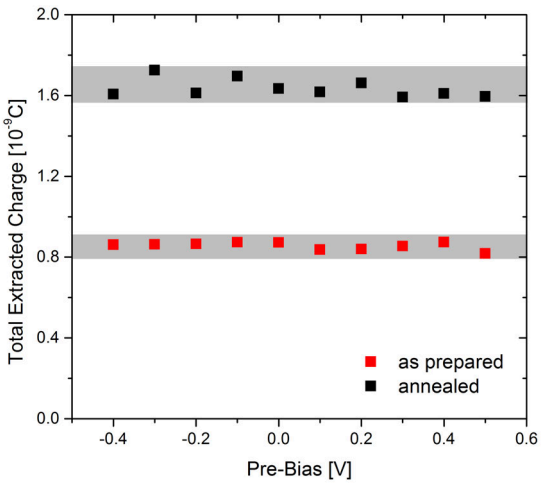

Figure 4.2: The total extracted charge is independent of the applied pre-bias during laser excitation for the annealed and as prepared P3HT:PCBM samples. The time delay was 20 ns and the pulse fluence was 0.7 μJ/cm^2. The grey areas indicate a 10% range around the mean value.

These results show for the first time, directly and unambiguously, that the charge carrier generation process in the much debated P3HT:PCBM system is independent of an electric field and does not account for the field-dependent photocurrent.
This conclusion is in apparent contradiction to a recent transient absorption spectroscopy (TAS) study by Marsh et al. [19] There, the prolonged lifetime of the hole-related spectral feature upon increasing electric field was interpreted as evidence that field induced polaron pair dissociation suppresses geminate recombination. However, this data can be alternatively explained assuming a higher electron mobility compared to the hole mobility. The rapid extraction of electrons under a negative bias then leads to reduced bimolecular recombination in the remaining hole population, which is especially significant under the high laser fluences of 12 μJ/cm^2 used in this study. Consequently, the hole lifetime is increased.
On the other hand, a bias-independent generation process is in accordance with earlier TAS studies by Howard et al. and Guo et al. [21, 22], which indicated direct generation of free charges within a few picoseconds. For the annealed device, a field-independent fast free carrier generation is expected from the high FF of about 67% [11], implying high currents and generation yields even at very low internal fields.
Interestingly, the total charge is also independent of pre-bias in the as-prepared device. This result is unexpected since chloroform-cast as-prepared devices exhibit very low FF and currents, the origin of which was so far very controversially discussed. Mihailetchi et al. suggested that the FF and J_{SC} in these devices is limited by build-up of space charge, brought about by a large difference in the hole and electron mobility.[25] Additionally, they argued that the J_{SC} is further limited by the incomplete dissociation of electron-hole pairs at the donor-acceptor interface. Upon annealing the hole mobility strongly increases and space charge effects are absent.
Other studies using TAS reported a significant increase in the yield of dissociated charges upon annealing that was also ascribed to an enhanced efficiency of charge separation.[158] These studies were performed in the absence of an electric field and with pulse fluences well above 4 μJ/cm, where nonlinear effects begin to dominate the processes. Several publications stated a higher rate coefficient for non-geminate recombination in as prepared devices and proposed this to be the main cause for the lower FF.[134, 159]
Our results show unambiguously, that field-assisted generation of carriers in competition with monomolecular recombination of geminate pairs is insignificant even in the as prepared blend and cannot account for the low FF. These findings agree with conclusions from TAS measurements, that exciton dissociation at the heterojunction is followed by rapid formation of free charge carriers also in as prepared devices.[21]
It can be concluded, that field-independent free carrier generation is quite general for P3HT:PCBM blends over a wide range of morphologies and efficiencies. It has been postulated, that free carrier generation in P3HT-based solar cells is assisted by the delocalization of holes along fully conjugated segments.[160] Turner et al. used linear absorption spectroscopy to show that as-prepared chloroform-cast layers already contain a significant number of aggregated chains.[118] Eventually, the

number of aggregated P3HT chains on as-prepared samples seems to be sufficiently high for the efficient photogeneration of free carriers.

A second important observation can be made from Figure 4.2. The amount of extracted charge in the annealed device is approximately a factor of 1.8 higher than in the as prepared device. The excitation wavelength was chosen to 450 nm, where the optical absorption coefficient is equal in both devices (see absorption spectra in Section 2.8). Although this observation points to less efficient charge generation in the as-prepared blend, it is noted that the hole mobility in blends of P3HT with PC[60]BM was reported to be very small, in the order of 10^{-7} cm^2/Vs.[25] Under these conditions, hole extraction with a typical collection bias of -5 V and a collection time of 2 μs is insufficient. In fact, even longer extraction times did not result in a measurable difference in the extracted charge. For a photogenerated charge of 10^{-9} C and a mobility of 10^{-7} cm^2/Vs, the extraction current would be in the order of 10^{-6} A, which is below the resolution limit of the oscilloscope. It is therefore reasonable to conclude, that the photocurrent in as prepared blends is only due to moving electrons and the extracted charge in the TDCF experiment accounts for about half the photogenerated charge. Remarkably, this suggests almost equally efficient free charge generation in both, the as-prepared and the annealed devices. This is in accordance with a study by Howard et al., who reported only a small difference (ca 20%) in the amount of photogenerated charge measured by TAS.[21]

4.2.2 PTB7:PCBM

Similar to annealed P3HT:PCBM devices, optimized PTB7:PCBM solar cells with the sovent additive DIO show exceptional high FF in the order of 70% (Figure 2.14). In accordance with such high photocurrents even at low internal fields, the charge generation was measured to be independent of the applied bias. The results are shown in Figure 4.3 (left). These experiments were performed with an excitation density of 0.05 μJ/cm^2 and a wavelength of 500 nm. The total extracted charge Q_{tot} was normalized to the respective value at -2 V and smoothed with a third-order polynomial.
In contrast the devices prepared without DIO show a significant field dependence of the free charge generation efficiency. Here about 20% less charge is generated at open circuit voltage (V_{OC}) compared to -2 V. Since non-geminate recombination was excluded in this experiment, the field-dependence can only be attributed to geminate recombination losses at low internal fields.
The inset of Figure 4.3 shows the original data. About 40% less charge is extracted in the devices without DIO as compared to blends with DIO, indicating an overall lower free carrier generation rate also at high internal fields. This is in accordance with a larger phase separation in those blends implying a smaller donor-acceptor interface for exciton splitting. Several groups reported a large phase separation in pristine blends with domains in the order of >100 nm and showed that the main effect of DIO is to suppress the formation of the large fullerene clusters, leading to a smaller length scale of the polymer and fullerene phases and an increase of the effec-

tive interfacial area.[120, 123, 124] Our measurements are in agreement with these reports. Notably, though the generation rate without DIO is considerably smaller than with DIO, the photon absorption efficiency is equal in both blends (see Section 2.8 for the absorption spectra), meaning that the internal quantum efficiency is reduced in blends without DIO.
To further clarify the origin of the geminate losses in pristine devices, the field-dependence of the generation was investigated for different excitation wavelengths (Figure 4.3, right). Note that the overall field-dependence in the right graph is slightly smaller than in the left graph, as these experiments were performed later on a blend with a different batch of PTB7. We observe a smaller field-dependence of generation in the blue region (405 nm) where PCBM is predominantly excited (see absorption spectra of PCBM and PTB7 in Section 2.8). Here, about 5% less charges are generated at V_{OC} compared to -2 V. In contrast, if PTB7 excitation dominates (600 nm) the generation rate drops approximately by 12% when going from reverse bias to open circuit conditions. This observation is consistent with a recent study by Brenner et al. reporting a stronger voltage dependence of the polymer photocurrent generation in the devices without additive by means of voltage-dependent EQE measurements.[161] A greater field-dependent generation upon polymer excitation indicates that not all the excitons created in the polymer phase are sufficiently separated into free charge carriers at the donor/acceptor interface. Apparently, a significant fraction of the polymer excitons form bound CT states across the interface that need the aid of an electric field to be fully separated.

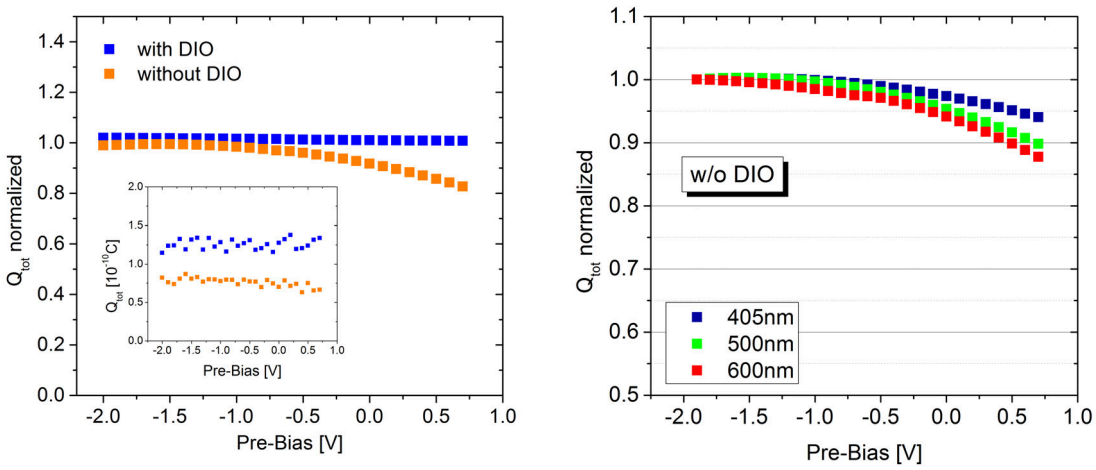

Figure 4.3: Left: Total extracted charge (Q_{tot}) as a function of the applied pre-bias during laser excitation at 500 nm, smoothed and normalized to Q_{tot} at -2 V. The pulse fluence was 0.05 μJ/cm^2 and the time delay was 10 ns. The free carrier generation is independent of the applied bias in the device with DIO. Without DIO ~20% less charge is generated at V_{OC} compared to -2 V. The inset shows the raw data. Right: Charge carrier generation of a device without DIO at 3 different wavelengths. The field-dependence is stronger if PTB7 is predominantly excited (600 nm, red) as compared to PCBM excitation (400 nm, blue).

A morphological X-ray study by Collins et al. showed that in blends without DIO, pure agglomerated fullerene domains in the order of 200 nm in size are embedded in a polymer-rich matrix containing 30% dispersed PCBM.[123] Because of the large dimensions of the domains, well exceeding the exciton diffusion length, a significant fraction of PTB7-excitons are not able to reach an agglomerate interface within their lifetime but are quenched at dispersed PCBM molecules within the matrix.
Furthermore, it was shown recently that fullerene agglomerates have a deeper lying LUMO than dispersed molecules in the matrix, leading to a higher LUMO offset between donor and acceptor and, therefore, reducing the probability of geminate or non-geminate recombination.[162] Other studies suggest that the presence of fullerene aggregates is required for strong electron delocalization and ultrafast long-range charge separation as discussed in Section 2.3.2.[68, 139, 163] In either case, charge transfer states between polymer chains and dispersed fullerenes in large and highly intermixed domains, with no fullerene agglomerates in close vicinity, are expected to suffer from geminate recombination and a higher field-dependence of charge separation. This situation is schematically depicted in Figure 4.4.
In blends with DIO the dimensions of the fullerene and polymer domains are in the order of 30 nm.[123] Therefore, an agglomerate interface is always within the exciton diffusion length and all quenched excitons are efficiently separated into free charge carriers. Consequently the generation rate is not expected to depend on the electric field in those devices. The results of the TDCF measurements are in very good agreement with these morphological models.

In summary, TDCF measurements provided for the first time direct access to geminate recombination losses in the free carrier generation process of two relevant OPV systems. In three of the four investigated BHJ solar cells the charge carrier genera-

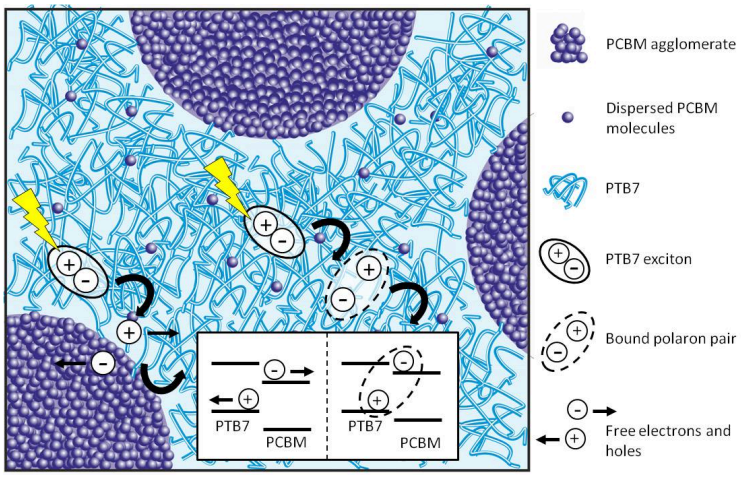

Figure 4.4: Schematic image of the morphology in devices without DIO based on structural studies by Collins et al.[123] Charge generation is field-independent close to the agglomerate interfaces and field-assisted in the matrix, where only dispersed PCBM molecules are available for charge transfer.

tion process proved to be independent of the electric field.
These results challenge the current role of the CT state. While its existence has undoubtedly been proven for a variety of donor-acceptor combinations, including the ones studied here, by means of photophysical methods [42, 44, 45, 66, 164], the general importance of these states in limiting charge photogeneration still remains questionable. Quantum mechanical studies and optical measurements indicate that the properties of CT states are strongly related to the molecular nature of the interface and that the role in the charge generation process may vary significantly between different material systems.[52, 53, 86, 165] In all three cases where field-independent generation was observed, the blend morphology comprises nanometer-sized crystalline or aggregated polymer or fullerene domains. It is proposed that these domains stabilize free charges away from the interface and prevent them from geminate recombination. In contrast, the blend with large amorphous PTB7 domains containing dispersed PCBM, suffers from geminate recombination losses of about 20%.
Obviously, in a number of state-of-the-art BHJ solar cells, free carrier generation is not limited by field-assisted splitting of strongly bound interfacial polaron pairs. In these devices the bias dependent photocurrent must be of different origin. Therefore, the fate of charge carriers after the photogeneration process will be investigated in the next section.

4.3 Non-geminate Recombination

After the photogeneration process, the free charge carriers are either extracted by an applied electric field or they recombine non-geminately and are lost to the photocurrent. At flat band conditions, close to the open circuit voltage at one sun illumination, where no effective field is operating, all charge carriers are condemned to recombination. Under these conditions, TDCF can be applied to probe the recombination dynamics in the solar cell by varying the time delay between the laser pulse and the extraction pulse.[4]
If the delay after excitation is increased, the charge carriers have more time to recombine and, consequently, less charge is extracted with the collection pulse. The photocurrent integral over the time of the collection pulse is equal to the photogenerated charge Q_{coll} still present in the device after the delay t_{d} and is decreasing with increasing delay (see Figure 3.1 for a schematic description of Q_{coll}, Q_{pre} and Q_{tot}).
If the effective electric field during the delay is not exactly zero, charge carriers start moving and a photocurrent signal is also recorded prior to the collection pulse. The integral of the photocurrent during the delay time is called pre-charge Q_{pre} and is equal to the charge extracted by the electrodes under pre-bias conditions during the

[4] At this point it should be noted that V_{OC} is not a meaningful definition in a TDCF experiment, since it is a dynamic quantity that depends on the carrier density in the device. In this chapter the V_{OC} at one sun is used as a reference value for the applied pre-bias. This approach is justified as carrier densities generated in TDCF are of the order of carrier densities at one sun illumination.

delay. The total charge Q_{tot} is the sum of Q_{coll} and Q_{pre} and measures the total photogenerated charge that survives recombination and is collected by the electrodes. If the delay is slightly increased from t_{d} to $t_{\mathrm{d}} + \Delta t$, the total charge is reduced by the amount of charge $\Delta Q_{\mathrm{coll}}^{\mathrm{rec}}(\Delta t)$ that has recombined in Δt:

$$\begin{aligned} Q_{\mathrm{tot}}(t_{\mathrm{d}} + \Delta t) &= Q_{\mathrm{coll}}(t_{\mathrm{d}} + \Delta t) + Q_{\mathrm{pre}}(t_{\mathrm{d}} + \Delta t) \\ &= Q_{\mathrm{coll}}(t_{\mathrm{d}}) + Q_{\mathrm{pre}}(t_{\mathrm{d}}) - \Delta Q_{\mathrm{coll}}^{\mathrm{rec}}(\Delta t) = Q_{\mathrm{tot}}(t_{\mathrm{d}}) - \Delta Q_{\mathrm{coll}}^{\mathrm{rec}}(\Delta t). \end{aligned} \tag{4.1}$$

The number of recombined charge carriers $\Delta n(\Delta t) = \Delta Q_{\mathrm{coll}}^{\mathrm{rec}}(\Delta t)/eAd$ can be determined with an appropriate model for non-geminate recombination. In case of bimolecular recombination it is:

$$R_{\mathrm{BMR}} = \frac{\Delta n}{\Delta t} = -kn^2(t_{\mathrm{d}}), \tag{4.2}$$

with k being the bimolecular recombination (BMR) coefficient. Assuming that

$$n(t_{\mathrm{d}}) = Q_{\mathrm{coll}}(t_{\mathrm{d}})/eAd, \tag{4.3}$$

the temporal evolution of Q_{coll} can be described as follows:

$$Q_{\mathrm{coll}}(t_{\mathrm{d}} + \Delta t) = Q_{\mathrm{coll}}(t_{\mathrm{d}}) - [Q_{\mathrm{pre}}(t_{\mathrm{d}} + \Delta t) - Q_{\mathrm{pre}}(t_{\mathrm{d}})] - k\frac{Q_{\mathrm{coll}}^2(t_{\mathrm{d}})}{eAd}\Delta t. \tag{4.4}$$

Equation (4.4) can be used to iteratively calculate the collected charge for each time step and, by comparing to the experimental results, the recombination dynamics in the device can be resembled and, for instance, the BMR coefficient k can be extracted.
However, the derivation of Equation (4.4) contains three important approximations. First, as discussed in the previous chapter, it is assumed, that non-geminate recombination is absent during the collection of the remaining charges after t_{d}. For a correct analysis, therefore, a sufficiently high collection bias has to be applied.
Second, bimolecular recombination reduces the carrier density only where the density profiles of electrons and holes overlap. In the above analysis it is assumed, that the density profiles completely overlap, which is a reasonable assumption, considering uniform charge generation by a short laser pulse in the absence of an electric field. In case, the density profiles of holes and electrons only partly overlap, the evaluation with Equation (4.4) will underestimate the true local recombination coefficient.[82]
The third and probably most critical approximation is given by Equation (4.3), which assumes that the charge carriers remaining in the layer after t_{d} still travel an average distance of $d/2$ before being extracted at the electrodes. This, however, is only true if the displacement of the charges during the delay is very small compared to the layer thickness d and if diffusion, space charge effects or dispersive transport spread the charge density profile, so that the charge carriers can be considered to be rather uniformly distributed across the layer.
If the experimental conditions are chosen to satisfy these approximations, the BMR coefficient k can be reliably extracted from the measurement as is demonstrated

in Figure 4.5 (left). To confirm that the iterative analysis described above yields reasonable values for k, the numerical drift-diffusion simulation described in Section 2.7.2 was used to simulate the collected charge after different time delays in the range of 20 ns to 10 μs. In this simulation the effective electric field during the delay was set to zero, so that $Q_{\mathrm{pre}} = 0$ for all delays. Also, non-injecting contacts were used to minimize dark injection. The BMR coefficient in the simulation was set to $k_1 = 1 \times 10^{-18}$ m^{3}s^{-1}, $k_2 = 5 \times 10^{-18}$ m^{3}s^{-1} and $k_3 = 1 \times 10^{-17}$ m^{3}s^{-1} (black, red, green symbols respectively). The solid lines are the best fits to the data, using Equation (4.4) and leaving k as the free fit parameter. $Q_{\mathrm{coll}}(t_{\mathrm{d}} = 0) = Q_0$ is the initial photogenerated charge and is taken from the photocurrent integral of the transient at the shortest delay. The extracted BMR coefficients using the iterative fit function are very close to the input values ($k_1 = 0.95 \times 10^{-18}$ m^{3}s^{-1}, $k_2 = 4.2 \times 10^{-18}$ m^{3}s^{-1}, $k_3 = 0.8 \times 10^{-17}$ m^{3}s^{-1}), demonstrating the validity of Equation (4.4) at low electric fields during pre-bias conditions.
If, however, lower pre-biases, i.e. higher effective electric fields, are applied during the delay, the charge carriers may already move a considerable distance towards the collecting electrodes. Upon the application of the collection pulse, the average distance traveled by the carriers will be less then $d/2$. Consequently, the true carrier density will be larger than the one calculated from $Q_{\mathrm{coll}}(t_{\mathrm{d}})$ with Equation (4.3) and the application of Equation (4.4) to the experimental data will overestimate the recombination coefficient, as shown in Figure 4.5 (right). The input parameters are the same as in the left graph, however, during the delay a small effective bias of -0.1 V was applied. In this case, the extracted BMR coefficients are up to 60%

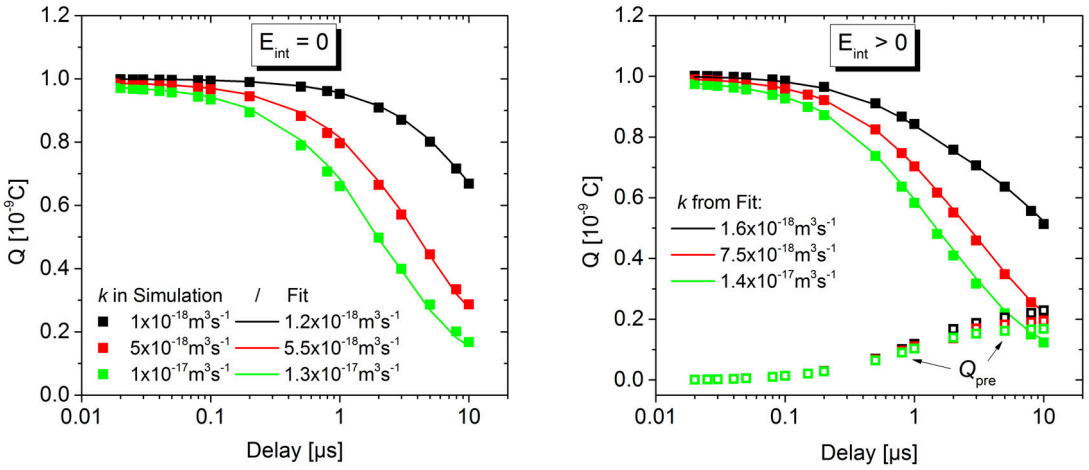

Figure 4.5: Drift diffusion simulation (symbols) of the recombination dynamics after a homogeneous inserted carrier density for three different k values. Parameters of the simulated sample: $d = 200$ nm, $E_{\mathrm{LUMO}} = -3.6$ eV, $E_{\mathrm{HOMO}} = -4.8$ eV, $E_{\mathrm{anode}} = E_{\mathrm{cathode}} = -4.2$ eV. Left: The internal field during the time delay is exactly 0 ($V_{\mathrm{pre}} = 0$). Right: A small internal field is applied during delay. ($V_{\mathrm{pre}} = -0.1V$) The solid lines are fits with Equation (4.4). The obtained k values are shown in the graph.

higher than the input values. This effect increases with increasing effective field and, therefore, measurements taken under such conditions should be analysed with care.

4.3.1 The Presence of Dark Charges

The last section motivated the desire to apply pre-biases close to the open circuit voltage (at one sun) to minimize the effective electric field during delay in the recombination experiments. However, at forward bias in the vicinity of V_{OC} some devices show significant dark currents, arising from charge injection via the electrodes. Consequently, in these devices a considerable amount of dark charge is present at a pre-bias close to V_{OC}, as shown in Figure 4.6. The injected charge at a certain pre-bias V_{pre} can be determined with the TDCF set-up by recording the dark transient with collection voltage V_{coll} and subtracting a reference dark transient taken at $V_{\mathrm{pre}} = 0$, where injection of carriers is negligible, with collection voltage $V_{\mathrm{coll}} + V_{\mathrm{pre}}$ to negate the capacitance effects. The integral of the difference-transient yields the additionally injected charges at V_{pre}.
Figure 4.6 shows the injected dark charge as described above for different applied pre-biases for annealed P3HT:PCBM (left) and PTB7:PCBM with and without DIO (right). In all three devices the injected dark charge is negligible at low pre-biases and shows a steep increase towards and above the V_{OC} at one sun. For typical pre-bias conditions in the recombination experiments (dashed lines in the graph), Q_{dark} is significantly high, especially in the case of annealed P3HT:PCBM. Here, for low excitation fluences (typically generating a charge in the order of 10^{-10} C) it strongly exceeds the photogenerated charge. However, in the TDCF experiment, the dark charge is not recognized as part of the collected charge, as the dark current transient is always subtracted from the transient under illumination. On the other hand, the

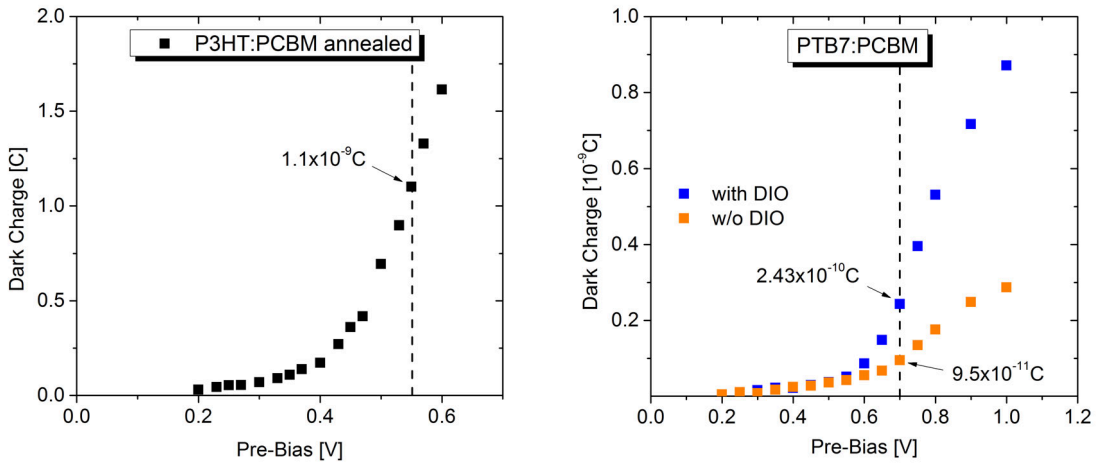

Figure 4.6: Dark Charge for annealed P3HT:PCBM (left) and PTB7:PCBM (right) as a function of applied pre-bias. For the as prepared P3HT:PCBM device no dark charge could be measured up to $V_{\mathrm{pre}} = 1V$. The dashed lines indicate typical pre-bias conditions for the recombination experiments.

background charge carriers take part in the bimolecular recombination, and their presence accelerates the decay of the photoinduced charge population. Thus, if the dark charge is not properly taken into account in the evaluation of the data, the BMR coefficients will be strongly overestimated as is demonstrated clearly in Figure 4.7. To account for the dark charge Q_{dark} in the iterative analysis, Equation (4.4) has to be modified to:

$$Q_{\mathrm{coll}}(t_{\mathrm{d}}+\Delta t) = Q_{\mathrm{coll}}(t_{\mathrm{d}}) - [Q_{\mathrm{pre}}(t_{\mathrm{d}}+\Delta t) - Q_{\mathrm{pre}}(t_{\mathrm{d}})] - \frac{k}{eAd}[Q^2_{\mathrm{coll}}(t_{\mathrm{d}}) + 2Q_{\mathrm{coll}}(t_{\mathrm{d}})Q_{\mathrm{dark}}]\Delta t. \tag{4.5}$$

The derivation of Equation (4.5) is shown in the appendix A.3.
Figure 4.7 shows drift-diffusion simulations with a constant background charge of $Q_{\mathrm{dark}} = 1 \times 10^{-10}$ C. The input BMR coefficient was $k = 5 \times 10^{-18}$ m^{3}s^{-1} for all simulations, and the photogenerated charge Q_0 set to $2Q_{\mathrm{dark}}$ (black symbols), Q_{dark} (red symbols) and $0.5Q_{\mathrm{dark}}$ (green symbols). The solid lines are the best fits using Equation (4.4), therefore ignoring the dark charge. Apparently, also reasonable fits can be achieved in this way, however the extracted BMR coefficients exceed the true value in all cases. If the dark charge exceeds the photogenerated charge by a factor of 2, the extracted k exceeds the true value even by a factor of 5.
The dashed lines are the best fits including the dark charge in the analysis (Equation (4.5)). In this case the extracted BMR coefficients are very close to the input value in all cases, demonstrating the importance of taking into account injected dark carriers in the analysis of bimolecular recombination coefficients.

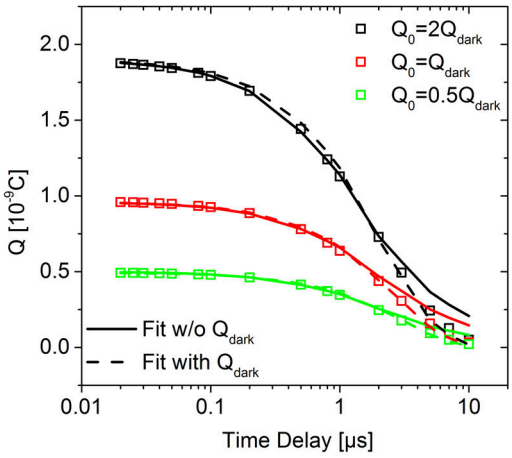

	k ignoring Q_{dark} [m^{3}s^{-1}]	k including Q_{dark} [m^{3}s^{-1}]
$Q_0 = 2\ Q_{dark}$	1×10^{-17}	4×10^{-18}
$Q_0 = Q_{dark}$	1.4×10^{-17}	4×10^{-18}
$Q_0 = 0.5\ Q_{dark}$	2.5×10^{-17}	4×10^{-18}

Figure 4.7: Drift diffusion simulation (symbols) with a constant background charge of $Q_{\mathrm{dark}} = 1 \times 10^{-10}$ C, a constant BMR coefficient $k = 5 \times 10^{-18}$ m^{3}s^{-1} and three different initial photogenerated charge Q_0. The solid lines are fits without accounting for Q_{dark} (Equation (4.4)), the dashed line fits include Q_{dark} (Equation (4.5)). The obtained k values are presented in the table.

4.3.2 P3HT:PCBM

In this section the results for the recombination dynamics in the annealed and as prepared P3HT:PCBM devices are summarized. Figure 4.8 (left) shows the collected charge of the annealed sample as a function of time delay at four different laser pulse fluences. The pre-bias was kept close to open circuit conditions ($V_{\mathrm{pre}} = 0.55$ V), minimizing the internal field and charge extraction during the delay, so that the loss of the collected charge is mostly due to non-geminate recombination. The data can be consistently fitted with the model according to Equation (4.5) (solid lines). The good agreement between the data and the iterative fit suggests bimolecular recombination to be the dominant loss channel at longer delay times.
Proper consideration of the dark charge (of 1.1×10^{-9} C) yields values for k between 1.1×10^{-18} $\mathrm{m^3 s^{-1}}$ and 1.4×10^{-18} $\mathrm{m^3 s^{-1}}$, slightly increasing with increasing laser intensity. This very slight increase of k with fluence excludes significant contributions from higher-order recombination processes. The overall magnitude of k is comparable with values reported in literature [22, 166–168], however most of these studies reported a more pronounced increase of the recombination coefficient with carrier density, which was explained by a carrier density-dependent mobility in the presence of energetic disorder.
For further validation of the rather weak dependence of k on carrier density in the annealed P3HT:PCBM devices found here, TDCF experiments were carried out with a constant white light background illumination (using four focused white light LEDs; Lumileds Rebel). The fluence of the laser pulse was kept constant at 0.4 μJ/cm^2 and the background illumination was varied between 0 and 300 mW/cm^2. The results are shown in Figure 4.8 (right). As expected for bimolecular recombination, for

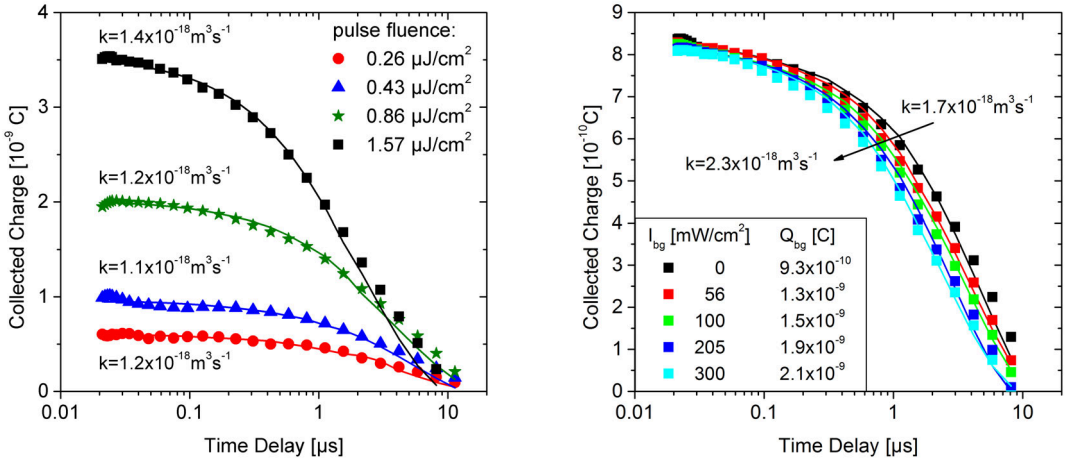

Figure 4.8: Left: Collected charge as a function of the time delay for annealed P3HT:PCBM at four different pulse fluences (V_{pre}=0.55 V, V_{coll}=5 V). Right: Collected charge as a function of time delay for a fixed laser fluence of 0.4 μJ/cm^2 and different steady state background illumination intensities I_{bg}. Solid lines are BMR fits according to Equation (4.5). The obtained k values are shown in the graph.

increasing background illumination the decay of the laser generated charge carriers measured as Q_{coll} becomes faster. Equation (4.5) can also be used to analyse the experiments with background illumination, by replacing Q_{dark} by the total background charge Q_{bg} in the device inluding the injected dark charge and the photogenerated charge from the LED illumination. Again, the BMR coefficients extracted from this data increase with increasing carrier density, but also here the increase is rather moderate.
The consistent fit to the data with Equation (4.5) for different pulse fluences and background charge shows, that the charge carrier dynamics in the annealed devices can be fully explained by the competition between extraction and bimolecular recombination, including a background carrier density and a weak dependence of the BMR coefficient on carrier density.
Though compared to annealed P3HT:PCBM devices, the as prepared devices show similar initial carrier densities, a much faster decay of the collected charge with increasing delay is observed. For a pulse fluence of 0.8 μJ/cm^2 the half life time in the as prepared sample is $\approx$ 450 ns and in the annealed sample $\approx$ 3 μs. Figure 4.9 shows the normalized decay curves of the collected charge, indicating the different half life times for the two devices. This is in good agreement with other studies on the kinetics of bimolecular recombination in those blends.[134, 159, 167]
Interestingly, no dark charge could be measured in the as prepared devices up to a voltage of 1 V. This is in accordance with a much lower dark current density in forward direction in this voltage regime. Figure 4.9 (right) shows the unnormalized Q_{coll} data at four different laser intensities. Again, the data can be fitted using the

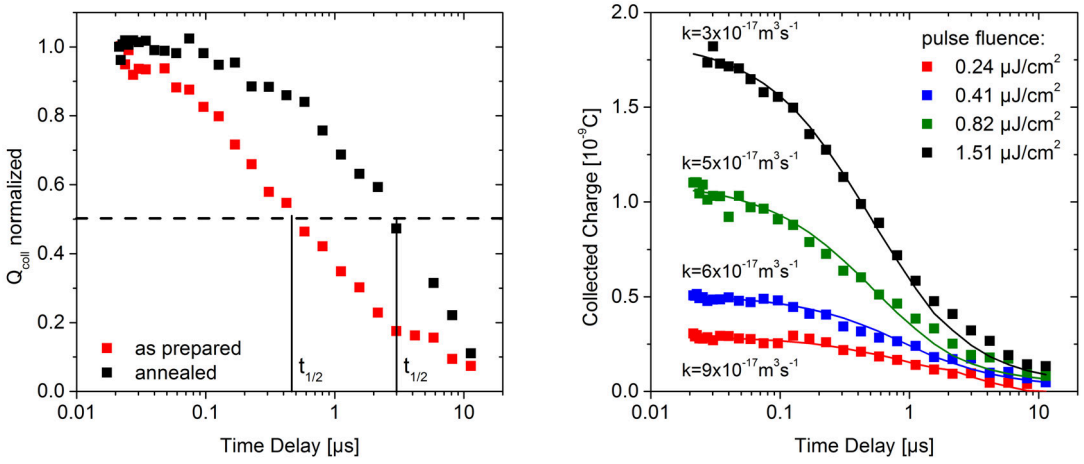

Figure 4.9: Left: Collected charge normalized to the initial charge as a function of time delay for as-prepared and annealed P3HT:PCBM devices for a pulse fluence of 0.8 μJ/cm^2. The decay dynamics in the as-prepared device are almost one order of magnitude faster than in the annealed device. Right: The recombination dynamics in the as pepared device are fitted with Equation (4.5), where Q_{dark} is set to zero. The obtained k values are shown in the graph.

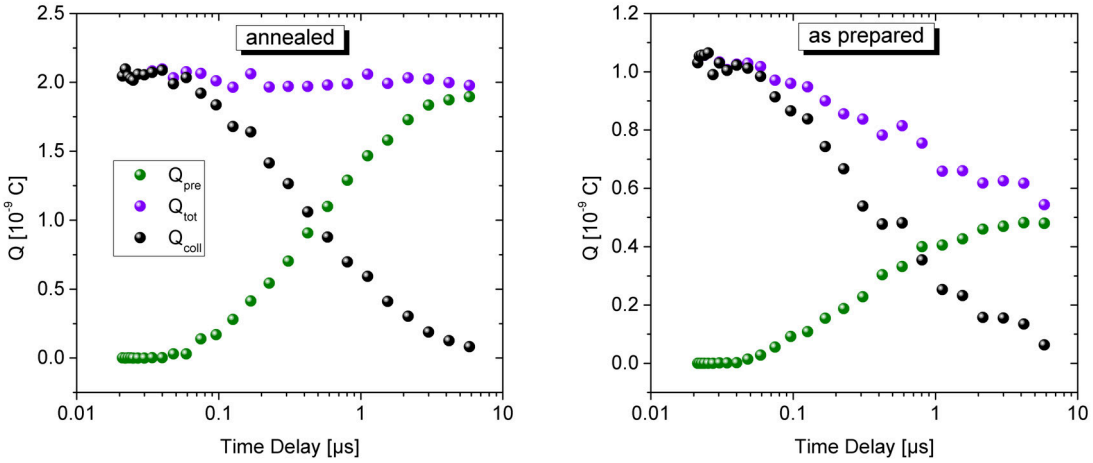

Figure 4.10: Q_{coll}, Q_{pre} and Q_{tot} as a function of time delay at V_{pre}=0 V (short circuit conditions) for the annealed (left) and as-prepared (right) P3HT:PCBM devices. The pulse fluence was 0.8 μJ/cm^2 in both cases. In the as prepared device, strong recombination losses lead to a rapid decay of Q_{tot}.

BMR model from above, setting the dark charge equal to zero (solid lines). It is also taken into account, that the charge inside the device is double the extracted charge, as holes are quite immobile in the as prepared blends. This will be shown in the next section. Interestingly, the extracted BMR coefficients slightly decrease with increasing laser intensity and, therefore, charge carrier density. This is in contradiction to common BMR models, see Langevin theory in Section 2.4.2, where k is determined by the carrier mobility and should therefore show, if any, a positive dependence on carrier density. Recently, Heeger and coworkers [169] proposed contributions from monomolecular trap-assisted recombination for P3HT:PCBM, however inclusion of this process in Equation (4.5) did not provide reasonable fits to the TDCF data and can be safely excluded.

Irrespective of the exact process determining the decay kinetics, the strongly reduced carrier lifetimes in the as prepared blends lead to significant recombination losses even at short circuit and for moderate fluences. Figure 4.10 shows Q_{coll}, Q_{pre} and Q_{tot} as a function of time delay at $V_{\text{pre}} = 0$ V (reflecting short circuit conditions) and a fluence of 0.8 μJ/cm^2. The increase of Q_{pre} is due to more charges being extracted during longer delay. The short carrier lifetime in the as-prepared devices leads to a rapid decay of the total charge with increasing delay, implying significant recombination losses and inefficient extraction of charge carriers at short circuit. In contrast, in the annealed device Q_{tot} stays constant over the observed time span, indicating little recombination losses and efficient charge carrier extraction at short circuit.

4.3.3 PTB7:PCBM

Following the procedure of the previous section, delay dependent TDCF measurements were also analysed for PTB7:PCBM devices prepared with and without DIO to gain insight into the recombination dynamics in these blends. Figure 4.11 (left) shows the decay of the collected charge at a pre-bias of 0.7 V (close to open circuit conditions), for similar photogenerated charge carrier densities (symbols) and the BMR fit according to Equation (4.5) (lines). In both cases a dark charge was included as determined from Figure 4.6, $Q_{\mathrm{dark}} = 2.43 \times 10^{-10}$ C (with DIO) and $Q_{\mathrm{dark}} = 9.5 \times 10^{-11}$ C (w/o DIO). The very good agreement between the data and the fits indicates that bimolecular recombination is the main loss mechanism at long delays in both blends, yielding BMR coefficients of $k = 1.6 \times 10^{-17}$ m^{3}s^{-1} for the device with DIO and $k = 4.5 \times 10^{-17}$ m^{3}s^{-1} for the device without DIO. For both types of blends the BMR coefficient varies only weakly with illumination intensity and, therefore, carrier density (data not shown). This excludes influence from higher recombination orders also in these devices.
The value for k with DIO is in very good agreement to recombination coefficients reported recently by Deledalle et al. for a similar carrier density of 3×10^{22} m^{-3}.[90] In contrast to this Rauh et al. observed a much lower BMR of only 5×10^{-18} m^{3}s^{-1} at the same carrier density.[168] Both of these values were obtained from charge extraction experiments without an additional extraction bias. The reasons for the discrepancies will be discussed in more detail in Chapter 5.4. BMR coefficients for the blends prepared w/o DIO have so far not been reported in literature.

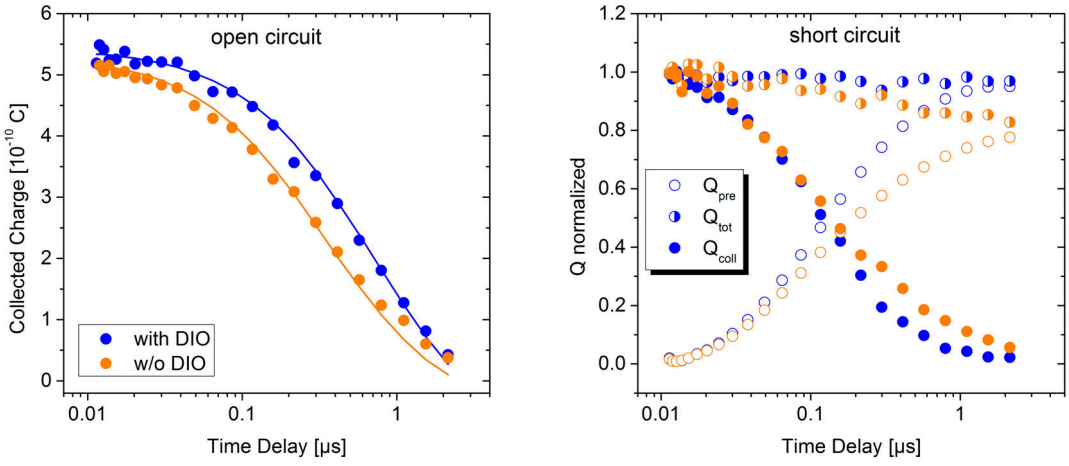

Figure 4.11: Left: Collected charge at open circuit conditions for increasing time delay with and w/o DIO for similar initial photogenerated charges. The pulse fluences were chosen 0.2 μJ/cm^2 and 0.6 μJ/cm^2, respectively, to generate similar carrier densities. The fits with Equation (4.5) (solid lines) reveal $k = 1.6 \times 10^{-17}$ m^{3}s^{-1} (with DIO) and $k = 4.5 \times 10^{-17}$ m^{3}s^{-1} (w/o DIO). A dark charge of 2.43×10^{-10} C (with DIO) and 9.5×10^{-11} C (w/o DIO) was included. Right: Normalized Q_{coll}, Q_{pre} and Q_{tot} at short circuit conditions. W/o DIO the extraction is less efficient.

Even though, in case of PTB7:PCBM, no significant dependence of k on V_{pre} was observed (data not shown), an important observation can be made from the dynamics at 0 V (short circuit). Figure 4.11 (right) displays the collected charge Q_{coll}, the total charge Q_{tot} and the pre-charge Q_{pre} as measured with TDCF for increasing time delay. Despite of a very similar decay of Q_{coll} in both blends, in the devices without DIO less Q_{pre} is extracted in the same time span. As a consequence Q_{tot} shows a significant decay, indicating severe losses at short circuit conditions, whereas in the blends with DIO Q_{tot} stays constant over the whole period. This is evidence for a slower and less efficient charge extraction in the devices without DIO.

In summary, delay dependent TDCF measurements are a powerful tool to analyse recombination dynamics in working OPV devices. By means of numerical simulations it was shown, that meaningful values for BMR coefficients can be obtained by analysing Q_{pre} and Q_{coll} with a specially developed fit routine. The consistent fit to the data at various initial carrier densities proves that the charge carrier dynamics in the investigated devices can be fully described by the competition of bimolecular recombination and extraction of carriers. A dark charge carrier density, arising from carrier injection at forward bias, has to be taken into account for the correct interpretation of the carrier dynamics. This result might also be important for the analysis of other transient experiments, such as photo-CELIV and charge extraction [145, 170], that use different biases during excitation and rely on the evaluation of the photocurrent.
Decay curves measured at $V_{\mathrm{pre}} = 0$ directly reveal whether or not non-geminate recombination losses are relevant at short circuit conditions and already allow some general conclusions about the device performance. However, PTB7:PCBM blends without DIO, exhibiting the highest values for k of the investigated devices, show a less rapid decay of Q_{tot} with time and also possess higher FF than as prepared P3HT:PCBM blends with a k-value of a factor of 4 lower. It is clear, that the loss of the total charge and the bias-dependence of the photocurrent are not solely determined by the BMR in the device, but also by the charge carrier transport. Imbalanced electron and hole mobility may lead to the build up of space charge at low internal fields, hindering the efficient extraction of both carrier types. Therefore, the consideration of charge carrier mobilities and the extraction kinetics are an important part in the complete analysis of the charge carrier dynamics in organic solar cells and shall be discussed in the following section.

4.4 Charge Carrier Transport

The previous section revealed a dynamic competition between recombination and efficient extraction of charge carriers in devices under illumination. In the absence of field-dependent generation, these two processes mainly determine the shape of the $J - V$ characteristics, emphasizing the importance of knowledge about the carrier extraction kinetics which are usually characterized by the charge carrier mobility. The direct measurement of mobilities in a working device is still quite challenging

and the results might depend strongly on the measurement conditions.[171] One straightforward method is to determine mobilities from TDCF transients by extrapolating the initial photocurrent slope upon application of the collection bias to zero, as described in Chapter 3.2. The advantage of this approach is that the mobility can be probed for different extraction fields and the laser intensity can be chosen such that the resulting carrier density is close to the carrier density of a working solar cell.
The results for the P3HT:PCBM and PTB7:PCBM devices are shown in Figure 4.12 (left and right, respectively). Here, the initial linear slope of the photocurrent transients at different extraction voltages was extrapolated to zero (as shown in the inset) to gain $t(I = 0)$. The charge carrier transit times t_{tr} and mobilities μ were then calculated according to:

$$t_{\mathrm{tr}} = t(I = 0) - 2RC \tag{4.6}$$

and

$$\mu = \frac{d^2}{t_{\mathrm{tr}} U_0} \tag{4.7}$$

where d is the device thickness and U_0 is the extraction voltage. The RC time was determined by analysing the dark current transients of each device as was exemplarily shown for the PTB7:PCBM devices in Section 3.2.1. For P3HT:PCBM the fit to the dark transient yielded RC time constants of 20 ns for the annealed device and 18 ns for the as prepared device. The complete resistance-capacitance analysis is presented in the appendix A.4.
Proper inclusion of the set-up RC time constant, according to Section 3.2.3, leads

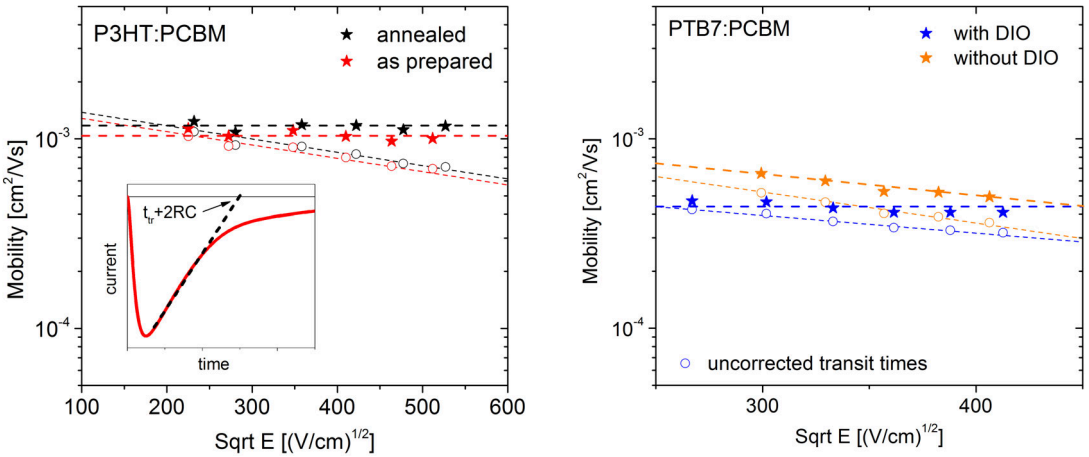

Figure 4.12: Charge carrier mobilities determined from extrapolation of TDCF transients in P3HT:PCBM (left) and PTB7:PCBM (right) devices. The stars include the subtraction of $2RC$. For comparison the data points not accounting for the RC time are also displayed (open circles) and show strong deviations. All dashed lines are guides to the eye. The inset shows the principle of photocurrent extrapolation.

to a field-independent mobility, in the relevant range for solar cells, for the devices of annealed P3HT:PCBM ($\mu = 1.2 \times 10^{-3}$ cm^2/Vs), as prepared P3HT:PCBM ($\mu = 1.0 \times 10^{-3}$ cm^2/Vs) and PTB7:PCBM with DIO ($\mu = 4.5 \times 10^{-4}$ cm^2/Vs). Contrarily, the PTB7:PCBM device without DIO exhibits a field-dependent mobility of $\mu_0 = 1.2 \times 10^{-3}$ cm^2/Vs and a Poole-Frenkel factor of $\beta = -0.002\sqrt{\text{cm/V}}$. Mobilities with a negative field dependence have occasionally been observed in TOF or CELIV experiments on high mobility materials [133, 172, 173] and have been attributed to strong spatial disorder, i.e. a broad distribution of intersite distances for charge carrier hopping, within the material. In the context of the Gaussian disorder model of charge transport [16], in the presence of large spatial disorder, an applied electric field prevents charge carriers from following hopping routes that involve sites that are spatially close but could only be reached by hopping in directions opposite to the electric field. This reduces the effective mobility until the electric field is large enough to considerably facilitate forward jumps.
Morphological studies on PTB7:PCBM blends revealed little crystalline content in the layers, suggesting mostly amorphous domains that are predestined for high spatial disorder. Especially in the blends prepared without DIO large amorphous intermixed PTB7-rich domains have been reported [123, 124, 154], indicating that the transport in these devices is indeed limited by a negative field dependence of the mobility.
It should be noted that if the extrapolated transit times are not corrected by $2RC$, the mobility data show a negative field-dependence for all devices, as is indicated by the small dots in Figure 4.12. Such a behaviour is implausible, especially for the highly ordered annealed P3HT:PCBM blend. It is a pure experimental artifact, due to the transit times not being long enough compared to the RC time of the set-up and highlights the importance of the correct data analysis according to Section 3.2.3.
The extrapolation of transit times from photocurrent transients is a fast and straight forward method to determine charge carrier mobilites. However, the initial slope of the current decay is defined by the fastest charge carriers only. As the total current is the sum of the electron and the hole current, it is in principle possible to determine a second linear slope of the transient at longer times, which can be attributed to the slower carrier type, if electron and hole mobility lie both within the resolution limit of the set-up. However, in most cases the photocurrent at longer times is affected by diffusion of charge carriers and a mobility dispersion, making it difficult to unambiguously extract a second linear slope. Also, if the mobility of the slower carrier type is much lower than the mobility of the faster carriers, the currents may drop below the resolution limit of the oscilloscope.
An alternative way to extract the charge carrier mobility also of the slower carrier type is to use the drift-diffusion simulation from Section 2.7.2 to fit whole TDCF transients at different biases and delays. The advantage of the numerical simulation is that it can also account for charge diffusion due to high carrier concentration gradients, space charge effects due to unbalanced mobilities and possible field-dependent mobilities. The numerical fits for P3HT:PCBM (left) and PTB7:PCBM (right) for different biases and time delays are presented in Figure 4.13. The corresponding

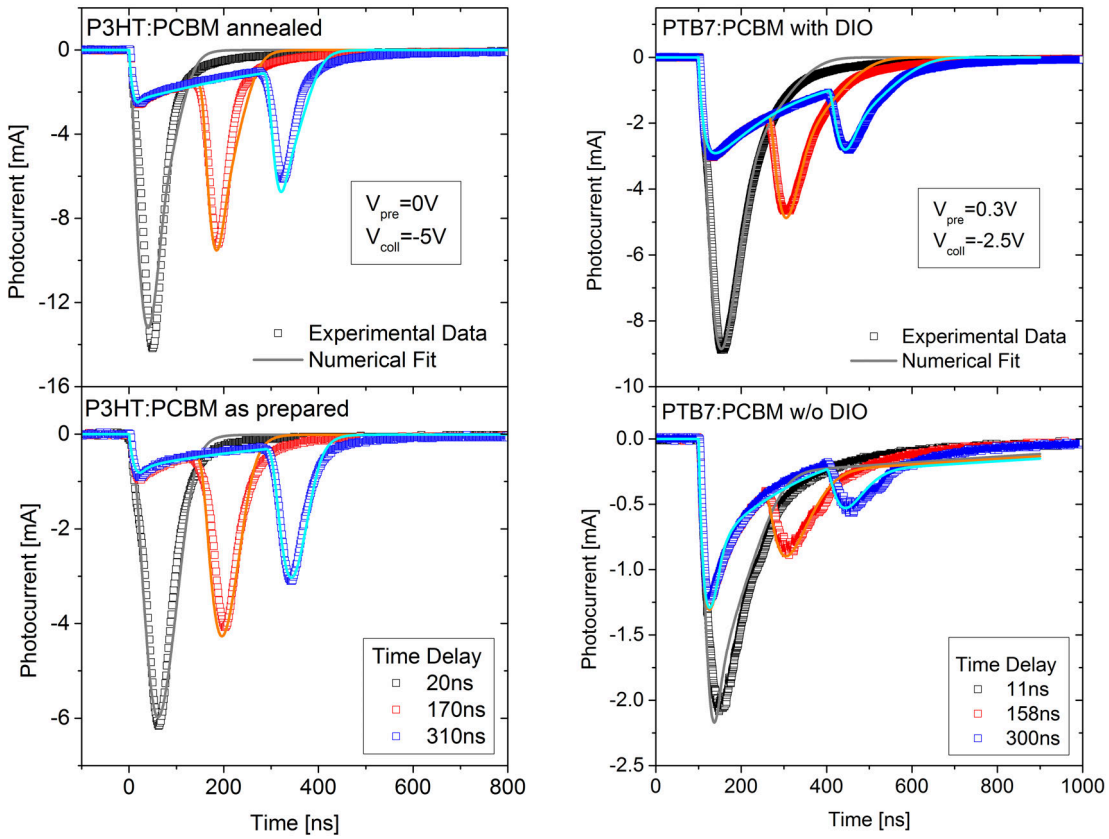

Figure 4.13: Numerical drift diffusion fits to TDCF transients under different time delays and bias conditions for P3HT:PCBM (left) and PTB7:PCBM (right) devices. Symbols are the measurement and solid lines are the simulations. The input parameters are summarized in Table 4.1. In all cases a linear voltage ramp with risetime 20 ns was used. In both P3HT:PCBM samples and the PTB7:PCBM w/o DIO a slightly higher and time dependent mobility during the first 20 ns was used.

	P3HT:PCBM		**PTB7:PCBM**	
	as prepared	**annealed**	**w/o DIO**	**with DIO**
n_0 [m^{-3}]	$3.4 \cdot 10^{-22}$	$3.1 \cdot 10^{-22}$	$2.5 \cdot 10^{-22}$	$6.5 \cdot 10^{-22}$
μ_e [cm^2/Vs]	$9 \cdot 10^{-4}$	$1.8 \cdot 10^{-3}$	$3 \cdot 10^{-5}$	$3 \cdot 10^{-4}$
μ_h [cm^2/Vs]	$1 \cdot 10^{-6}$	4×10^{-4}	$9 \cdot 10^{-4}$(*)	4.5×10^{-4}
BMR [m^3s^{-1}]	$6 \cdot 10^{-17}$	1.1×10^{-18}	$5 \cdot 10^{-17}$	$1.6 \cdot 10^{-17}$
R [Ω]	70	60	50	50
C [pF]	265	265	354	354

Table 4.1: Simulation parameters used in Figure 4.13. (*) field-dependent (zero-field) mobility with $\beta = -0.003\sqrt{\mathrm{cm/V}}$

simulation parameters are summarized in Table 4.1.
It is important to note that, given the rather large number of parameters, different sets of parameters may achieve similar good fits to the data. However, here most input parameters can be supplied by experiments. The relative permittivity (determining the sample capacitance and therefore the RC time constant) and the series resistance were taken from the dark transient analysis. The mobility of the faster charge carrier type was taken from extrapolated transit times and the initial photogenerated carrier density was taken from the photocurrent integral. The bimolecular recombination coefficients were taken from the delay dependent TDCF measurements in Section 4.3. With that the only fit parameter left is the carrier mobility of the slower carrier type and the simulation can be used to estimate that value. The mobility values of the slower carriers leading to the best fits are given in Table 4.2. For the as prepared P3HT:PCBM device the slower carrier mobility was assumed to be at least 3 orders of magnitude lower than the faster carrier mobility as has been observed in previous measurements for P3HT:PC[60]BM. As mentioned before, the contribution of the rather immobile holes to the photocurrent is below the resolution limit of the oscilloscope and could therefore not be fitted with the simulation.
The most critical point in this approach is that the exact built-in field of the sample is not known. In the simulation it is given by the difference of the electrode work functions. However, in the real device the electrodes are pinned to certain levels above the HOMO or below the LUMO.[174] The exact values of these pinning levels

	P3HT:PCBM		**PTB7:PCBM**	
	as prepared	**annealed**	**w/o DIO**	**with DIO**
faster carrier (extrapolation of extraction transients)	1×10^{-3} (electrons)	1.2×10^{-3} (electrons)	7×10^{-4} (holes)*	4.5×10^{-4} (holes)
slower carrier (fit to TDCF transients)	1×10^{-6} (holes)†	4×10^{-4} (holes)	3×10^{-5} (electrons)	3×10^{-4} (electrons)
electron-only (SCLC)	-	1.3×10^{-3} (electrons)	-	4×10^{-4} (electrons)
hole-only (SCLC)	-	1.6×10^{-4} (holes)	-	-

Table 4.2: Summary of mobilities in [cm^2/Vs] obtained from different experiments. Details of experimental and analytic techniques are given in the text. For field-dependent mobilities (*), the values at short circuit conditions are stated. †The hole mobility in as prepared P3HT:PCBM blends could not be fitted and was set to a fixed value in the simulation.

depend on carrier density and energetic disorder [175] which is not considered in this simulation. Importantly, the built-in field of a sample determines the effective electric field in the device under pre-bias and collection-bias conditions, which might therefore be slightly different in the simulation and the experiment.
Furthermore, the simulation assumes blocking contacts and does not account for high injected carrier densities, as was measured for example in annealed P3HT:PCBM, and which may alter the electric field and carrier distribution in the device. As a last point, the simulation does not account for a distribution of carrier mobilities known as dispersion, which has been observed [16] and leads to a broadening of the transients at longer extraction times.
Nevertheless, the good agreement between the fits and the experimental data gives a good estimate of the charge carrier extraction kinetics and the extracted mobilities present a profound basis to compare them to alternative mobility measurements. In any case, complementary measurements have to be used to distinguish between electron and hole mobilities.
A standard approach to separately investigate electron and hole transport is the measurement of space charge limited current (SCLC) in single carrier devices (see Section 2.5.3). These unipolar current measurements analyse the flow of charges injected via ohmic contacts at forward bias in the dark. In the absence of traps, the space charge limited current is described by the Mott-Gurney law:

$$J_{\mathrm{SCLC}} = \frac{9}{8}\mu\varepsilon\varepsilon_{\mathrm{r}}\frac{V^2}{d^3}, \tag{4.8}$$

and depends on the applied voltage V, the film thickness d and the mobility μ. Hole-only and electron-only devices were prepared as described in the appendix A.2. The resulting current density versus voltage curves for P3HT:PCBM (200 nm) at different annealing temperatures are shown in Figure 4.14. The hole-only devices approach a quadratic dependence of the current on the bias for high voltages and annealing temperatures above $60°C$. A fit to the curve at $140°C$ with Equation (4.8) (red dashed line) reveals a hole mobility of $\mu = 1.6 \times 10^{-4}$ cm^2/Vs. The as prepared hole-only device exhibits a slope in the log-log plot of slightly higher than 5. A slope larger than two is often connected to trap-limited current [100], but could also stem from a field-dependent mobility [102]. From the current-voltage characteristics alone, these two processes cannot be distinguished and a definite determination of the mobility is not possible. However, the comparison of the current density at 4V reveals qualitatively a continuous increase of the mobility with increasing annealing temperature over three orders of magnitude.
The electron current at the same bias increases only by about one order of magnitude with annealing temperature. The $J - V$ characteristics exhibit a slope of two for annealing temperatures of $60°C$ and higher. A fit to the curve at $140°C$ gives a mobility of $\mu = 1.3 \times 10^{-3}$ cm^2/Vs. This is in very good agreement to the value gained from the TDCF transients. From this it can be concluded that the faster charge carriers in the annealed devices are the electrons and the initial decay of the TDCF transients is caused by the electron motion across the device.
The slope of the $J - V$ curve of the as prepared electron-only device is slightly

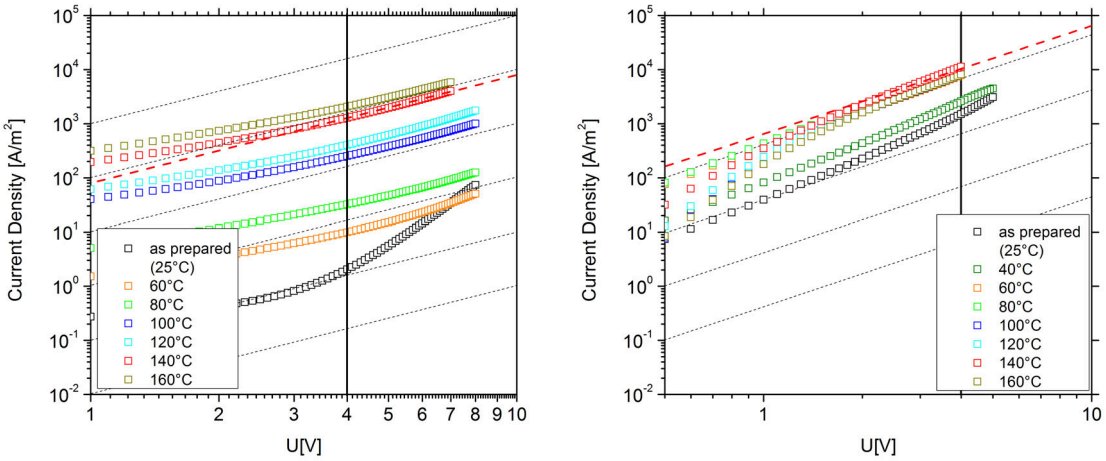

Figure 4.14: Dark current density versus voltage data of hole-only (left) and electron-only (right) P3HT:PCBM devices at different annealing temperatures. The dashed lines are fits to the curves at 140°C with Equation (4.8). The thin dotted lines indicate a slope of 2 in the log-log plot.

higher than two and can therefore not be evaluated with Equation (4.8). However, the current density at 4 V is about three orders of magnitude higher in the electron-only device compared to the hole-only device. Therefore, it is safe to conclude that the faster charge carriers in the as-prepared devices are also the electrons. Furthermore, a vast difference in the electron and hole current densities, and therefore also mobilities, in these devices becomes visible. As a result, the charge transport in as prepared P3HT:PCBM solar cells is strongly imbalanced and the build-up of space charge is expected to lead to a depression of the photocurrent and the fill factor.
The results of the SCLC measurements compare well to the work done by Mihailetchi et al. and Turner et al. on P3HT:PC[60]BM.[25, 118] In these studies the low hole mobilities were attributed to small P3HT aggregates and a lower overall crystallinity in the unoptimized devices. While the crystallinity in pristine P3HT films is quite high [113], the presence of PCBM molecules seems to prevent immediate crystalliziation of P3HT after the spin-coating process, resulting in a more amorphous film. This leads to weak interchain interaction in P3HT which strongly supresses the hole mobility. Upon thermal annealing, slow crystalliziation of P3HT takes place and a demixing between P3HT and PCBM is observed [114] which leads to improved charge transport. Note, that the previous work studied P3HT mixed with PC[60]BM. Here a very similar scenario is confirmed when using PC[70]BM.

Single carrier devices have also been prepared from PTB7:PCBM blends with and without DIO to measure electron and hole transport independently. The electron current density is shown to be space charge limited in both devices (see appendix A.5) and the results for two different film thicknesses are plotted in Figure 4.15 (symbols). For a constant voltage (e.g. 2 V) the electron only current density is about one order of magnitude lower in the devices without DIO. Since, in the case

of SCLC, the current density is directly proportional to the charge carrier mobility, two important conclusions can be drawn. First, upon addition of DIO the electron mobility significantly increases by about one order of magnitude. However, the mobilities determined from the TDCF transients show a slight decrease with DIO. Therefore, the faster charge carrier type, measured with TDCF can be assigned to holes. Then, the electron mobility in the devices without DIO is about one order of magnitude lower than the hole mobility, and this is expected to lead to severe extraction problems at low biases and therefore limit the FF.
For the devices with DIO, the $J - V$ characteristics reveal a slope of 2 in the investigated voltage range and can be evaluated with Equation (4.8). The mobilities obtained from the fit (lines in Figure 4.15) are stated in the graph and agree very well to the value determined for the slower charge carriers from the numerical fits to the TDCF transients (compare Table 4.2). For the devices without DIO, the slope in the log-log plot is higher than two, possibly due to a field-dependent or trap-limited mobility. At first glance, the low electron mobility in the presence of large pure fullerene domains in the blend without DIO as was observed by Collins et al. seems counterintuitive. However, a recent study by Hedley et al. showed that the large fullerene domains in the device without DIO (of 100-200 nm in diameter) consist of smaller 20-60 nm very pure fullerene spheres.[124] While the electron mobility within those small fullerene spheres might be quite high, the macroscopic transport across the entire fullerene domain will limited by the transitions between the small spheres.
These findings are in part in variance with the results from a recent mobility study by Foster et al. on blends of PTB7 with PC[60]BM.[28] While both studies agree that DIO has little effect on the hole mobility, the absolute values of electron and

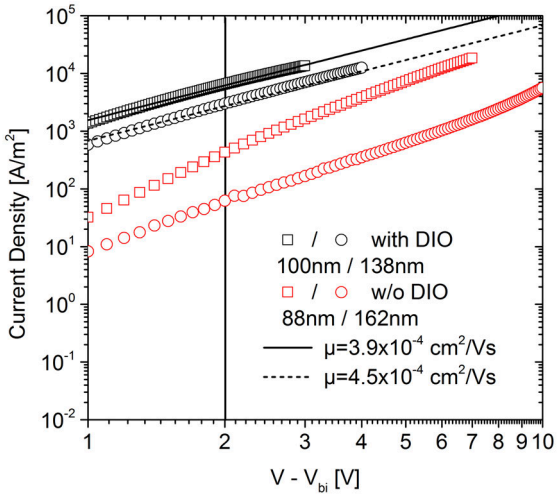

Figure 4.15: Dark current density versus voltage data of electron-only devices prepared with (black) and without DIO (red) for 2 different layer thicknesses each. The lines are best the fits with Equation (4.8). The obtained mobilities are displayed in the graph.

hole mobilities are found to be much lower in this report. More importantly, Foster et al. found the electron mobility to significantly decrease further with the use of DIO, despite a larger fill factor of the DIO processed device. Such low mobilities would significantly depress the fill factor and are therefore in contradiction to the high FF measured in devices with DIO. Compared to blends with PC[70]BM, the devices in this report yielded a smaller FF, indicating that differences in the charge carrier dynamics cannot be ruled out. Recently, evidence of a different film morphology in blends made of PTB7 with PC[60]BM as compared to PC[70]BM has been reported.[155] Concomitant differences in the charge transport properties might be the reason for the different mobilities.
Note, that hole-only devices have also been prepared with and w/o DIO. However, for unknown reasons, the $J-V$ curves for all thicknesses up to 200 nm displayed a slope of 1 and could not be evaluated with SCLC.

In summary it has been shown that the charge transport properties of BHJ solar cells are largely affected by the sample preparation conditions. TDCF analysis in combination with SCLC measurements revealed that thermal annealing of chloroform cast P3HT:PCBM blends increases the hole mobility by three orders of magntitudes and the electron mobility by about one order of magnitude. In high efficiency PTB7:PCBM blends the effect of DIO is mainly to increase the electron mobility. While in the respective optimized devices, balanced charge transport allows for efficient extraction of both electrons and holes also at low internal fields, the unoptimized devices are strongly transport limited. In PTB7:PCBM without DIO a difference of electron and hole mobility of approximately one order of magnitude hinders extraction mainly at low internal fields while higher fields facilitate transport of both carriers. In contrast, in as prepared P3HT:PCBM blends a mobility mismatch of several orders of magnitude leads to a build up of space charge and limits extraction over a wide voltage range.

4.5 Summary

In this chapter the charge carrier generation, recombination and transport of two highly relevant OPV material systems - P3HT:PCBM and PTB7:PCBM - have been studied in great detail. Both systems have in common that they exhibit only moderate to poor performances directly after preparation and require special treatment such as thermal annealing or the addition of a solvent additive to reach their maximum performances. The influence of the preparation conditions on the charge carrier dynamics was to be explored.
The implementation of a new TDCF set-up with very high time resolution now allows to determine the field dependence of charge carrier generation and geminate recombination losses very precisely within a few percent. It turned out that in three of the four investigated samples the free carrier generation process does not depend on the electric field. The blends of P3HT:PCBM consist of an interpenetrating network of highly crystalline nanometer-sized polymer and fullerene domains.[114, 116, 117]

Even in the as prepared blend about 30% of the P3HT chains have been found in an aggregated state.[118] It is proposed that these crystalline domains stabilize the separated charges away from the interface and therefore prevent them from geminate recombination. In the blend of PTB7:PCBM with DIO the nanometer-sized aggregated pure fullerene domains [123, 124] are responsible for stabilization of the charges and suppression of geminate recombination. In contrast, in the PTB7:PCBM blends without DIO, large more than 100 nm sized, mixed phases with dispersed PCBM lead to a field dependent generation with geminate recombination losses at low internal fields of about 20%. These results prove that the generation process is not primarily responsible for the performance improvement in these devices.
In fact, the poor FF in both unoptimized blends is mainly caused by unbalanced mobilities, which however have different origins in the different blends. In the as prepared P3HT:PCBM the very fine intermixing of polymer and fullerene phases and the lower content of crystallized polymer chains lead to poor percolation for hole transport. In contrast, PTB7:PCBM w/o DIO consists of very large polymer-rich domains which leads to a higher hole mobility compared to the unoptimized P3HT:PCBM device. However, electron transport in these blends is most probably limited by transitions between small pure fullerene spheres within the fullerene-rich domains which are separated by amorphous mixed regions.[124]
In both systems optimization via annealing or solvent additive improves electron and hole transport and leads to more balanced mobilities, which are $\mu_e = 1.2 \times 10^{-3}$ cm^2/Vs and $\mu_h = 4 \times 10^{-4}$ cm^2/Vs for annealed P3HT:PCBM and $\mu_e = 3 \times 10^{-4}$ cm^2/Vs and $\mu_h = 4.5 \times 10^{-4}$ cm^2/Vs for PTB7:PCBM with DIO. In the optimized PTB7:PCBM the mobilities are even more balanced (ratio of 1.5) compared to P3HT:PCBM (ratio of 3) leading to a slightly higher FF in these devices, even though the BMR coefficient was significantly higher ($k = 1.6 \times 10^{-17}$ m^{3}s^{-1} in PTB7:PCBM and $k = 1.2 \times 10^{-18}$ m^{3}s^{-1} in P3HT:PCBM). It should be noted that balanced mobilities alone are not sufficient to reach high FF. Both mobilities have to be sufficiently high so that the charge carriers are extracted from the layer fast enough before undergoing BMR. Also, the layer thickness plays an important role. Since the PTB7:PCBM blends have only half the layer thickness, the dwell time of the carriers in the layer is shorter compared to the thicker P3HT:PCBM blends and the higher BMR coefficient is less disruptive.
In both optimized devices the nongeminate recombination is reduced compared to Langevin recombination described in Chapter 2.4.2. The reasons for the reduction lie in the optimized phase separated blend morphology, however they are not understood in detail yet and could not be further elucidated in this work.
Whether the measured parameters for the generation rates, mobilities and recombination coefficients are able to explain the exact shape of the $J - V$ curves (Figure 2.12 and 2.14) will be further investigated with the help numerical device simulations in Chapter 6.

5 Steady State Recombination

5.1 Introduction

In the previous chapter it has been shown that beside charge carrier generation and extraction, the recombination process of independent charge carriers plays a major role in the determination of the device efficiency. So far, recombination has been studied with TDCF, where the device equilibrium state is disturbed by illumination with a short laser pulse. Naturally, the boundary conditions in this experiment are different from the device steady state conditions under continuous illumination.
For example, in case of energetic disorder, the Gaussian disorder model (GDM) [16] as well as the multiple trapping (MT) and release model [96, 176, 177] predict a time-dependent relaxation of charge carrier mobility after pulsed generation in a transient photocurrent experiment. Hence, the mobility and with that the recombination rate constant directly after laser excitation might potentially be higher compared to the steady state situation.
Another difference is expected to occur in the distribution of the charge carriers across the device. While a homogeneous carrier profile is assumed after laser excitation, in some cases very inhomogeneous profiles have been reported for continuous illumination [90] which will certainly influence the carrier dynamics.
Therefore, it is of great interest to investigate the recombination behaviour under steady state conditions and compare it with the results of the transient experiments.
In a solar cell under illumination at open circuit conditions the external current is zero by definition. In good approximation the net current density at each point in the bulk is also zero and the continuity equation is reduced to $G = R$ with G being the generation rate and R being the recombination rate. In case of bimolecular recombination this expression can be written as:

$$G = R = kn^2, \tag{5.1}$$

where n is the charge carrier density and k is the bimolecular recombination coefficient. If G and n are known, the recombination coefficient can be calculated. The generation rate can be determined from the current density at high reverse bias via $G = J_{rev}/ed$, where geminate and nongeminate recombination losses are assumed to be absent and all generated charge carriers are extracted. The only unknown parameter is then the charge carrier density present in the device and shall be more closely investigated in this chapter. It is shown that current methods to determine carrier densities are insufficient for the investigated material systems and a new experimental set-up to measure charge carrier densities is developed. The analysis of carrier density at different illumination intensities as a function of the generation rate reveals the recombination coefficient as a function of carrier density and yields information of the reaction order and energetic structure of the blends. Furthermore, the physical meaning of the extracted carrier densities and the influence of illumination and device thickness on the calculated recombination coefficients will be investigated by means of numerical simulations.

5.2 BACE - Bias Assisted Charge Extraction

At the beginning of this work, the most established method to measure charge carrier densities in solar cells under steady state operating conditions was the *Charge Extraction* (CE) method.[170] In this conventional CE experiment, the device is illuminated by white light-emitting diodes and held at open-circuit conditions. The light source is then switched off and at the same time, the device is short circuited. This creates a current transient as the cell discharges, which is integrated to obtain the charge carrier density.

This method proved to work well for high efficiency solar cells where a sufficient extraction of all charge carriers in the device is expected, even at low electric fields (short circuit). However, problems might occur if strong recombination or space charge effects hinder the extraction of all charge carriers under short circuit conditions as was seen for example for the as prepared P3HT:PCBM device and also for blends of some new low bandgap polymers, including PTB7, with PCBM. Furthermore, trapping of charge carriers in deep trap states might also prevent a complete extraction of charge carriers.

For those reasons, the novel technique of *Bias Assisted Charge Extraction* (BACE) was developed within this work as a more general approach to measure charge carrier densities. The goal of this technique is to considerably accelerate the extraction of the charge carriers by applying a high extraction voltage V_{extr} in reverse direction. The experimental set-up and the schematic time line of the experiment are presented in Figure 5.1. Here, during steady state illumination the device is held at a fixed prebias $V_{\mathrm{pre}}(I)$ that corresponds exactly to the open circuit voltage $V_{\mathrm{OC}}(I)$ at the given illumination intensity I. The respective values for $V_{\mathrm{OC}}(I)$ are independently measured across a 10 MΩ resistor prior to the BACE measurement. When switching off the LEDs, the external bias is rapidly changed to reverse direction (rise time of voltage pulse ≈ 20 ns). By applying sufficiently high extraction voltages, the extraction time can be pushed to the limit of the RC time and losses due to recombination and trapping are reduced. Integration of the current transient then yields the total mobile charge, assuming a homogeneous distribution is present in

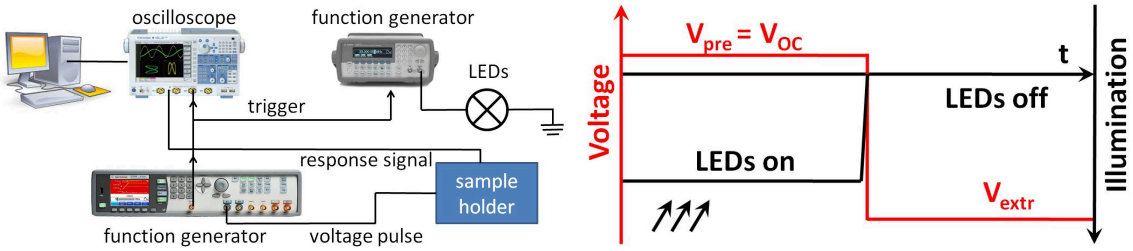

Figure 5.1: Experimental setup and schematic time line of the BACE experiment. An Agilent 33220A function generator was used to operate the LEDs and an Agilent 81150A was used to switch the bias voltage between V_{pre} and V_{extr} and provide the trigger for the whole setup. Illumination was provided by an array of four focused white light LEDs (Lumileds Rebel, switch-off time < 200 ns).

the device.
Proper care of the capacitive charge is taken by performing the same voltage jump in the dark and setting V_{pre} to 0 V. It is important to start the reference measurement at 0 V (or even below), to avoid subtraction of potential dark charge due to injection, which would lead to an erroneous determination of the total carrier density.
The advantage of the novel BACE technique is demonstrated in Figure 5.2 for the as prepared P3HT:PCBM solar cell (thickness 200 nm). The photocurrent transients (left graph) show a significantly faster extraction at $V_{\mathrm{extr}} = -4.5$ V compared to $V_{\mathrm{extr}} = 0$ V (corresponding to short circuit conditions). The right graph shows the subsequent increase of the extracted charge with increasing extraction voltage (following steady state illumination corresponding to 1 sun illumination). For voltages below -2 V the extracted charge saturates, indicating that at these conditions significant losses due to recombination and trapping can be excluded. In contrast, only about 60% of the mobile charge is extracted when the extraction bias is set to 0 V (see inset of right figure). In this case the conventional CE experiment would clearly underestimate the charge in the device.
For comparison, in the optimized annealed P3HT:PCBM device (see inset) the extracted charge does not change with applied bias, meaning that even 0 V extraction voltage (short circuit) is sufficient to remove all charge carriers from the device. This is in accordance with our findings in Chapter 4.3 and the results by Shuttle et al.[170]
Note, that the switch-off time (time until $I < 10\%$ of initial value) of the LEDs in this setup was approximately 200 ns. To avoid recombination losses during this time

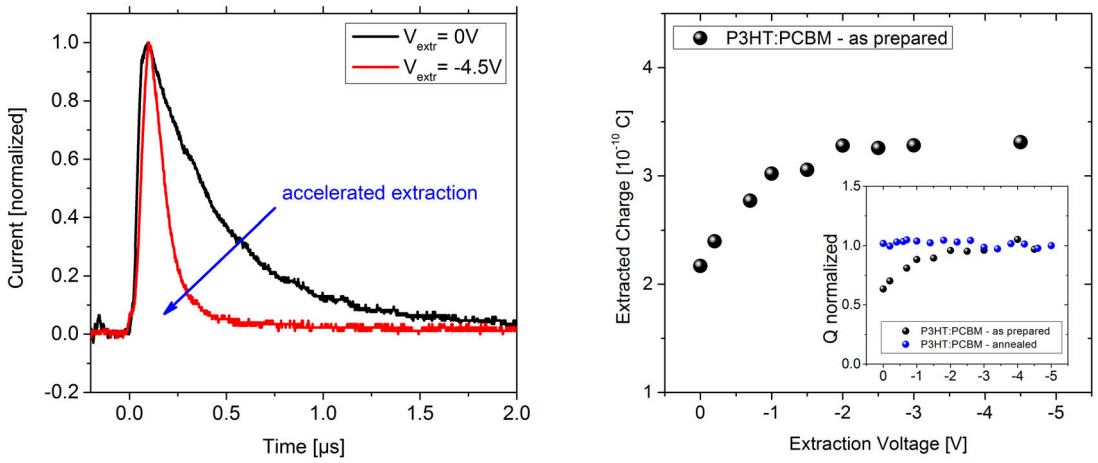

Figure 5.2: Left: Normalized BACE photocurrent transients of an as prepared P3HT:PCBM solar cell at two different extraction voltages. Right: Extracted charge as a function of applied extraction voltage. At voltages < -2 V all mobile charge carriers are efficiently extracted. Inset: Normalized extracted charge vs extraction voltage. At 0 V only 60% of the mobile charges are extracted. For comparison, in annealed P3HT:PCBM all charge carriers are extracted even at 0 V. The device thickness was 200 nm in both cases.

period, extraction was started immediately after the switch. Theoretical estimation and experimental verification (shown in the appendix A.6) revealed that only an insignificant amount of charge carriers are generated by the remaining light during the switch-off time.
In conclusion, the new BACE method enables a more accurate determination of the charge carrier density also in non-optimized devices with low mobilities or material blends with high non-geminate recombination coefficients, such as some new high-efficiency low bandgap copolymers.[144]

5.3 Steady State Carrier Densities

Before turning to the calculation of recombination coefficients, the phrase *steady state carrier density* and its physical meaning with respect to a charge extraction experiment shall be further investigated. Kirchartz and coworkers pointed out that charge carrier profiles are highly inhomogenous, in particular for thin devices and low illumination intensities. As a result, reaction orders deduced from CE experiments might be incorrect.[90] The following sections consider this for BACE and for parameters relevant for the experiments conducted here. Figure 5.3 (left) shows simulated carrier density profiles at open circuit conditions for typical device parameters of a PTB7:PCBM blend with DIO. The device thickness was chosen to be 100 nm, the injection barrier $\phi_B = 0.05$ eV and generation rate $G = 1.1 \times 10^{28}$ m^{-3}s^{-1}. All other parameters were taken from Table 6.3. The spatial distribution of the charge carriers was calculated with the drift diffusion simulation described in Section 2.7.1. As can be seen from Figure 5.3 the carrier density extends over more than 5 orders

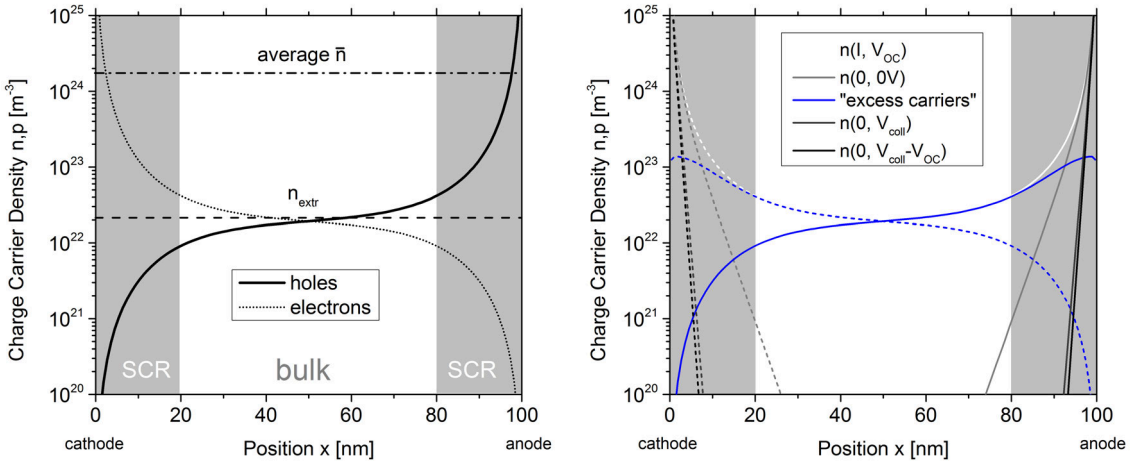

Figure 5.3: Left: Simulated charge carrier density profiles for a 100 nm device under illumination at V_{OC} with injection barriers of 0.05 eV and a generation rate of 1.1×10^{28} m^{-3}s^{-1}. The dashed-dotted line indicates the average carrier density in the device and the dashed line denotes n_{extr} according to Equation (5.5). Under reverse bias, electrons move to x=0 and holes to x=d. Right: Density profiles in the dark at different biases and excess carrier density as described in the text.

of magnitude through the device with steep gradients close the contacts. This raises the question about the relevant carrier density in the device.
As indicated in the graph, the device can be divided into three regions. The space charge regions (SCR) close to the contacts (marked by the grey areas in the graph) are determined by the injection of charge carriers and characterized by very steep gradients of the carrier density. The bulk region in the middle of the device (white area in graph) exhibits less steep gradients and is mainly determined by photogeneration and recombination of charge carriers in the bulk. The average carrier density defined as $\bar{n} = \frac{1}{d}\int n(x)dx$ (marked by the dashed-dotted line in Figure 5.3) is strongly determined by the space charge regions and is several orders of magnitude higher than the carrier density in the bulk.
The steady state carrier distribution strongly depends on the chosen experimental parameters. Figure 5.4 (upper panel) shows the simulated density profiles for different injection barriers (a) and layer thicknesses in the dark (b) and for different illumination intensities, expressed by the varying generation rate (c). For decreasing injection barriers, $\phi_B \rightarrow 0$, the injected carrier density at the contacts strongly increases and dominates the carrier distribution in the layer. Only for barriers above 0.2 eV a more homogeneous bulk region is established. Note that in this

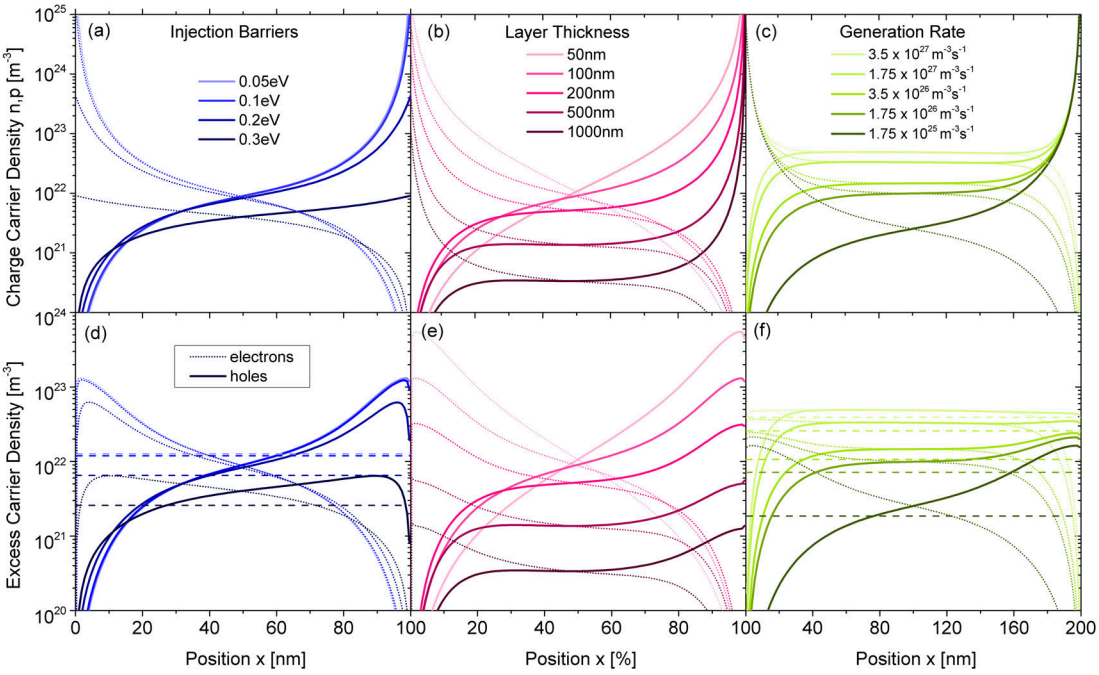

Figure 5.4: Upper Panel: Simulated charge carrier density profiles for (a) different injection barriers for a 100 nm device in the dark at 0.7 V; (b) different layer thicknesses for a barrier of 0.05 eV in the dark at 0.7 V; (c) different illumination intensities at respective V_{OC} expressed by the generation rates for a 200 nm device with 0.05 eV barrier. Lower Panel: Excess carrier densities for the same conditions. The dashed lines denote n_{extr}.

simulation the injection of charge carriers is treated by thermal equlibrium at the metal-semiconductor interface. Therefore, the charge carrier density in the first simulation cell of the active layer is kept constant at $n = N_c \exp(-\phi_B/kT)$, where N_c is the effective density of states of the conduction and valence bands and ϕ_B is the injection barrier (see Section 2.7.1 for a more detailed description of the simulation). The distribution of charge carriers without illumination is then given by drift and diffusion of injected carriers being in equilibrium with recombination of electrons and holes in the bulk. In the case of low injection barriers, the homogeneous bulk region is more distinct for larger layer thicknesses, where the extension of the space charge regions becomes small compared to the layer thickness. For layer thicknesses below 100 nm the carrier distribution in the dark is completely injection dominated and no bulk region is established. Figure 5.4 (c) shows that under illumination with increasing generation rate the carrier distribution becomes more homogeneous and the bulk region becomes more distinct compared to the contact regions. Note that the bulk carrier density established as a plateau (n_{bulk}) is the relevant carrier density that reveals information about the recombination dynamics in the blend. According to Equation (5.1) the $n_{\mathrm{bulk}}(G)$ - dependence is determined by the recombination order, which is two in the simulations. Figure 5.5 (left) displays the simulated n_{bulk} (taken from the plateau for high generation rates) as a function of generation rate, corresponding to the density profiles shown in Figure 5.4 (c). As expected for bimolecular recombination, the slope of the log-log plot is 1/2. Note that the density profiles were simulated at the open circuit voltage, corresponding to the respective generation rate, exactly as in the real BACE measurement. The values for V_{OC}

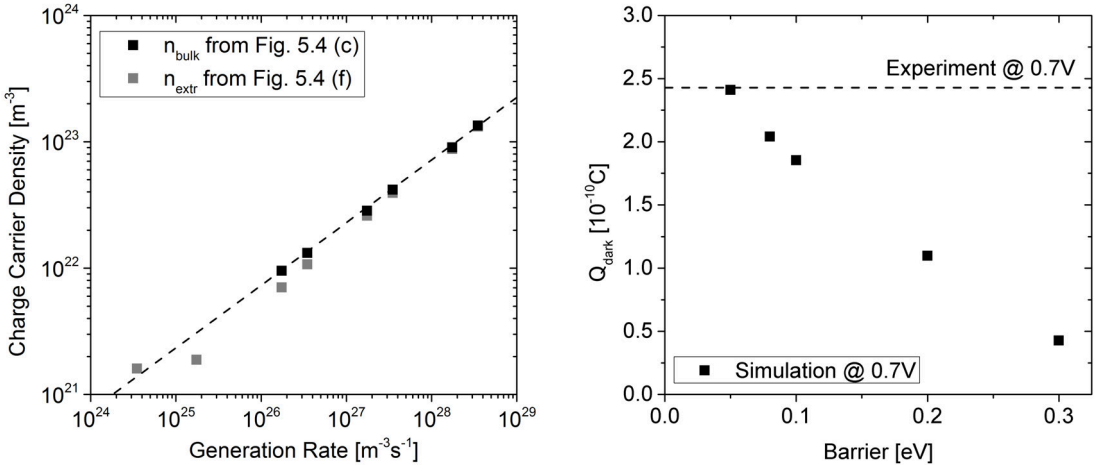

Figure 5.5: Left: Simulated n_{bulk} and n_{extr} for different generation rates taken from the density profiles shown in Figure 5.4 (c,f). For $G < 10^{26}$ m^{-3}s^{-1}, n_{bulk} is not shown as no plateau is established. The dashed line indicates a slope of 1/2. Right: Simulated dark charge as a function of the injection barrier for a 100 nm device at 0.7 V. The parameter set for the PTB7:PCBM device with DIO (Table 6.3) was used. The dashed line corresponds to the measured value of Q_{dark} for PTB7:PCBM at 0.7 V.

at the respective generation rates were taken from the $J-V$ curves, which were simulated in advance.
As mentioned before the BACE measurement always includes the correction by a dark reference pulse to negate the capacitance effects. Therefore, altogether four different carrier profiles are important that are indicated in Figure 5.3 (right). Besides the carrier distribution under illumination at V_{OC}, $n(I, V_{\mathrm{OC}})$, also the carrier profiles in the dark at V_{coll} (extraction after illumination), 0V and $V_{\mathrm{coll}} - V_{\mathrm{OC}}$ (reference pulse) have to be considered. The carrier distribution that is actually probed in a BACE measurement is then:

$$n_{\mathrm{excess}} = [n(I, V_{\mathrm{OC}}) - n(0, V_{\mathrm{coll}})] - [n(0,0) - n(0, V_{\mathrm{coll}} - V_{\mathrm{OC}})], \tag{5.2}$$

which is called the excess carrier density. In general, $n(0, V_{\mathrm{coll}}) \approx n(0, V_{\mathrm{coll}} - V_{\mathrm{OC}})$ (compare Figure 5.3 (right)) and with that n_{excess} can be simplified to $n_{\mathrm{exc}} \approx n(I, V_{\mathrm{OC}}) - n(0,0)$.
The excess carrier density is plotted in Figure 5.4 lower panel. It is obvious that $n_{\mathrm{exc}}(x)$ is in general more homogeneous compared with the upper panel since the injected carrier density at the contacts hardly changes when going to 0V in the dark. This also indicates that the large carrier densities at the contacts cannot be extracted in the measurement.
In a charge extraction experiment, BACE as well as conventional CE, the carrier density is determined from the integral of the extraction current transient over time. This integral is determined by the average (excess) carrier density and the average distance traveled by each carrier. In the case of an inhomogeneous spatial distribution, the drift length of the charge carriers has to be weighted by the charge carrier density according to:

$$\bar{x} = \frac{\int_0^d x \cdot n_{\mathrm{exc}}(x) dx}{\int_0^d n_{\mathrm{exc}}(x) dx}, \tag{5.3}$$

where $\bar{x}$ is the weighted drift length, x is the position in the device and $n(x)$ is the carrier density as a function of position. The extracted charge Q_{extr}, that corresponds to the integral of the transient, can then be calculated by:

$$Q_{\mathrm{extr}} = \bar{n}_{\mathrm{exc}} e A \bar{x}, \tag{5.4}$$

with e the electric charge and A the electrode area. Note, that Equation (5.4) is valid if charges are extracted at $x = 0$ (electrons). For charges that are extracted at $x = d$ (holes), $Q_{extr} = \bar{n} e A (d - \bar{x})$ has to be used instead. A confirmation by transient simulation that the integral of a current transient arising from a certain carrier distribution $n(x)$ indeed corresponds to the value calculated by Equations (5.3) and (5.4) can be found in the appendix A.7. From the integrated charge, the extracted charge carrier density is determined by:

$$n_{\mathrm{extr}} = \frac{Q_{\mathrm{extr}}}{eAd}, \tag{5.5}$$

as is also done in extraction experiments. n_{extr} is plotted in Figure 5.4 (c) (dashed lines). It is clear that n_{extr} is in general lower than n_{bulk} due to the dark correction.

Only for very high generation rates (illumination intensities) n_{extr} is expected to approach n_{bulk}. In the plot n_{extr} vs. G (Figure 5.5) this leads to a slightly larger slope than 1/2 for intermediate generation rates. As a consequence, BMR coefficients determined from n_{extr} in this regime would be overestimated. It can be concluded that higher illumination intensities lead to more reliable results, since the dark charge becomes less important.
Notably, for very low generation rates, n_{extr} levels off at a slope <1/2 which has often been obeserved in experiments. The reason for this deviation is that the carrier distributions become very inhomogeneous at low illumination and the space charge regions at the contacts begin to dominate the integral. As a consequence, n_{extr} is not related to the bulk carrier density anymore and hardly depends on the illumination intensity, which in turn leads to an apparent recombination order higher than 2.
The influence of spatial gradients of charge density on the apparent reaction order was already pointed out by Deledalle et al.[90] In this publication the reaction order was determined from the ideality factor and the voltage dependence of the charge carrier density. However, this work did not explicitly investigate the influence of the spatial gradient on the integral of an extraction transient as was done here.

Interestingly, from Figure 5.4 (a,d) it became clear, that the height of the injection barrier ϕ_B strongly influences the carrier density in the dark. In reverse, the dark charge measured in the device under forward bias can now be used to estimate the injection barriers. As an example the measured dark charge in the PTB7:PCBM device with DIO at 0.7 V was $Q_{\mathrm{dark}} = 2.43 \times 10^{-10}$ C (see Chapter 4.3). In Figure 5.5 (right) this value is compared to the simulated Q_{dark} for PTB7:PCBM with DIO (parameters from Table 6.3) at 0.7 V for different barrier heights. With decreasing barrier, the extracted dark charge rapidly increases. The experimental value (dashed line) is only reached for the lowest barrier considered here (0.05 eV), suggesting that rather low injection barriers are a realistic assumption. This is in accordance with recent findings in literature, that optimized, ohmic contacts facilitate injection and increase device efficiencies.[30, 178]

In conclusion, the theoretical investigations show that the charge carrier density measured with BACE can in principle be used to determine the recombination order and rate coefficients for different steady state illumination intensities. However, the simulations revealed clear limits for the experiment and the conditions have to be chosen such that n_{extr} is close to n_{bulk}. For very inhomogeneous carrier profiles, i.e. for low injection barriers, low illumination and layer thicknesses below 100 nm, no real bulk density plateau is established. In this case n_{extr} has no physical meaning. This has to be considered when setting up a charge extraction experiment. In the light of the thereby arising experimental requirements (high carrier densities, large layer thicknesses), the necessity of an external bias to extract all charge carriers and the superiority of BACE compared to conventional CE, becomes even more significant.
Furthermore, the corrections by the dark reference pulse lead to an error, if Q_{dark} at

0V is still considerable high (i.e. at low injection barriers). Therefore, the error made in the experiment depends sensitively on the barriers, thickness and illumination intensity and special care has to be taken when analysing charge carrier densities as deficient experimental conditions can easily lead to erroneous conclusions.

5.4 Steady State Recombination Coefficients

Having clarified the physical meaning of the extracted charge carrier density and the conditions for which reliable results can be obtained, we will now turn to the determination of the steady state recombination coefficients. It has been shown, that the slope of the log-log plot carrier density versus generation rate gives the recombination order, which is 2 in case of bimolecular recombination (BMR). Using Equation (5.1) the BMR recombination coefficients under steady state conditions can be determined. The experimental results for the four investigated devices, P3HT:PCBM annealed and as prepared as well as PTB7:PCBM with and without DIO, will be discussed with respect to the results from TDCF measurements and from literature.

5.4.1 P3HT:PCBM

Figure 5.6 (left) shows the total extracted charge carrier density measured with BACE for the as prepared and annealed device as a function of illumination intensity. The extraction bias was set to -5 V to ensure sufficient extraction of all charge carriers also for the highest light intensities. For all light intensities, the steady state carrier density in the annealed device is about one order of magnitude higher than in the as prepared device. This is in agreement with the results of Hamilton et al. where the charge carrier density was determined using a differential capacitance technique.[159] The lower charge carrier density in the as prepared device is mainly attributed to a higher recombination rate in accordance with the results from TDCF.
For the illumination range studied here, non-linear processes like exciton-exciton annihilation can assumed to be absent and the charge carrier generation rate is strictly proportional to the illumination intensity. In this case Figure 5.6 is analogous to the left plot in Figure 5.5. The slope of the extracted charge as a function of intensity in the log-log plot is close to 1/2 in both devices. This means that non-geminate recombination strictly follows a second order process, in accordance with the good fit of the Q_{coll} versus delay time data (see Chapter 4.3) to a bimolecular recombination process.
The charge carrier generation rate was calculated from the steady state current density of the annealed device at -2 V. Motivated by the results from Chapter 4.2, the same generation rates at the respective illumination intensities were assumed for the annealed and as prepared devices and the charge in the as prepared device under illumination was assumed to be double the extracted charge.
The calculated BMR coefficients k for both devices are shown in Figure 5.6 (right) in comparison with the coefficients determined with TDCF. Both techniques yield very similar values for the BMR coefficient. This suggests that carriers generated

by pulsed illumination in the TDCF experiments equilibrate rapidly and that the equilibrated carrier distribution is similar to the steady state distribution under continuous illumination.
For the annealed blend, k is rather constant throughout the measured range of carrier densities, although a weak, approximately twofold, increase is observed when increasing the carrier density to 2×10^{23} m^{-3}. This very weak dependence of k on n is at variance previous publications, where a steeper rise of the recombination coefficient with carrier density was reported.[159, 168, 179] The reason for this discrepancy might lie in the particular preparation conditions used here. In fact, a considerable variation in the dependence of k on n in different publications becomes obvious, as illustrated by the solid lines in Figure 5.6 (right). Also, in contrast to conventional CE as well as the differential charging method, both TDCF and BACE extract charge with a reverse bias, ensuring that most mobile carriers in the device are removed from the active layer. An incomplete extraction of carriers at increasing intensities would result in a slope $< 1/2$ in the n vs G plot and consequently lead to a steeper $n(k)$-dependence.
The result of a rather constant k is in agreement with a weak dependence of carrier mobility on carrier density in this blend found in various studies.[93, 168] In Langevin theory, the BMR coefficient of a homogeneous medium is determined by the sum of the hole and the electron mobilities (Section 2.4.2). Little data is available regarding the dependence of electron mobility on electron densities in fullerenes at low fields, but due to the low disorder in the PCBM phase, the electron mobility is expected to depend only weakly on carrier density. For hole motion in pure P3HT, Tanase et al. showed that the mobility is rather constant up to a hole density of

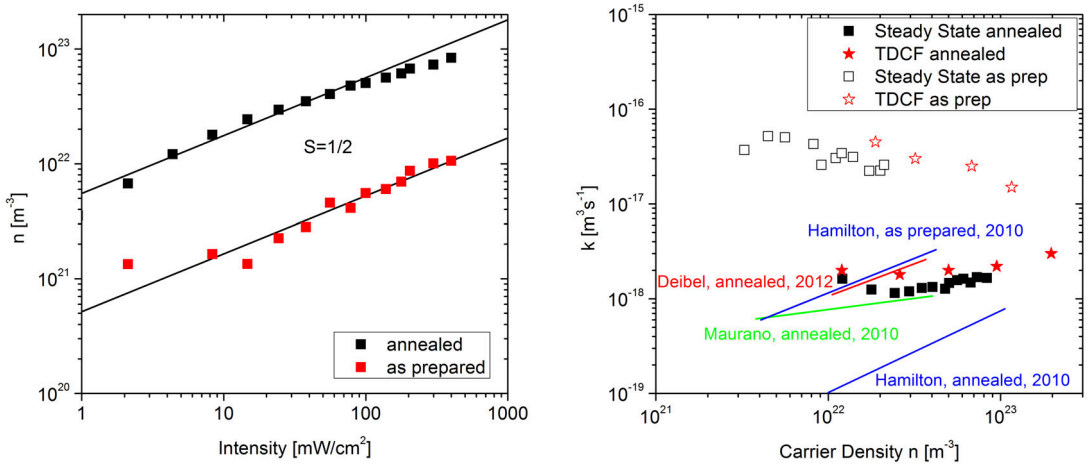

Figure 5.6: Left: Total carrier density as a function of illumination intensity for an as prepared and annealed P3HT:PCBM device. The extraction voltage was -5 V. The solid lines show a slope of 1/2. Right: BMR coefficients as a function of charge carrier density. Symbols: measurements from this work; Solid lines: trends reported in the literature.[159, 167, 168]

$\approx 7 \times 10^{22}$ m^{-3}.[92] Based on calculations with the variable range hopping model proposed by Vissenberg and Matters, the continuous increase of μ_h above a carrier density of $\approx 1 \times 10^{23}$ m^{-3} is explained by a filling of states at the bottom of the density of states (DOS) distribution.[180] Brondijk et al. found the hole mobility in unipolar P3HT diodes to increase weakly, by a factor of three, when raising the hole density by one order of magnitude from 2×10^{22} m^{-3} to 2×10^{23} m^{-3}, with an even weaker dependence of μ_h on n at lower hole densities.[181]
The results of k as a function of carrier density for the annealed devices in this work follow the trend shown in the work by Tanase et al., suggesting that acceleration of BMR at higher carrier densities is indeed caused by higher mobilities due to trap filling, but that this effect is rather moderate throughout the carrier densities considered here.
For the as prepared device, the data in Figure 5.6 suggest a very weak, but continuous decrease of k with n which was also observed in the TDCF analysis. It is worth pointing out that the experimental conditions for the BACE experiment were chosen such to measure reliable carrier densities, using a 200 nm device and high illumination intensities up to 400 mW/cm^2 (corresponding to the illumination of 4 suns). The simulations in Figure 5.7 (left) shows that under these conditions the carrier distributions in the device are very homogeneous, despite the large mismatch of electron and hole mobility (μ_h was chosen $10^{-3} \times \mu_e$ in this simulation). Also, the BMR coefficients derived from the simulated n_{extr} are constant and correspond exactly to the input value of the simulation. Therefore, it can be ruled out, that the observed decrease of k with n is an experimental artefact arising from imbalanced mobilities, but might rather be an intrinsic property of the CF-cast as prepared blend.
An alternative model is suggested, which considers that the photogenerated holes

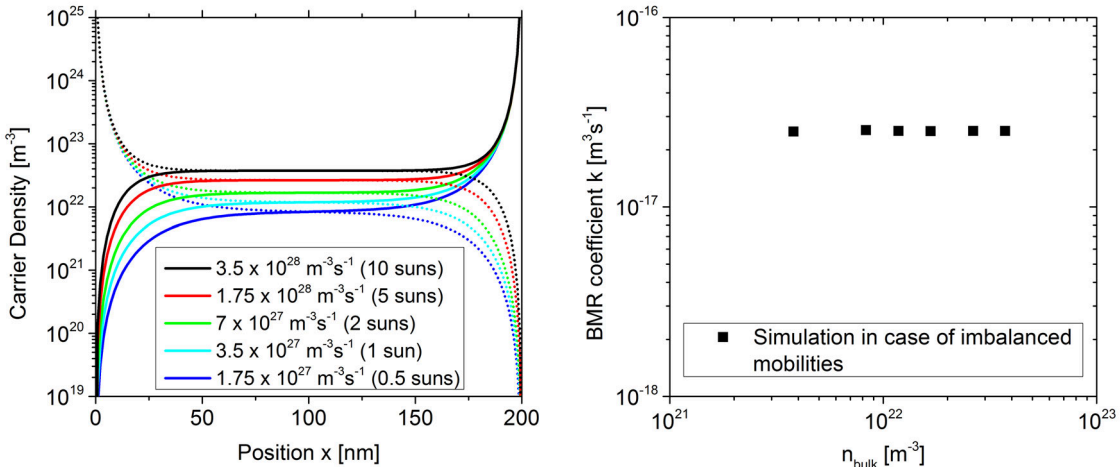

Figure 5.7: Left: Simulated carrier density profiles for a device with highly imbalanced mobilities (parameters from as prepared P3HT:PCBM in Table 6.1). Right: BMR coefficients determined from n_{bulk} from the left graph.

are rather immobile, but is not captured by the steady state simulation. Photogeneration of charges in the as-prepared blends can thus be interpreted as photodoping, where the mobility of one charge carrier type is much higher than that of the countercharge. Arkhipov pointed out that ionized dopants cause a broadening of the DOS distribution, owing to the Coulomb attraction of mobile charge carriers, which effectively results in a reduction of the mobility of the doping induced mobile carrier at low-to-moderate doping concentrations.[182, 183] The model quantitatively reproduced data on electrochemically doped P3HT by Jiang et al.[184], and its general predictions were fully confirmed by recent studies on molecularly doped polymers.[185, 186] Due to the strong interpenetration of the electron and hole conducting phase in as prepared blends, the distortion of the DOS in the electron-transporting phase, due to trapped holes on small polymer crystallites, might indeed be quite severe, slowing down the diffusive motion of photogenerated electrons in their search for recombination partners.
Irrespective of the exact mechanism causing the observed decrease of k with n, this dependence is rather moderate and k can be considered as constant (within a factor of two) throughout the steady state illumination range studied here. Therefore, both charge extraction methods, BACE and TDCF, prove the recombination coefficient to be rather insensitive to carrier density in the working regime of the solar cell for both as prepared and annealed CF cast P3HT:PCBM blends. Within this regime, the BMR coefficient is ≈ 40 times higher in the as prepared device compared to the annealed device.

5.4.2 PTB7:PCBM

For comparison, BACE experiments were also performed for PTB7:PCBM blends with and without the solvent additive DIO. Importantly, these devices exhibited layer thicknesses of 100 nm. The plot of the normalized extracted charge as a function of extraction voltage at 100 mW/cm^2 illumination intensity (inset of Figure 5.8) shows that significant losses at low extraction biases are expected for both devices. In the device with DIO only about 90% and in the device without DIO only about 80% of the charges are extracted at 0 V external bias, compared to high reverse extraction voltages. This effect is attributed mainly to higher recombination, as compared for example to annealed P3HT:PCBM, and is expected to increase with increasing illumination intensity. Therefore, a high external voltage is essential for sufficient extraction of all photogenerated carriers at all intensities and a conventional CE experiment would significantly underestimate the true carrier density. The extraction voltage was set to -2.5 V in the following studies.
For the device with DIO, the slope of the log-log plot of carrier density as a function of intensity (Figure 5.8, left) is very close to 1/2, indicating that nongeminate recombination dynamics follow a second order process. Consequently, the recombination coefficient shows almost no dependence on the charge carrier density (Figure 5.8, right). This behaviour is expected for material combinations with little or no energetic disorder.
In contrast, for the device without DIO, the charge carrier density increases with

illumination intensity with a slope of 0.31 for most of the intensity range. This was often attributed to bimolecular recombination with a carrier density dependent recombination coefficient leading to an apparent higher (third) order recombination process.[15, 93] Consequently, k increases almost linearly with n at low and intermediate carrier densities. Only for the highest investigated intensities the data can be fitted with a slope of 1/2 and k becomes independent of n.
Overall, the recombination without DIO is faster than with DIO, except for the very small carrier densities shown here. For example for one sun illumination intensity (corresponding to 100 mW/cm^2) the BMR coefficients are $k = 3 \times 10^{-17}$ m^{3}s^{-1} (w/o DIO) and $k = 1.2 \times 10^{-17}$ m^{3}s^{-1} (with DIO). The values for k with DIO are in very good agreement to recombination coefficients reported recently by Deledalle et al. for ca 90 nm thick DIO processed blends for carrier concentrations above 10^{22} m^{-3} (shown in graph).[90] In contrast to this, Rauh et al. reported a relatively pronounced increase of k with carrier density, also for DIO processed devices, with k ranging between 2×10^{-18} m^{3}s^{-1} and 8×10^{-18} m^{3}s^{-1} for n increasing from 1.5×10^{22} m^{-3} to 4×10^{22} m^{-3} at 300 K.[168] The reasons for the different carrier density dependencies and lower absolute values of k seen by Rauh et al., may in part be due to the fact that classical CE instead of BACE was used in their study.

As pointed out before, a dependence of k on carrier density was initially attributed to a density dependent mobility in the presence of a broadened DOS due to increased energetic disorder or traps.[93, 179] However, it was pointed out above that an inhomogeneous spatial distribution of charge carriers in the device can result

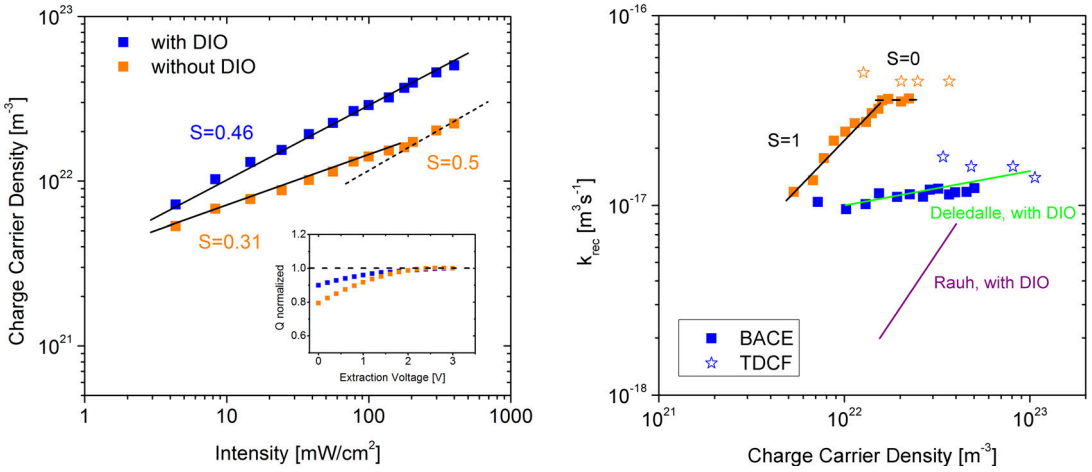

Figure 5.8: Left: Charge carrier densities at open circuit conditions for different illumination intensities determined by BACE. The extraction voltage was -2.5 V. The straight lines indicate a slope of 0.46 for the device prepared with DIO and a slope of 0.31 for the device without DIO. The dashed line indicates a slope of 1/2. Inset: Normalized extracted charge as a function of extraction voltage at 100 mW/cm^2 illumination. Right: BMR coefficients as a function of charge carrier density. Symbols: measurements from this work; Solid lines: trends reported in the literature.[90, 168]

in an apparent density dependence of the mean recombination coefficient, see also reference [90]. In fact, there it was shown that for low carrier densities and thin devices, a steep increase of $k(n)$ becomes visible, similar to what is seen for the device without DIO, which is most probably caused by the inhomogeneous carrier distribution at low illumination intensities.
Motivated by the results of this study, a simulation of steady state carrier distributions for a 100 nm device was performed, using the device parameters of the PTB7:PCBM blend without DIO. The recombination mechanism used in this simulation was bimolecular with a BMR coefficient of $k = 3 \times 10^{-17}$ m^{3}s^{-1}. The results of the charge carrier distribution for different generation rates are shown in Figure 5.9 (left). For clarity, only the hole densities are shown, however, the electron densities show similar behaviour at all generation rates. It is clear that for all generation rates up to 3.4×10^{28} m^{-3}s^{-1} (which generates a V_{OC} corresponding to an illumination intensity of 5 suns) the density profiles are very inhomogeneous and no distinct plateau with a constant carrier density can be observed, except for the highest intensity. The dashed lines in the graph mark n_{extr} according to Equations (5.3) - (5.5). Except for the highest generation rate, n_{extr} is clearly dominated by the high space charge at the extracting electrode and varies only little with light intensity. Consequently, the slope of n_{extr} versus generation rate (illumination intensity) is smaller than 1/2, see right graph of Figure 5.9. In fact, in this example the slope is 0.37 which is very close to the experimentally observed value.
These simulations confirm the assumption, that the observed slope of 0.3 is not caused by a third order recombination process, but is rather an experimental artefact due to the inhomogeneous carrier distributions and dominant egde effects in the

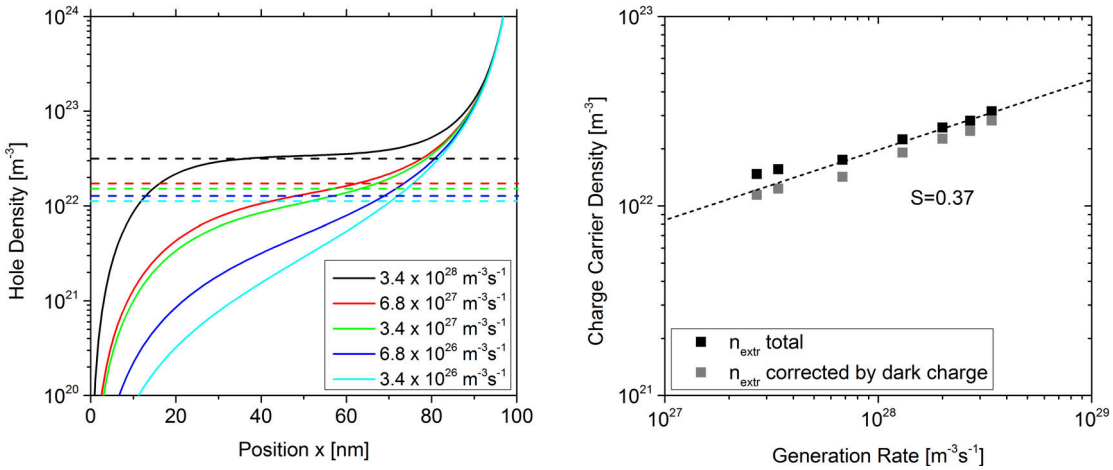

Figure 5.9: Left: Simulated carrier density profiles (holes) for a 100 nm device (parameters from PTB7:PCBM without DIO). Dashed lines indicate the carrier densities that would be extracted with BACE. Right: Extracted carrier densities (taken from the left graph) vs generation rate with and w/o dark correction by $n_{dark} = 3.3 \times 10^{21}$ m^{-3} at 0 V. The solid line indicates a slope of 0.37.

thin devices. Only at the highest intensities start the bulk properties to dominate the processes and the extracted carrier densities and recombination coefficients become reliable.
In comparison, the BMR coefficients obtained from TDCF measurements, where a relatively homogeneous charge carrier profile is generated, vary only little with carrier density for the two types of blends and agree quite well with steady state coefficients at the highest carrier densities. Therefore, in the device analysis in the following chapter, the recombination process was assumed to be strictly bimolecular and k to be independent of carrier density.

Interestingly, for the device with DIO, even though it was also only of 100 nm thickness, the carrier density increases with light intensity according to a slope of 1/2. The reason is probably that higher generation rates at the respective light intensities and the smaller recombination coefficient, compared to the blend without DIO, lead to higher carrier densities and more homogeneous carrier distributions.
Considering again the dark carrier distribution for different device thicknesses (Figure 5.4, middle), the 100 nm devices show, compared to larger layer thicknesses, a very broad and distinct space charge region. Therefore, very high photogenerated carrier densities are necessary to form homogeneous carrier distributions in the device. From that point of view it seems to be more appropriate to use larger layer thicknesses of 200 nm or more for BACE measurements. On the other hand, it is known, that the preparation of larger layer thicknesses can considerably change the nanomorphology in the blend and may lead to completely different device properties, including transport and recombination.[187] Therefore, when choosing the appropriate device thickness for the experiment, one has to consider carefully the error that is made by the measurement at thin layers versus the error that might occur from morphology changes at higher film thicknesses. In cases where the blend is known to be very sensitive to preparation conditions, as in PTB7:PCBM, it is more useful to measure at the optimized device thickness (100 nm) and in return consider only the highest possible illumination intensities.

5.5 Discussion

In this chapter organic solar cell devices were investigated under steady state operating conditions. First of all, numerical drift-diffusion simulations showed that the charge carrier distribution in the device under continuous illumination largely depends on the injection barrier height, the active layer thickness and the illumination intensity.
It is further shown, that the injected carrier density in the dark, measured at different forward biases with BACE is a good reference for the actual injection barrier height in the device and that very low barriers (< 0.1 eV) are common in most high efficiency solar cells.
More importantly, the simulations revealed that the phrase *charge carrier density*, as it is commonly used in extraction experiments is only meaningful for large layer

thicknesses (usually well above 100 nm) and high carrier densities, when a homogeneous carrier distribution in the device is formed.
Particularly at high carrier densities, but also in general in devices with high recombination or poor transport, conventional CE methods are not sufficient to extract all photogenerated charge carriers from the device. Therefore, the new technique BACE (*Bias Assisted Charge Extraction*) was introduced for a more precise determination of steady state carrier densities. The application of a high reverse extraction voltage significantly reduces the extraction time and with that potential losses due to recombination. In addition, the high external field enhances extraction, if space charge effects or deep traps hinder extraction. For three out of the four investigated device types it was shown that without the external voltage significant losses would occur and the charge carrier density would be seriously underestimated.
The charge carrier density as a function of illumination intensity was then measured with BACE for the four model devices (as prepared and annealed P3HT:PCBM and PTB7:PCBM with and without DIO) and from that the steady state recombination coefficients as function of carrier density were determined. In all cases, the results are very close to BMR coefficients determined with TDCF. Therefore it can be concluded, that the charge carrier dynamics directly after pulsed excitation are similar to the steady state conditions and that the carriers equlibrate rapidly or that there is no significant energetic disorder present in these blends.
Only, in the PTB7:PCBM device without DIO the effects of an inhomogeneous carrier distribution in a thin layer became visible and lead to an apparent third order recombination process, which was also often reported in literature. However, numerical simulations and the comparison with the results from TDCF showed that this effect is due to an erroneous determination of the carrier density with BACE, due to inhomogeneous carrier profiles, and that the true recombination process is bimolecular with a constant recombination coefficient.

6 Current-Voltage Characteristics

6.1 Introduction

The specific shape of the current density-voltage ($J-V$) characteristics of an organic solar cell is determined by the balanced competition between charge carrier generation, recombination and transport of carriers to the electrodes. The relevant parameters, connected to these physical processes, are the charge carrier generation rate G with a possible field dependence, the bimolecular recombination constant k and the electron and hole mobilities, μ_e and μ_h, respectively. In the previous two chapters, these parameters were experimentally determined by a variety of techniques and discussed for four different types of blends - P3HT:PCBM (annealed and as prepared) and PTB7:PCBM (with and without DIO). Furthermore, the measurements revealed oblique information about energetic disorder and true recombination order in these blends.
In the next step a numerical drift-diffusion simulation shall be used to examine whether the experimentally determined dynamic parameters are capable to explain the measured $J-V$ characteristics of the investigated devices. It turns out that using the measured parameters as input parameters, the simulation reaches excellent agreement with the experimental data for a wide range of illumination intensities. Thus, the measurement techniques and device analysis presented in this work enable a full description of the solar cell characteristics and provide a profound understanding of the dynamic processes in organic solar cells.
The results for the model devices made of P3HT:PCBM and PTB7:PCBM are shown and the simulation input parameters are discussed with respect to validity and unambiguity. Furthermore, the influence of surface recombination at the contacts is discussed and shown to be negligible under the conditions considered here. Finally, all results are discussed in the context of previous publications and the specific blend morphologies.

6.2 P3HT:PCBM

Figure 6.1 shows the experimental $J-V$ characteristics, measured at different light intensities relative to one sun (symbols) together with the simulation results (solid lines) for the annealed (left) and the as prepared (right) P3HT:PCBM blends. The parameters used in the simulation for 1 sun illumination intensity are summarized in Table 6.1, together with the source of the respective parameters. In accordance with the TDCF results a field-independent generation rate was used for **both devices** and all intensities and, consistent with BACE, no energetic disorder was considered in the simulation.
For the **annealed** device, the generation rate at one sun illumination intensity was determined from the short circuit current density via $G = J_{SC}/ed = 3.6 \times 10^{27}$ $m^{-3}s^{-1}$. The generation rates used for the lower intensities scale with the relative illumination and are listed in Table 6.2. The bimolecular recombination coefficient k was set to 1.6×10^{-18} m^3s^{-1} as determined from the BACE measure-

ments at high illumination. The electron mobility, $\mu_e = 1.2 \times 10^{-3}$ cm^{2}V^{-1}s^{-1}, was taken from the extrapolation of TDCF photocurrent transients and the hole mobility, $\mu_h = 3 \times 10^{-4}$ cm^{2}V^{-1}s^{-1}, from the numerical fit to the transients. Both values are independent of the electric field within the considered range. Note, that the hole mobility determined by SCLC measurements is about a factor of 2 smaller than the value used here. However, the simulation of the $J - V$ curves responds very sensitively to the charge carrier mobility and the reduction of μ_h by a factor of 2 decreases the fill factor from 67% to 57% (dashed orange line in Figure 6.1).
Finally, the electron and hole injection barriers were set to the lowest possible value at which the simulation still runs stable, $\phi_B = 0.01$ eV. This value is consistent with the extraordinary high dark charge found in these devices at forward bias.
The excellent agreement of the simulation with the experimental data for an intensity range covering two orders of magnitude indicates that a field-independent generation rate and constant (field- and density-independent) recombination coefficient perfectly describe the $J - V$ characteristics of the annealed P3HT:PCBM device.
As discussed extensively in Chapter 4, the same generation rate is proposed for the **as prepared** device as for the annealed device. At the same time, the recombination kinetics were found to be about one order of magnitude faster for carrier densities which are typical for steady state illumination at one sun or below. The increased BMR coefficient k has often been proposed to be responsible for the lower FF and J_{SC} in the as prepared blends.[132, 159] Figure 6.1 (right) shows that an increase of k by one or two orders of magnitude indeed reduces the FF, J_{SC} and

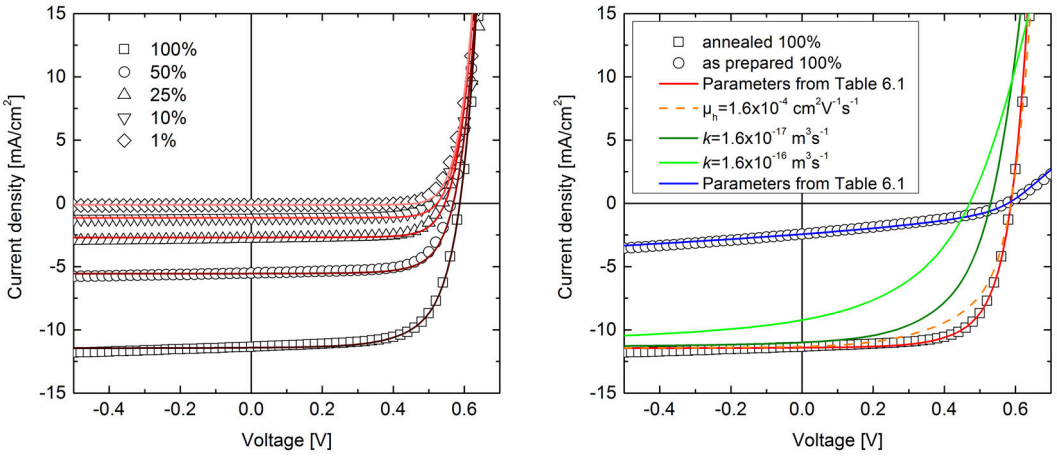

Figure 6.1: Left: $J-V$ characteristics at different light intensities relative to one sun for the annealed device. Symbols are the experimental data and solid lines are drift-diffusion simulations (for more details see text). Right: A reduction of the hole mobility by a factor of 2, as measured by SCLC for the annealed device, decreases considerably the FF (orange dashed line). Increasing only k by one or two orders of magnitude (dark and light green lines) cannot resemble the measured $J - V$ curve of the as-prepared blend. Only highly imbalanced mobilities can explain the shape of the curve (blue line).

V_{OC}, compared to the annealed device. However, variation of only this particular parameter cannot resemble the shape of the as prepared $J-V$ curve. The $J-V$ characteristics can, however, be fully reproduced using the parameters in Table 6.1, with $k = 2.5 \times 10^{-17}$ m^{3}s^{-1} (from BACE) and a hole mobility that is approximately three orders of magnitude lower than in the annealed blend. Such a low hole mobility in the as prepared blend is in very good agreement with the results of the SCLC measurements in Chapter 4.
As shown by Goodman and Rose, the large mismatch between electron and hole mobility will lead to a build-up of space charge in the device.[188] The space charge screens the electric field in the interior of the active layer and detains the carriers from extraction. This leads to a significant reduction of the fill factor. In the case of space charge limited current, the photocurrent is completely determined by the mobility of the slower charge carrier and can be described with an analytical model as suggested by Mihailetchi et al. [189]:

$$J_{\mathrm{ph}} = q\left(\frac{9\varepsilon_0\varepsilon_r\mu_h}{8q}\right)^{1/4} G^{3/4}V^{1/2} \tag{6.1}$$

Figure 6.2 (left) shows experimental $J-V$ curves for different light intensities with the fits according to Equation (6.1). The very good agreement of the fits and the data indicates that the performance of the as prepared devices is indeed dominated by space charge effects.
Also shown in Figure 6.2 (right) are the results of the numerical simulation for different light intensities with the respective generation rates listed in Table 6.2. Note, that for these simulations an electron injection barrier of $\phi_e = 0.39eV$ was introduced to account for the slowly rising current density at voltages above V_{OC}.

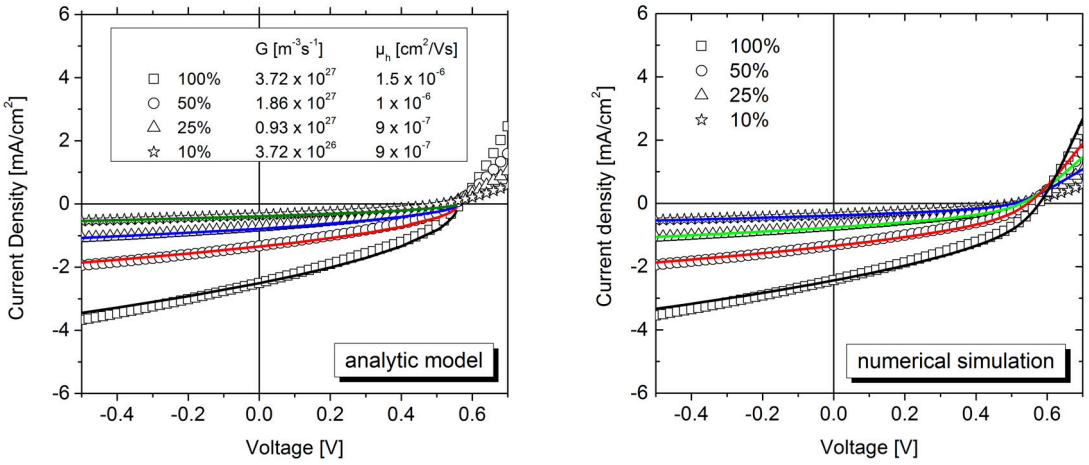

Figure 6.2: Left: Fit of the as prepared data with the analytical model for space charge limited photocurrent from reference [189] for different light intensities. The inset gives the parameters used for the generation rate and the hole mobility. Right: Numerical simulation to the same data using the parameters from Table 6.1 and 6.2.

Parameter	annealed	source	as prepared	source
Generation Rate $[m^{-3}s^{-1}]$	3.6×10^{27}	J_{SC}	3.6×10^{27}	TDCF
BMR coefficient $[m^3s^{-1}]$	1.6×10^{-18}	BACE (TDCF)	2.5×10^{-17}	BACE (TDCF)
electron mobility $[cm^2/Vs]$	1.2×10^{-3}	TDCF (extrapolation)	1.0×10^{-3}	TDCF (extrapolation)
hole mobility $[cm^2/Vs]$	3×10^{-4}	TDCF (fit)	5×10^{-7}	best fit in simulation
Injection Barriers [eV]	$\phi_e = \phi_h = 0.01$	dark charge	$\phi_e = 0.39$ $\phi_h = 0.05$	dark charge
effective bandgap [eV]	1.09	best fit	1.17	best fit

Table 6.1: Parameters used for the drift diffusion simulation of the as prepared and annealed P3HT:PCBM $J-V$ curves at 1 sun illumination intensity.

Intensity (1 sun)	Generation Rate $[m^{-3}s^{-1}]$ annealed	as prepared
100%	3.6×10^{27}	3.6×10^{27}
50%	1.75×10^{27}	1.8×10^{27}
25%	8.5×10^{26}	8.5×10^{26}
10%	3.6×10^{26}	3.5×10^{26}
1%	3.6×10^{25}	-

Table 6.2: Generation rates used when fitting the $J-V$ characteristics of the as prepared and annealed P3HT:PCBM blends for different light intensities relative to 1 sun.

This relatively high barrier leads to a very low dark electron density in the device also at high forward biases. For example, the simulated electron charge in the dark according to Equation (5.4) at $V = 0.55V$ is $Q_e \approx 3 \times 10^{-12}$ C. This value is below the resolution of our BACE setup and, considering that the holes in the device are too slow to be extracted, it corresponds well to the fact that no dark charge could be measured in the as prepared devices.
Finally, it has to be noted that the effective bandgap, defined as the difference of the acceptor-LUMO and donor-HOMO energy, used for the simulations was chosen such that the simulated curve matches the experimental curve at V_{OC}. The resulting bandgaps were 1.17 eV and 1.09 eV for the as prepared and annealed devices, respectively. These parameters cannot be understood as fixed physical values, since they strongly depend on the underlying density of states N_0. Here, a fixed value of $N_0 = 10^{27}$ m^{-3} was used for all simulations, which corresponds approximately to one transport state per nm^3 and is commonly used in literature.[92, 190–192] However, the trend of a reduction of the bandgap upon thermal annealing is in accordance with the results of Kelvin probe measurements, where a reduction of the difference of electron and hole pinning levels upon annealing was observed.[193]

6.3 Influence of Surface Recombination

In the preceding simulations the only loss process considered was bimolecular recombination in the bulk. However, surface recombination of minority carriers at the contacts reduces the carrier densities at the electrodes and is therefore also a potential loss process that has to be considered. Surface recombination at the electrodes relates the current to the minority densities at the electrodes:

$$J_{\mathrm{n(p)}} = qS_{\mathrm{n(p)}}[n(p) - n(p)_{\mathrm{eq}}], \tag{6.2}$$

where $J_{\mathrm{n(p)}}$ is the electron (hole) density at the anode (cathode), $S_{\mathrm{n(p)}}$ is the surface recombination velocity, $n(p)$ is the electron (hole) density at the electrode, and $n(p)_{\mathrm{eq}}$ is the equilibrium carrier density at the electrode. No estimates of the (finite) surface recombination velocity exist, making it difficult to judge how important this loss process is.[136] Assuming that the minority carrier densities at the contacts are equal to their equilibrium values is equivalent to infinite surface recombination.[194] This represents a possible loss mechanism as the carrier densities at the contacts remain constant regardless of the photogeneration of carriers in the bulk.
The other limit (vanishingly small surface recombination) allows for more minority carriers at the contacts and corresponds to selective contacts: minority carriers cannot exit the device at the wrong contact. Selective contacts have earlier been suggested by Shuttle et al. who found that the dark current in annealed P3HT:PCBM devices is dominated by bimolecular recombination.[170] Also, several authors suggested that PEDOT:PSS efficiently works as an electron blocking layer.[172, 195–197] In addition, vertical phase segregation might enhance contact selectivity.[151]
In the preceding simulations it was assumed that holes (electrons) do not flow out

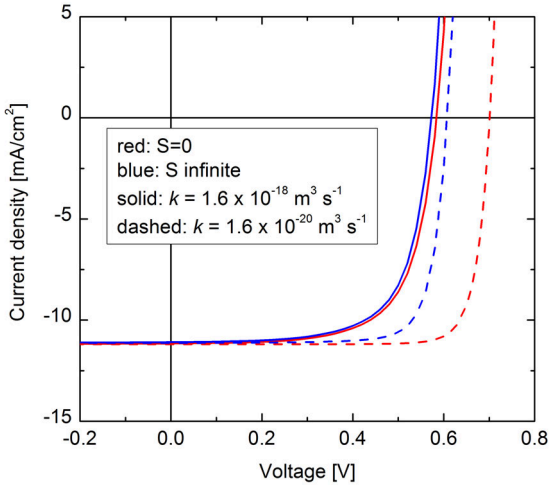

Figure 6.3: Comparison of zero (red lines) and infinite (blue lines) surface recombination for a bulk recombination coefficient of $k = 1.6 \times 10^{-18}$ m^{3}s^{-1} (solid lines). The influence of surface recombination becomes only significant if bimolecular recombination is much slower than the measured values (dashed lines).

at the electron (hole) injecting contact. Figure 6.3 compares this assumption with the other extreme, which is infinite surface recombination, where the electrodes are not selective. Surprisingly, the influence of surface recombination is negligible for the parameters investigated here. Even at the low bimolecular recombination rates ($k = 1.6 \times 10^{-18}$ m^{3}s^{-1}) found in the annealed devices, bimolecular recombination of electrons (holes) with holes (electrons) near the anode (cathode) is much stronger than the surface recombination of electrons (holes) at the anode (cathode). Only if the bimolecular recombination rate is further reduced (by two orders of magnitude) the minority carriers are able to reach the contact and the effect of surface recombination alters the $J - V$ characteristics.
In contrast, transient simulations showed that contact selectivity has a great influence on the charge carrier decay dynamics after a short laser excitation (see appendix A.9). In the case of non-selective contacts the charge carriers can leave the device at both contacts which leads to an additional diffusion dominated decay channel. The simulations show that in this case the decay dynamics proceed on a much faster time scale (by one order of magnitude) which is not observed in the experiments. Therefore, selective contacts are assumed to be present in the P3HT:PCBM devices.

6.4 PTB7:PCBM

In the following the numerical simulation results will be discussed for PTB7:PCBM blends with and without the solvent additive DIO. As it was shown in the previous section, the influence of surface recombination is negligible even in the presence of low bimolecular recombination rates in the order of $k = 1 \times 10^{-18}$ m^{3}s^{-1}. For **both PTB7:PCBM blends** k was found to be at least one order of magnitude higher.

Therefore, the surface recombination was set to infinite in the following simulations. Also, in agreement with the BACE results, energetic disorder was neglected throughout all simulations. The injection barriers for holes and electrons were set to 0.05 eV, which is the value that leads to the best concordance with the measured dark charge in both devices.

For the device **with DIO** the charge carrier generation rate was determined to be field-independent and $G = J_{\text{-3V}}/ed = 1.1 \times 10^{28}$ m^{-3}s^{-1} at one sun illumination intensity. The BMR coefficient, $k = 1.2 \times 10^{-17}$ m^{3}s^{-1}, was taken from the BACE experiments at high carrier density. The hole mobility, $\mu_h = 4.5 \times 10^{-4}$ cm^{2}V^{-1}s^{-1}, was taken from the extrapolation of the TDCF transients and the electron mobility, $\mu_e = 3 \times 10^{-4}$ cm^{2}V^{-1}s^{-1}, from the numerical fit to the same transients. Both values are found to be independent of the electric field.

All parameters are summarized in Table 6.3. The left graph in Figure 6.4 shows the experimental $J - V$ characteristics for the blends prepared with DIO measured at different light intensities (symbols) together with the simulation results (solid lines). The excellent agreement of the simulation with the data for an intensity range of two orders of magnitude indicates that a field-independent generation rate and a moderate bimolecular recombination rate with a carrier density independent recombination coefficient, in competition with efficient extraction of both electrons and holes, sufficiently explains the $J - V$ characteristics. The generation rates used for the fits at different intensities are listed in Table 6.4.

For the device **without DIO** a field-dependent generation was measured with TDCF. As could be seen from Figure 4.3 the generation is fairly constant in the region from -2 V up to approximately -0.7 V and then drops by 20% from -0.7 V to 0.7 V. This drop was approximated by a linear decrease. Using this parametriza-

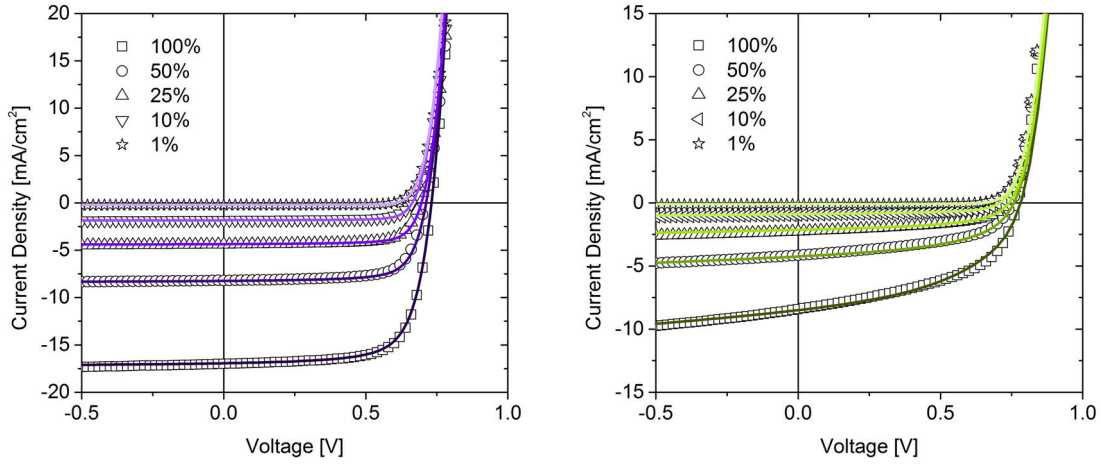

Figure 6.4: $J - V$ characteristics at different light intensities relative to one sun for the devices prepared with (left) and without DIO (right). Symbols are the experimental data and solid lines are drift-diffusion simulations (for more details see text). The simulation parameters are summarized in Table 6.3 and 6.4.

Parameter	with DIO	source	w/o DIO	source
Generation Rate $[m^{-3}s^{-1}]$	1.1×10^{28}	$J_{\text{-3V}}$	6.5×10^{27} at -0.7 V	TDCF
BMR coefficient $[m^3s^{-1}]$	1.2×10^{-17}	BACE	4.5×10^{-17}	TDCF
electron mobility $[cm^2/Vs]$	3×10^{-4}	TDCF (fit)	2.7×10^{-5}	best fit in simulation
hole mobility $[cm^2/Vs]$	4.5×10^{-4}	TDCF (extrapolation)	1.2×10^{-3}	TDCF (extrapolation)
Injection Barriers [eV]	$\phi_e = \phi_h = 0.05$	dark charge	$\phi_e = \phi_h = 0.05$	dark charge
effective bandgap [eV]	1.27	best fit	1.36	best fit

Table 6.3: Parameters used for the drift diffusion simulation of the PTB7:PCBM $J-V$ curves at 1 sun illumination intensity.

Intensity (1 sun)	Generation Rate $[m^{-3}s^{-1}]$ with DIO	w/o DIO
100%	1.1×10^{28}	6.5×10^{27}
50%	5.3×10^{27}	3.2×10^{27}
25%	2.8×10^{27}	1.6×10^{27}
10%	1.2×10^{27}	6.7×10^{26}
1%	1.3×10^{26}	6.7×10^{25}

Table 6.4: Generation rates used when fitting the $J-V$ characteristics of the PTB7:PCBM blends with and without DIO for different light intensities relative to 1 sun.

tion, an effective generation rate was calculated for each bias voltage and taken as input parameter for the simulation. Note, that in most simulations, the generation rate is related to the local electric field via a Braun-Onsager-type model.[14] This approach also takes into account a distribution of generation rates in the device due to an inhomogeneous field. However, our approach has two advantages. First, the parameters needed for the Braun-Onsager model are hard to access by experiments and are usually estimated from drift-diffusion simulations themselves. Also, it was shown that in many cases the model delivers unphysical parameters. Second, the field-dependence measured with TDCF is also an average over the entire device for each applied external bias. Even though this approach does not yield any information about the exact mechanism causing the field-dependent generation rate, it seems more appropriate to be used here.
The recombination coefficient was set to $k = 4.5 \times 10^{-17}$ $\mathrm{m^3 s^{-1}}$, independent of carrier density, as determined with TDCF. As extensively discussed in Chapter 5.2, the homogeneous carrier distribution in the TDCF experiment leads to more reliable results for k than BACE for the blend without DIO.
The field-dependent hole mobility, $\mu_h = 1.2{\times}10^{-3}$ $\mathrm{cm^2 V^{-1} s^{-1}}$ and $\beta = -0.002\sqrt{\mathrm{cm/V}}$, was taken from the extrapolation of the TDCF transients. The electron mobility is the parameter with the highest experimental uncertainty. The value achieving the best fit to the experimental $J-V$ curves is $\mu_e = 2.7 \times 10^{-5}$ $\mathrm{cm^2 V^{-1} s^{-1}}$, which is in very good agreement with the value determined from transient fit ($\mu_e = 2.7 \times 10^{-5}$ $\mathrm{cm^2 V^{-1} s^{-1}}$). Note that the electron mobility is significantly lower compared to the device with DIO, which supresses the FF. The results for the experimental and simulated $J-V$ curves at five different illumination intensities are shown in Figure 6.4 (right) and the simulation parameters are listed in Tables 6.3 and 6.4. Again, very good agreement was achieved for all intensities for one set of parameters, showing that energetic disorder and a density dependent mobility are not necessary to describe the $J-V$ characteristics. It is therefore proposed that the density dependent recombination coefficient observed in the BACE measurement is mostly a consequence of inhomogeneous carrier distributions due to imbalanced mobilities and high recombination and with that, indirectly, a consequence of the morphology with large donor and acceptor phases.
Note that the resulting bandgaps used in these simulations were 1.27 eV and 1.36 eV for the devices with and without DIO respectively (at one sun illumination). Effective bandgaps determined by analysing the V_{OC} as a function of carrier density (see appendix A.8) are in very good agreement with the values used here and confirm the trend of a reduction of ca 90 meV upon adding DIO, most likely caused by a change in domain morphology.
Importantly, the addition of DIO causes only minor to moderate changes of the individual dynamic parameters. Therefore the variation of only one of these parameters cannot explain the dramatic improvement of the performance when DIO is added. This is demonstrated in Figure 6.5, where the experimental $J-V$ curves of the device w/o DIO are compared to parametric simulations starting with the parameters used for the devices with DIO (black lines in Figure 6.5). The generation rate (at

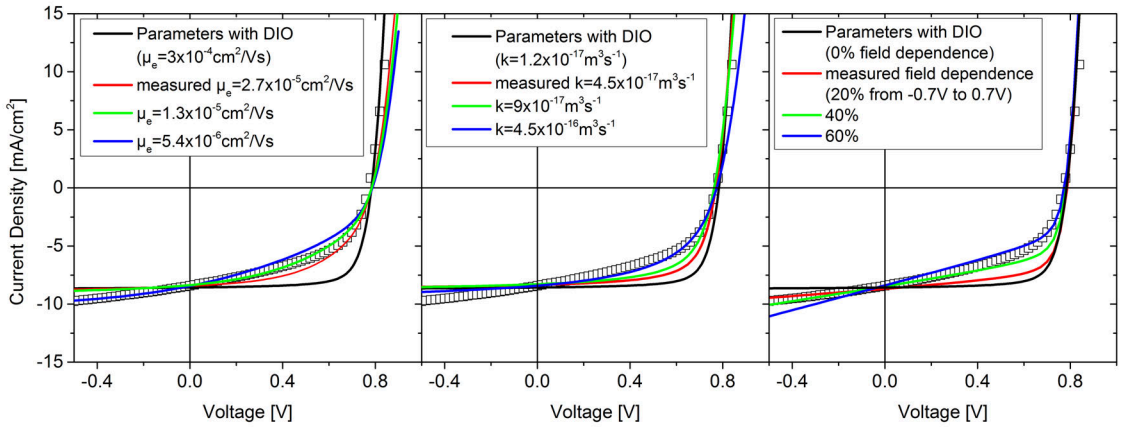

Figure 6.5: Experimental $J-V$ curves (symbols) for the blend without DIO, compared to parametric simulations (lines). In all curves, the black line displays the simulation with the parameters used for the device processed with DIO (s. Table 6.3). Then, only one parameter was changed while all the others were kept the same as in the DIO processed case. Left: only the electron mobility is stepwise reduced. Middle: only the BMR coefficient k is increased. Right: only the field dependence of generation is increased. In the simulations, the effective bandgap and the generation rate (at -0.7V) are adjusted to yield the same V_{OC} and J_{SC} for all curves. All other parameters are kept constant.

-0.7 V) and the effective bandgap were adjusted to achieve the same J_{SC} and V_{OC} for all simulated curves. As expected, this simulation leads to a much higher FF than was measured in devices without DIO.
Then, either only the electron mobility was stepwise reduced (left), the BMR coefficient k was increased (middle) or the field dependence of generation was increased (right). In each graph, the red lines show the simulation when using the value of the specific parameter as measured on the blend without additive, while the green and blue lines use values that further decrease the overall performance. Though in some cases parts of the $J-V$ curve are well resembled by the simulation, the applied parameters differ largely from the measured values. For example, the fourth quadrant of the $J-V$ curve can be well fitted by only increasing the value of k to 3×10^{-16} m^{3}s^{-1}, but this value is unrealistically large. Furthermore, these parameters fail to explain the $J-V$ characteristics over the full voltage range. The specific shape of the curve can, therefore, not be ascribed to the change of only the mobility, only the recombination or only the field-dependence of generation. Likewise, if the change of one of the parameters, for example the electron mobility, is neglected, the device FF and performance will be overestimated, as it was for example observed by Foertig et al.[26] It is only when the changes of all three parameters upon DIO addition are taken into account that the simulation matches the experimental $J-V$ characeristics under all illumination conditions and for a wide range of voltages.

6.5 Discussion

In summary it has been shown that the dynamic parameters for charge carrier generation, recombination and transport, having been experimentally determined in this work are capable to explain the steady state $J - V$ characteristics under different illumination intensities.
For the annealed P3HT:PCBM device all data can be consistentliy explained by a field-independent generation of free charge carriers at the donor-acceptor interface and strict bimolecular recombination in competition with efficient extraction of both electron and holes. This is in accordance with a uniform morphology of well interconnected donor and acceptor domains.
For the as prepared P3HT:PCBM the generation rate was also found to be fully independent of electric field in the solar cell working regime. The results also indirectly imply that as prepared and annealed devices have similar internal quantum efficiencies, despite the very different morphologies. However, the free carrier lifetime is much shorter in the as prepared blend, due to a higher bimolecular recombination coeffcient. This leads to significant recombination losses at short circuit conditions. However, the simulations of the $J - V$ characteristics under illumination showed that the significantly poorer performance cannot be explained solely on the basis of an enlarged BMR coefficient. Experiments and simulations show consistently that space charge effects, due to a very low hole mobility and a resulting imbalanced charge extraction are the main cause for the low FF and the low J_{SC} in these devices. It has been previously reported that $\approx 30\%$ of the polymer chains are in the aggregated state in as prepared CF-cast P3HT:PCBM blends.[118] While this concentration seems to ensure efficient charge generation, it is too low to guarantee rapid extraction of photogenerated holes to the electrodes.
In contrast to the P3HT:PCBM devices, the blends comprising the low bandgap copolymer PTB7 exhibit a broader absorption spectrum with a higher spectral overlap to the sun emission. This leads to higher overall generation rates in both devices compared to the homopolymer:fullerene blends, as was confirmed by our measurements. For the optimized devices with DIO all data can again be consistently explained by the combination of a field-independent free charge carrier generation, a moderate bimolecular recombination with a carrier density independent recombination coefficient and efficient extraction of both electron and holes. The experimental results are consistent with a uniform morphology of well interconnected donor and acceptor domains of the size of the exciton diffusion length.
For the devices prepared without DIO the overall charge carrier generation efficiency is reduced compared the blend with DIO. This is consistent with a structural model where large fullerene clusters are embedded into a polymer rich surrounding. As already pointed out by Collins et al.[123] this particular morphology will lead to inefficient exciton harvesting, due to a small active interface. Furthermore, the generation rate was found to be field-dependent, in particular when exciting primary the polymer. However, the drift-diffusion simulations show unamiguosly that the lower performance of the devices without DIO cannot be explained solely on the basis of a field-dependent generation and a higher coefficient for non-geminate recombination.

Instead, the effect of the additive on the entire $J-V$ characteristics can only be reproduced when, in addition taking into account a reduced electron mobility in the device processed without DIO, causing inefficient electron extraction and a poor fill factor.
To conclude, the experiments on four different blends show that the shape of the $J-V$ characteristics is very specific for each device and depends on all the dynamic parameters. This emphasizes the necessary knowledge and consideration of these parameters. Interestingly, for all blends the generation efficiency did not (or only weakly) depend on the applied bias, meaning that the $J-V$ curves were largely determined by the competition between extraction and non-geminate recombination. Thereby, annealing or processing with DIO affected all relevant parameters (G, k, μ_e and μ_h). Consequently the measurement and discussion of only a subset of parameters cannot lead to a complete understanding of the whole device.
On the other hand, it turned out that the simulation responds very sensitively to the variation of single parameters. It might therefore be possible to attribute changes of the $J-V$ curves when modifying the preparation protocol to the variation of only the mobility, the BMR coefficient or the generation rate. This work shows that this approach is erroneous. Instead, in this work, all parameters for reproducing the measured $J-V$ characteristics were taken from measurements with suitable measurement techniques. It is only when these parameters are combined that the $J-V$ curves can be reproduced over the entire ranges of bias and illumination intensities. Therefore, the measurement techniques for determining the dynamic solar cell parameters together with the numerical drift diffusion simulations presented in this work, provide a powerful algorithm for a complete description and comprehensive understanding of the working principle of organic solar cells.

7 Summary and Outlook

This thesis provides a deep understanding of the dynamic processes and physical parameters determining the performance of polymer based heterojunction solar cells. A new approach for explaining the characteristic current-voltage output was developed combining the experimental determination of charge carrier generation, recombination and transport and the application of numerical device simulations. For the first time, all relevant parameters were successfully determined from experiments and confirmed by the numerical simulations.

One of the main achievements of this work was the advancement of the *Time Delayed Collection Field* (TDCF) method from a former μs time resolution to a ns regime with 20 ns pulse rise time and 100 ns time delay. In TDCF charge carriers are generated by a short laser pulse and subsequently extracted by a defined rectangular voltage pulse. During this thesis, rise time and time delay have been further improved to 10 ns each.[5] The improved temporal resolution allowed for the first time a reliable determination of the effect of an electric field on free charge carrier generation. An analytic model for the description of TDCF transients was developed and revealed the experimental conditions for which reliable results can be obtained. In particular, it turned out that the *RC* time of the setup which is mainly given by the sample geometry has a significant influence on the shape of the transients which has to be considered for correct data analysis.

TDCF has been used for the first time to measure charge carrier generation, recombination and transport with the same experimental setup. This excludes experimental errors due to different measurement and preparation conditions and demonstrates the strength of this technique. Owing the careful analysis of this work and the versatile possible applications, TDCF is now a well established technique in the field of organic solar cells, reflected by the large number of publications based on TDCF measurements in the last four years.[18, 26, 70, 71, 132–144] As an example this method has very recently been used to investigate the explicit role of the interfacial charge transfer (CT) state in the charge generation process by selectively exciting the donor, acceptor and charge transfer state manifold.[70, 71] The results suggest that the generation in OSC in general proceeds via the split-up of thermalized CT states, irrespective of the initial excitation energy, which is in great contrast to most current models.

In the course of this work another new technique *Bias Assisted Charge Extraction* (BACE) was developed to measure charge carrier densities in solar cells under real operating conditions. Here, the charge carriers photogenerated under steady state illumination are extracted by applying a high reverse bias. The accelerated extraction compared to conventional charge extraction minimizes losses through non-geminate recombination and trapping during extraction and proved to be more precise than

[5] mainly by the work of Jona Kurpiers

the current established techniques. However, numerical steady state device simulations revealed that inhomogeneous carrier distributions in the device, due to low energetic injection barriers, may lead to an erroneous determination of the bulk charge carrier density. This can result in apparently higher recombination orders, similar to what has been observed by Kirchartz et al.[89] Importantly, it could be shown that the relevant charge carrier density in the device can be determined the more precise the higher the photogenerated charge carrier density and the thicker the active layer, which should be in general greater than 100 nm. These findings are of course also true for the widely used conventional charge extraction technique and are therefore of great importance for the community.

The careful analysis of meaningful experimental conditions now enables a reliable determination of charge carrier densities under different illumination and bias conditions. The charge carrier densities under open circuit conditions, where no external currents are flowing and all generated charge carriers recombine non-geminately, were then used to determine non-geminate recombination orders as well as steady state recombination rate constants. Comparison of the recombination dynamics at steady state and at short time scales allowed to draw conclusions about the energetic distribution of transport sites. Moreover, the precise measurement of steady state carrier densities with BACE has opened up new important applications, such as quantifying the energetic contribution to the V_{OC} in donor/acceptor blends [193] and the development of a novel technique to determine effective charge carrier mobilities under solar cell operation conditions.[138] These developments show that the new BACE technique highly contributes to a fundamental understanding of organic solar cell properties.

The newly developed experimental techniques allow to sensitively analyse and quantify geminate and non-geminate recombination losses along with charge transport in organic solar cells. A full analysis was exemplarily demonstrated for two prominent polymer-fullerene blends.
The model system P3HT:PCBM spincast from chloroform (as prepared) exhibits poor power conversion efficiencies (PCE) on the order of 0.5%, mainly caused by low fill factors (FF) and currents. It could be shown that the performance of these devices is limited by the hole transport and large bimolecular recombination (BMR) losses, while geminate recombination losses are insignificant. The low polymer crystallinity and poor interconnection between the polymer and fullerene domains leads to a hole mobility of the order of 10^{-7} cm^2/Vs which is several orders of magnitude lower than the electron mobility in these devices. The concomitant build up of space charge hinders extraction of both electrons and holes and promotes bimolecular recombination losses.
Thermal annealing of P3HT:PCBM blends directly after spin coating improves crystallinity and interconnection of the polymer and the fullerene phase and results in comparatively high electron and hole mobilities in the order of 10^{-3} cm^2/Vs and 10^{-4} cm^2/Vs, respectively. In addition, a coarsening of the domain sizes leads to

a reduction of the BMR by one order of magnitude. High charge carrier mobilities and low recombination losses result in comparatively high FF (>65%) and short circuit current ($J_{SC} \approx 10$ mA/cm^2). The overall device performance (PCE $\approx 4\%$) is only limited by a rather low spectral overlap of absorption and solar emission and a small V_{OC}, given by the energetics of the P3HT.

From this point of view the combination of the low bandgap polymer PTB7 with PCBM is a promising approach. In BHJ solar cells, this polymer leads to a higher V_{OC} due to optimized energetics with PCBM. However, the J_{SC} in these (unoptimized) devices is similar to the J_{SC} in the optimized blend with P3HT and the FF is rather low ($\approx 50\%$). It turned out that the unoptimized PTB7:PCBM blends suffer from high BMR, a low electron mobility of the order of 10^{-5} cm^2/Vs and geminate recombination losses due to field dependent charge carrier generation.
The use of the solvent additive DIO optimizes the blend morphology, mainly by suppressing the formation of very large fullerene domains and by forming a more uniform structure of well interconnected donor and acceptor domains of the order of a few nanometers. Our analysis shows that this results in an increase of the electron mobility by about one order of magnitude (3×10^{-4} cm^2/Vs), while BMR and geminate recombination losses are significantly reduced. In total these effects improve the J_{SC} (≈ 17 mA/cm^2) and the FF ($> 70\%$). In 2012 this polymer/fullerene combination resulted in a record PCE for a single junction OSC of 9.2%.[30]

Remarkably, the numerical device simulations revealed that the specific shape of the $J-V$ characteristics depends very sensitively to the variation of not only one, but all dynamic parameters. On the one hand this proves that the experimentally determined parameters, if leading to a good match between simulated and measured $J-V$ curves, are realistic and reliable. On the other hand it also emphasizes the importance to consider all involved dynamic quantities, namely charge carrier generation, geminate and non-geminate recombination as well as electron and hole mobilities. The measurement or investigation of only a subset of these parameters as frequently found in literature will lead to an incomplete picture and possibly to misleading conclusions.

Most importantly, the comparison of the numerical simulation employing the measured parameters and the experimental $J-V$ characteristics allows to identify loss channels and limitations of OSC. For example, it turned out that inefficient extraction of charge carriers is a criticical limitation factor that is often disobeyed. However, efficient and fast transport of charges becomes more and more important with the development of new low bandgap materials with very high internal quantum efficiencies. Likewise, due to moderate charge carrier mobilities, the active layer thicknesses of current high-performance devices are usually limited to around 100 nm. However, larger layer thicknesses would be more favourable with respect to higher current output and robustness of production. Newly designed donor materials should therefore at best show a high tendency to form crystalline structures, as

observed in P3HT, combined with the optimized energetics and quantum efficiency of, for example, PTB7.
The findings of this work also revealed that the individual blend morphology, influenced by the specific preparation conditions, plays a very important role for the device performance and needs to be controlled in such a way that efficient charge transport is ensured while geminate and non-geminate recombination is strongly suppressed.

In future work, the analysis concept developed in this thesis may also be applied to other polymer based or small molecule OSC or to new material classes. For example, organometal halide perovskites, a class of organic-inorganic hybrid materials, are currently emerging in the field of solar energy with power conversion efficiencies surpassing 20%.[198] Despite this striking success, little is still known about the exact carrier dynamics in these devices. Only recently TDCF studies revealed that the recombination dynamics in perovskite solar cells differ significantly from those in polymer solar cells, displaying for example time dependent recombination coefficients.[199] A complete device analysis as presented in this thesis may be able to estimate the impact of time dependent recombination dynamics on the device performance and identify further limitations to enforce a target-oriented improvement of device performance.

References

[1] Perez, R. *SHC Solar Update* **50**, 2 (2009).

[2] http://en.wikipedia.org/wiki/Renewable_energy, July (2015).

[3] http://www.nrel.gov/ncpv/images/efficiency_chart.jpg, (2015-09-06).

[4] Green, M. A., Emery, K., Hishikawa, Y., Warta, W., and Dunlop, E. D. *Progress in Photovoltaics: Research and Applications* **23**, 1–9 (2015).

[5] Chiang, C. K., Fincher, C. R., Park, Y. W., Heeger, A. J., Shirakawa, H., Louis, E. J., Gau, S. C., and MacDiarmid, A. G. *Phys. Rev. Lett.* **39**, 1098–1101 (1977).

[6] Tang, C. W. *Applied Physics Letters* **48**, 183–185 (1986).

[7] Hiramoto, M., Fujiwara, H., and Yokoyama, M. *Applied Physics Letters* **58**, 1062–1064 (1991).

[8] Yu, G., Gao, J., Hummelen, J. C., Wudl, F., and Heeger, A. J. *Science* **270**, 1789–1791 (1995).

[9] Halls, J. J. M., Walsh, C. A., Greenham, N. C., Marseglia, E. A., Friend, R. H., Morattl, S. C., and Holmes, A. B. *Nature* **376**, 498–500 (1995).

[10] Schilinsky, P., Waldauf, C., and Brabec, C. J. *Applied Physics Letters* **81**, 3885–3887 (2002).

[11] Li, G., Shrotriya, V., Huang, J., Yao, Y., Moriarty, T., Emery, K., and Yang, Y. *Nature Materials* **4**, 864–868 (2005).

[12] You, J., Dou, L., Yoshimura, K., Kato, T., Ohya, K., Moriarty, T., Emery, K., Chen, C.-C., Gao, J., Li, G., and Yang, Y. *Nature Communications* **4**, 1446 (2013).

[13] Chen, C.-C., Chang, W.-H., Yoshimura, K., Ohya, K., You, J., Gao, J., Hong, Z., and Yang, Y. *Advanced Materials* **26**, 5670–5677 (2014).

[14] Braun, C. L. *The Journal of Chemical Physics* **80**, 4157–4161 (1984).

[15] Shuttle, C. G., O'Regan, B., Ballantyne, A. M., Nelson, J., Bradley, D. D. C., and Durrant, J. R. *Phys. Rev. B* **78**, 113201 (2008).

[16] Bässler, H. *physica status solidi (b)* **175**, 15–56 (1993).

[17] Shuttle, C. G., Hamilton, R., ORegan, B. C., Nelson, J., and Durrant, J. R. *Proceedings of the National Academy of Sciences* **107**, 16448–16452 (2010).

[18] Roland, S., Schubert, M., Collins, B. A., Kurpiers, J., Chen, Z., Facchetti, A., Ade, H., and Neher, D. *The Journal of Physical Chemistry Letters* **5**, 2815–2822 (2014).

[19] Marsh, R. A., Hodgkiss, J. M., and Friend, R. H. *Advanced Materials* **22**, 3672–3676 (2010).

[20] Jamieson, F. C., Agostinelli, T., Azimi, H., Nelson, J., and Durrant, J. R. *The Journal of Physical Chemistry Letters* **1**, 3306–3310 (2010).

[21] Howard, I. A., Mauer, R., Meister, M., and Laquai, F. *Journal of the American Chemical Society* **132**, 14866–14876 (2010). PMID: 20923187.

[22] Guo, J., Ohkita, H., Yokoya, S., Benten, H., and Ito, S. *Journal of the American Chemical Society* **132**, 9631–9637 (2010). PMID: 20575519.

[23] Mihailetchi, V. D., Koster, L. J. A., Hummelen, J. C., and Blom, P. W. M. *Phys. Rev. Lett.* **93**, 216601 (2004).

[24] Mihailetchi, V. D., Xie, H., de Boer, B., Popescu, L. M., Hummelen, J. C., Blom, P. W. M., and Koster, L. J. A. *Applied Physics Letters* **89**, 012107 (2006).

[25] Mihailetchi, V., Xie, H., de Boer, B., Koster, L., and Blom, P. *Advanced Functional Materials* **16**, 699–708 (2006).

[26] Foertig, A., Kniepert, J., Gluecker, M., Brenner, T., Dyakonov, V., Neher, D., and Deibel, C. *Advanced Functional Materials* **24**, 1306–1311 (2014).

[27] Mauer, R., Howard, I. A., and Laquai, F. *The Journal of Physical Chemistry Letters* **1**, 3500–3505 (2010).

[28] Foster, S., Deledalle, F., Mitani, A., Kimura, T., Kim, K.-B., Okachi, T., Kirchartz, T., Oguma, J., Miyake, K., Durrant, J. R., Doi, S., and Nelson, J. *Advanced Energy Materials* **4**, 1400311 (2014).

[29] Mauer, R., Kastler, M., and Laquai, F. *Advanced Functional Materials* **20**, 2085–2092 (2010).

[30] He, Z., Zhong, C., Su, S., Xu, M., Wu, H., and Cao, Y. *Nature Photonics* **6**, 591–595 (2012).

[31] Chen, J.-D., Cui, C., Li, Y.-Q., Zhou, L., Ou, Q.-D., Li, C., Li, Y., and Tang, J.-X. *Advanced Materials* **27**, 1132–1132 (2015).

[32] Peierls, R. E. *Quantum Theory of Solids*. Clarendon Press, Oxford, (1955).

[33] Roncali, J. *Macromolecular Rapid Communications* **28**, 1761–1775 (2007).

[34] Pope, M. and Swenberg, C. E. *Electronic Processes in Organic Crystals and Polymers*. Oxford University Press, second edition, (1999).

[35] Geoghegan, M. and Hadziioannou, G. *Polymer Electronics*. Oxford University Press, (2013).

[36] Deibel, C. and Dyakonov, V. *Rep. Prog. Phys.* **73**, 096401 (2010).

[37] Shaw, P. E., Ruseckas, A., and Samuel, I. D. W. *Advanced Materials* **20**, 3516–3520 (2008).

[38] Lüer, L., Egelhaaf, H.-J., Oelkrug, D., Cerullo, G., Lanzani, G., Huisman, B.-H., and de Leeuw, D. *Organic Electronics* **5**, 83 – 89 (2004).

[39] Stübinger, T. and Brütting, W. *Journal of Applied Physics* **90**, 3632–3641 (2001).

[40] Kroeze, J. E., Savenije, T. J., Vermeulen, M. J. W., and Warman, J. M. *The Journal of Physical Chemistry B* **107**, 7696–7705 (2003).

[41] Etzold, F., Howard, I. A., Mauer, R., Meister, M., Kim, T.-D., Lee, K.-S., Baek, N. S., and Laquai, F. *Journal of the American Chemical Society* **133**, 9469–9479 (2011).

[42] Grancini, G., Maiuri, M., Fazzi, D., Petrozza, A., Egelhaaf, H.-J., Brida, D., Cerullo, G., and Lanzani, G. *Nature Materials* **12**, 29 (2012).

[43] Lee, J., Vandewal, K., Yost, S. R., Bahlke, M. E., Goris, L., Baldo, M. A., Manca, J. V., and Voorhis, T. V. *Journal of the American Chemical Society* **132**, 11878–11880 (2010).

[44] Tvingstedt, K., Vandewal, K., Gadisa, A., Zhang, F., Manca, J., and Inganäs, O. *Journal of the American Chemical Society* **131**, 11819–11824 (2009).

[45] Tvingstedt, K., Vandewal, K., Zhang, F., and Inganäs, O. *The Journal of Physical Chemistry C* **114**, 21824–21832 (2010).

[46] Sariciftci, N. S., Smilowitz, L., Heeger, A. J., and Wudl, F. *Science* **258**, 1474–1476 (1992).

[47] Scharber, M. C., Schultz, N. A., Sariciftci, N. S., and Brabec, C. J. *Phys. Rev. B* **67**, 085202 (2003).

[48] Behrends, J., Sperlich, A., Schnegg, A., Biskup, T., Teutloff, C., Lips, K., Dyakonov, V., and Bittl, R. *Phys. Rev. B* **85**, 125206 (2012).

[49] Kraffert, F., Steyrleuthner, R., Albrecht, S., Neher, D., Scharber, M. C., Bittl, R., and Behrends, J. *The Journal of Physical Chemistry C* **118**, 28482–28493 (2014).

[50] Veldman, D., Ipek, O., Meskers, S. C. J., Sweelssen, J., Koetse, M. M., Veenstra, S. C., Kroon, J. M., Bavel, S. S. v., Loos, J., and Janssen, R. A. J. *Journal of the American Chemical Society* **130**, 7721–7735 (2008).

[51] Arkhipov, V. I., Heremans, P., and Bässler, H. *Applied Physics Letters* **82**, 4605–4607 (2003).

[52] Shoaee, S., Subramaniyan, S., Xin, H., Keiderling, C., Tuladhar, P. S., Jamieson, F., Jenekhe, S. A., and Durrant, J. R. *Advanced Functional Materials* **23**, 3286–3298 (2013).

[53] Clarke, T. M. and Durrant, J. R. *Chemical Reviews* **110**, 6736–6767 (2010).

[54] Onsager, L. *Physical Review* **54** (1938).

[55] Hallermann, M., Haneder, S., and Da Como, E. *Applied Physics Letters* **93** (2008).

[56] Veldman, D., Meskers, S. C. J., and Janssen, R. A. J. *Advanced Functional Materials* **19**, 1939–1948 (2009).

[57] Kern, J., Schwab, S., Deibel, C., and Dyakonov, V. *physica status solidi (RRL) Rapid Research Letters* **5**, 364–366 (2011).

[58] Deibel, C., Strobel, T., and Dyakonov, V. *Advanced Materials* **22**, 4097–4111 (2010).

[59] Park, S. H., Roy, A., Beaupre, S., Cho, S., Coates, N., Moon, J. S., Moses, D., Leclerc, M., Lee, K., and Heeger, A. J. *Nature Photonics* **3**, 297–303 (2009).

[60] van Hal, P. A., Janssen, R. A. J., Lanzani, G., Cerullo, G., Zavelani-Rossi, M., and De Silvestri, S. *Phys. Rev. B* **64**, 075206 (2001).

[61] Gulbinas, V., Hertel, D., Yartsev, A., and Sundström, V. *Phys. Rev. B* **76**, 235203 (2007).

[62] Bakulin, A. A., Martyanov, D. S., Paraschuk, D. Y., Pshenichnikov, M. S., and van Loosdrecht, P. H. M. *The Journal of Physical Chemistry B* **112**, 13730–13737 (2008).

[63] Bernardo, B., Cheyns, D., Verreet, B., Schaller, R. D., Rand, B. P., and Giebink, N. C. *Nature Communications* (2014).

[64] Bakulin, A. A., Rao, A., Pavelyev, V. G., van Loosdrecht, P. H. M., Pshenichnikov, M. S., Niedzialek, D., Cornil, J., Beljonne, D., and Friend, R. H. *Science* **335**, 1340–1344 (2012).

[65] Tamura, H. and Burghardt, I. *Journal of the American Chemical Society* **135**, 16364–16367 (2013).

[66] Ohkita, H., Cook, S., Astuti, Y., Duffy, W., Tierney, S., Zhang, W., Heeney, M., McCulloch, I., Nelson, J., Bradley, D. D. C., and Durrant, J. R. *Journal of the American Chemical Society* **130**, 3030–3042 (2008).

[67] Shoaee, S., Clarke, T. M., Huang, C., Barlow, S., Marder, S. R., Heeney, M., McCulloch, I., and Durrant, J. R. *Journal of the American Chemical Society* **132**, 12919–12926 (2010).

[68] Gelinas, S., Rao, A., Kumar, A., Smith, S. L., Chin, A. W., Clark, J., van der Poll, T. S., Bazan, G. C., and Friend, R. H. *Science* **343**, 512–516 (2014).

[69] Jailaubekov, A. E., Willard, A. P., Tritsch, J. R., Chan, W.-L., Sai, N., Gearba, R., Kaake, L. G., Williams, K. J., Leung, K., Rossky, P. J., and Zhu, X.-Y. *Nature Materials* **12**, 66–73 (2013).

[70] Vandewal, K., Albrecht, S., Hoke, E. T., Graham, K. R., Widmer, J., Douglas, J. D., Schubert, M., Mateker, W. R., Bloking, J. T., Burkhard, G. F., Sellinger, A., Frechet, J. M. J., Amassian, A., Riede, M. K., McGehee, M. D., Neher, D., and Salleo, A. *Nature Materials* (2014).

[71] Albrecht, S., Vandewal, K., Tumbleston, J. R., Fischer, F. S. U., Douglas, J. D., Frechet, J. M. J., Ludwigs, S., Ade, H., Salleo, A., and Neher, D. *Advanced Materials* **26**, 2533–2539 (2014).

[72] van der Hofstad, T. G. J., Di Nuzzo, D., van den Berg, M., Janssen, R. A. J., and Meskers, S. C. J. *Advanced Energy Materials* **2**, 1095–1099 (2012).

[73] Shockley, W. and Read, W. T. *Phys. Rev.* **87**, 835–842 (1952).

[74] Hall, R. N. *Phys. Rev.* **87**, 387–387 (1952).

[75] Kuik, M., Nicolai, H. T., Lenes, M., Wetzelaer, G.-J. A. H., Lu, M., and Blom, P. W. M. *Applied Physics Letters* **98** (2011).

[76] Mandoc, M. M., Kooistra, F. B., Hummelen, J. C., de Boer, B., and Blom, P. W. M. *Applied Physics Letters* **91** (2007).

[77] Langevin, P. *Annales de chimie et de physique* **28**, 433–530 (1903).

[78] Pivrikas, A., Juška, G., Mozer, A. J., Scharber, M., Arlauskas, K., Sariciftci, N. S., Stubb, H., and Österbacka, R. *Phys. Rev. Lett.* **94**, 176806 (2005).

[79] Juska, G., Arlauskas, K., Stuchlik, J., and Österbacka, R. *Journal of Non-Crystalline Solids* **352**, 1167 – 1171 (2006).

[80] Deibel, C., Baumann, A., and Dyakonov, V. *Applied Physics Letters* **93** (2008).

[81] Zalar, P., Kuik, M., Ran, N. A., Love, J. A., and Nguyen, T.-Q. *Advanced Energy Materials* **4** (2014).

[82] Deibel, C., Wagenpfahl, A., and Dyakonov, V. *Phys. Rev. B* **80**, 075203 (2009).

[83] Bartesaghi, D., Perez, I., Kniepert, J., Roland, S., Turbiez, M., Neher, D., and Koster, L. J. A. *Nature Communications* **6** (2015).

[84] Koster, L. J. A., Mihailetchi, V. D., and Blom, P. W. M. *Applied Physics Letters* **88** (2006).

[85] Adriaenssens, G. and Arkhipov, V. *Solid State Communications* **103**, 541 – 543 (1997).

[86] McMahon, D. P., Cheung, D. L., and Troisi, A. *The Journal of Physical Chemistry Letters* **2**, 2737–2741 (2011).

[87] Shuttle, C. G., ORegan, B., Ballantyne, A. M., Nelson, J., Bradley, D. D. C., de Mello, J., and Durrant, J. R. *Applied Physics Letters* **92** (2008).

[88] Juska, G., Genevicius, K., Nekrasas, N., Sliauzys, G., and Dennler, G. *Applied Physics Letters* **93** (2008).

[89] Kirchartz, T. and Nelson, J. *Phys. Rev. B* **86**, 165201 (2012).

[90] Deledalle, F., Shakya Tuladhar, P., Nelson, J., Durrant, J. R., and Kirchartz, T. *The Journal of Physical Chemistry C* **118**, 8837–8842 (2014).

[91] Miller, A. and Abrahams, E. *Phys. Rev.* **120**, 745–755 (1960).

[92] Tanase, C., Meijer, E. J., Blom, P. W. M., and de Leeuw, D. M. *Phys. Rev. Lett.* **91**, 216601 (2003).

[93] Shuttle, C. G., Hamilton, R., Nelson, J., O'Regan, B. C., and Durrant, J. R. *Advanced Functional Materials* **20**, 698–702 (2010).

[94] Pasveer, W. F., Cottaar, J., Tanase, C., Coehoorn, R., Bobbert, P. A., Blom, P. W. M., de Leeuw, D. M., and Michels, M. A. J. *Phys. Rev. Lett.* **94**, 206601 (2005).

[95] Nenashev, A. V., Oelerich, J. O., and Baranovskii, S. D. *Journal of Physics: Condensed Matter* **27**, 093201 (2015).

[96] Tiedje, T. and Rose, A. *Solid State Communications* **37**, 49 – 52 (1981).

[97] Le Comber, P. G. and Spear, W. E. *Phys. Rev. Lett.* **25**, 509–511 (1970).

[98] Nelson, J. *Phys. Rev. B* **67**, 155209 (2003).

[99] Lampert, M. A. *Phys. Rev.* **103**, 1648–1656 (1956).

[100] Mark, P. and Helfrich, W. *Journal of Applied Physics* **33**, 205–215 (1962).

[101] Mauger, S. A., Chang, L., Friedrich, S., Rochester, C. W., Huang, D. M., Wang, P., and Moul, A. J. *Advanced Functional Materials* **23**, 1935–1946 (2013).

[102] Murgatroyd, P. N. *J. Phys. D: Appl. Phys.* **3**, 151 (1970).

[103] Schwoerer, M. and Wolf, H. C. *Organische Molekulare Festkörper*. Wiley-VCH Verlag, (2005).

[104] Fowler, R. H. and Nordheim, L. *Proceedings of the Royal Society of London A* **119**, 173–181 (1928).

[105] Scott, J. and Malliaras, G. G. *Chemical Physics Letters* **299**, 115 – 119 (1999).

[106] Arkhipov, V. I., Emelianova, E. V., Tak, Y. H., and Bässler, H. *Journal of Applied Physics* **84**, 848–856 (1998).

[107] Wolf, U. and Bässler, H. *Applied Physics Letters* **74**, 3848–3850 (1999).

[108] Wolf, U., Arkhipov, V. I., and Bässler, H. *Phys. Rev. B* **59**, 7507–7513 (1999).

[109] Blakesley, J. C. and Greenham, N. C. *Journal of Applied Physics* **106** (2009).

[110] Koster, L. J. A., Smits, E. C. P., Mihailetchi, V. D., and Blom, P. W. M. *Phys. Rev. B* **72**, 085205 (2005).

[111] Gummel, H. *IEEE Transactions on Electron Devices* **11**, 455–465 (1964).

[112] Bange, S. *Transient Optical and Electrical Effects in Polymeric Semiconductors*. PhD thesis, University of Potsdam, (2009).

[113] Prosa, T. J., Winokur, M. J., Moulton, J., Smith, P., and Heeger, A. J. *Macromolecules* **25**, 4364–4372 (1992).

[114] Yang, X., Loos, J., Veenstra, S. C., Verhees, W. J. H., Wienk, M. M., Kroon, J. M., Michels, M. A. J., and Janssen, R. A. J. *Nano Letters* **5**, 579–583 (2005).

[115] Verploegen, E., Mondal, R., Bettinger, C. J., Sok, S., Toney, M. F., and Bao, Z. *Advanced Functional Materials* **20**, 3519–3529 (2010).

[116] Savenije, T., Kroeze, J., Yang, X., and Loos, J. *Advanced Functional Materials* **15**, 1260–1266 (2005).

[117] Campoy-Quiles, M., Ferenczi, T., Agostinelli, T., Etchegoin, P. G., Kim, Y., Anthopoulos, T. D., Stavrinou, P. N., Bradley, D. D. C., and Nelson, J. *Nature Materials* **7**, 158–164 (2008).

[118] Turner, S. T., Pingel, P., Steyrleuthner, R., Crossland, E. J. W., Ludwigs, S., and Neher, D. *Advanced Functional Materials* **21**, 4640–4652 (2011).

[119] Kim, Y., Cook, S., Tuladhar, S. M., Choulis, S. A., Nelson, J., Durrant, J. R., Bradley, D. D. C., Giles, M., McCulloch, I., Ha, C.-S., and Ree, M. *Nature Materials* **5**, 197–203 (2006).

[120] Liang, Y., Xu, Z., Xia, J., Tsai, S.-T., Wu, Y., Li, G., Ray, C., and Yu, L. *Advanced Materials* **22**, E135–E138 (2010).

[121] Xu, T. and Yu, L. *Materials Today* **17**, 11 – 15 (2014).

[122] Tremel, K. and Ludwigs, S. In *P3HT Revisited From Molecular Scale to Solar Cell Devices,* Ludwigs, S., editor, volume 265 of *Advances in Polymer Science*, 39–82. Springer Berlin Heidelberg (2014).

[123] Collins, B. A., Li, Z., Tumbleston, J. R., Gann, E., McNeill, C. R., and Ade, H. *Advanced Energy Materials* **3**, 65–74 (2013).

[124] Hedley, G. J., Ward, A. J., Alekseev, A., Howells, C. T., Martins, E. R., Serrano, L. A., Cooke, G., Ruseckas, A., and W., S. I. D. *Nature Communications* **4** (2013).

[125] Keivanidis, P. E., Clarke, T. M., Lilliu, S., Agostinelli, T., Macdonald, J. E., Durrant, J. R., Bradley, D. D. C., and Nelson, J. *The Journal of Physical Chemistry Letters* **1**, 734–738 (2010).

[126] Popovic, Z. D. *The Journal of Chemical Physics* **78**, 1552–1558 (1983).

[127] Popovic, Z. D. *Chemical Physics Letters* **100**, 227 – 229 (1983).

[128] Esteghamatian, M., Popovic, Z. D., and Xu, G. *The Journal of Physical Chemistry* **100**, 13716–13719 (1996).

[129] Hertel, D., Soh, E. V., Bässler, H., and Rothberg, L. J. *Chemical Physics Letters* **361**, 99 – 105 (2002).

[130] Offermans, T., Meskers, S. C. J., and Janssen, R. A. J. *Journal of Applied Physics* **100** (2006).

[131] Kniepert, J., Schubert, M., Blakesley, J. C., and Neher, D. *The Journal of Physical Chemistry Letters* **2**, 700–705 (2011).

[132] Mingebach, M., Walter, S., Dyakonov, V., and Deibel, C. *Applied Physics Letters* **100** (2012).

[133] Albrecht, S., Schindler, W., Kurpiers, J., Kniepert, J., Blakesley, J. C., Dumsch, I., Allard, S., Fostiropoulos, K., Scherf, U., and Neher, D. *The Journal of Physical Chemistry Letters* **3**, 640–645 (2012).

[134] Gluecker, M., Foertig, A., Dyakonov, V., and Deibel, C. *physica status solidi (RRL) Rapid Research Letters* **6**, 337–339 (2012).

[135] Albrecht, S., Janietz, S., Schindler, W., Frisch, J., Kurpiers, J., Kniepert, J., Inal, S., Pingel, P., Fostiropoulos, K., Koch, N., and Neher, D. *Journal of the American Chemical Society* **134**, 14932–14944 (2012).

[136] Kniepert, J., Lange, I., van der Kaap, N. J., Koster, L. J. A., and Neher, D. *Advanced Energy Materials* **4** (2014).

[137] Yang, B., Yuan, Y., and Huang, J. *The Journal of Physical Chemistry C* **118**, 5196–5202 (2014).

[138] Albrecht, S., Tumbleston, J. R., Janietz, S., Dumsch, I., Allard, S., Scherf, U., Ade, H., and Neher, D. *The Journal of Physical Chemistry Letters* **5**, 1131–1138 (2014).

[139] Zusan, A., Vandewal, K., Allendorf, B., Hansen, N. H., Pflaum, J., Salleo, A., Dyakonov, V., and Deibel, C. *Advanced Energy Materials* **4** (2014).

[140] Proctor, C. M., Albrecht, S., Kuik, M., Neher, D., and Nguyen, T.-Q. *Advanced Energy Materials* **4** (2014).

[141] Gehrig, D. W., Roland, S., Howard, I. A., Kamm, V., Mangold, H., Neher, D., and Laquai, F. *The Journal of Physical Chemistry C* **118**, 20077–20085 (2014).

[142] Li, W., Albrecht, S., Yang, L., Roland, S., Tumbleston, J. R., McAfee, T., Yan, L., Kelly, M. A., Ade, H., Neher, D., and You, W. *Journal of the American Chemical Society* **136**, 15566–15576 (2014).

[143] Zusan, A., Gieseking, B., Zerson, M., Dyakonov, V., Magerle, R., and Deibel, C. *Scientific Reports* **5** (2015).

[144] Kniepert, J., Lange, I., Heidbrink, J., Kurpiers, J., Brenner, T. J. K., Koster, L. J. A., and Neher, D. *The Journal of Physical Chemistry C* **119**, 8310–8320 (2015).

[145] Juska, G., Arlauskas, K., Vilinas, M., and Kocka, J. *Phys. Rev. Lett.* **84**, 4946–4949 (2000).

[146] Seifter, J., Sun, Y., and Heeger, A. J. *Advanced Materials* **26**, 2486–2493 (2014).

[147] Cowan, S. R., Street, R. A., Cho, S., and Heeger, A. J. *Phys. Rev. B* **83**, 035205 (2011).

[148] Po, R., Maggini, M., and Camaioni, N. *The Journal of Physical Chemistry C* **114**, 695–706 (2010).

[149] Dang, M. T., Hirsch, L., and Wantz, G. *Advanced Materials* **23**, 3597–3602 (2011).

[150] Nguyen, L., Hoppe, H., Erb, T., Günes, S., Gobsch, G., and Sariciftci, N. *Advanced Functional Materials* **17**, 1071–1078 (2007).

[151] Agostinelli, T., Lilliu, S., Labram, J. G., Campoy-Quiles, M., Hampton, M., Pires, E., Rawle, J., Bikondoa, O., Bradley, D. D. C., Anthopoulos, T. D., Nelson, J., and Macdonald, J. E. *Advanced Functional Materials* **21**, 1701–1708 (2011).

[152] Kim, Y., Choulis, S. A., Nelson, J., Bradley, D. D. C., Cook, S., and Durrant, J. R. *Applied Physics Letters* **86** (2005).

[153] Moule, A. and Meerholz, K. *Advanced Materials* **20**, 240–245 (2008).

[154] Hammond, M. R., Kline, R. J., Herzing, A. A., Richter, L. J., Germack, D. S., Ro, H.-W., Soles, C. L., Fischer, D. A., Xu, T., Yu, L., Toney, M. F., and DeLongchamp, D. M. *ACS Nano* **5**, 8248–8257 (2011).

[155] Chen, W., Xu, T., He, F., Wang, W., Wang, C., Strzalka, J., Liu, Y., Wen, J., Miller, D. J., Chen, J., Hong, K., Yu, L., and Darling, S. B. *Nano Letters* **11**, 3707–3713 (2011).

[156] Liu, F., Zhao, W., Tumbleston, J. R., Wang, C., Gu, Y., Wang, D., Briseno, A. L., Ade, H., and Russell, T. P. *Advanced Energy Materials* **4** (2014).

[157] Li, Z., Lakhwani, G., Greenham, N. C., and McNeill, C. R. *Journal of Applied Physics* **114** (2013).

[158] Clarke, T. M., Ballantyne, A. M., Nelson, J., Bradley, D. D. C., and Durrant, J. R. *Advanced Functional Materials* **18**, 4029–4035 (2008).

[159] Hamilton, R., Shuttle, C. G., ORegan, B., Hammant, T. C., Nelson, J., and Durrant, J. R. *The Journal of Physical Chemistry Letters* **1**, 1432–1436 (2010).

[160] Deibel, C., Strobel, T., and Dyakonov, V. *Phys. Rev. Lett.* **103**, 036402 (2009).

[161] Brenner, T. J. K., Li, Z., and McNeill, C. R. *The Journal of Physical Chemistry C* **115**, 22075–22083 (2011).

[162] Jamieson, F. C., Domingo, E. B., McCarthy-Ward, T., Heeney, M., Stingelin, N., and Durrant, J. R. *Chem. Sci.* **3**, 485–492 (2012).

[163] Savoie, B. M., Rao, A., Bakulin, A. A., Gelinas, S., Movaghar, B., Friend, R. H., Marks, T. J., and Ratner, M. A. *Journal of the American Chemical Society* **136**, 2876–2884 (2014).

[164] Szarko, J. M., Rolczynski, B. S., Lou, S. J., Xu, T., Strzalka, J., Marks, T. J., Yu, L., and Chen, L. X. *Advanced Functional Materials* **24**, 10–26 (2014).

[165] Huang, Y.-S., Westenhoff, S., Avilov, I., Sreearunothai, P., Hodgkiss, J. M., Deleener, C., Friend, R. H., and Beljonne, D. *Nature Materials* **7**, 483–489 (2008).

[166] Mauer, R., Howard, I. A., and Laquai, F. *The Journal of Physical Chemistry Letters* **2**, 1736–1741 (2011).

[167] Maurano, A., Hamilton, R., Shuttle, C. G., Ballantyne, A. M., Nelson, J., ORegan, B., Zhang, W., McCulloch, I., Azimi, H., Morana, M., Brabec, C. J., and Durrant, J. R. *Advanced Materials* **22**, 4987–4992 (2010).

[168] Rauh, D., Deibel, C., and Dyakonov, V. *Advanced Functional Materials* **22**, 3371–3377 (2012).

[169] Cowan, S. R., Roy, A., and Heeger, A. J. *Phys. Rev. B* **82**, 245207 (2010).

[170] Shuttle, C. G., Maurano, A., Hamilton, R., ORegan, B., de Mello, J. C., and Durrant, J. R. *Applied Physics Letters* **93**(18) (2008).

[171] Blakesley, J. C., Castro, F. A., Kylberg, W., Dibb, G. F., Arantes, C., Valaski, R., Cremona, M., Kim, J. S., and Kim, J.-S. *Organic Electronics* **15**, 1263 – 1272 (2014).

[172] Bange, S., Kuksov, A., Neher, D., Vollmer, A., Koch, N., Ludemann, A., and Heun, S. *Journal of Applied Physics* **104** (2008).

[173] Mozer, A. J., Sariciftci, N. S., Pivrikas, A., Österbacka, R., Juska, G., Brassat, L., and Bässler, H. *Phys. Rev. B* **71**, 035214 (2005).

[174] Braun, S., Salaneck, W. R., and Fahlman, M. *Advanced Materials* **21**, 1450–1472 (2009).

[175] Lange, I., Blakesley, J. C., Frisch, J., Vollmer, A., Koch, N., and Neher, D. *Phys. Rev. Lett.* **106**, 216402 (2011).

[176] Orenstein, J. and Kastner, M. *Phys. Rev. Lett.* **46**, 1421–1424 (1981).

[177] Scher, H. and Montroll, E. W. *Phys. Rev. B* **12**, 2455–2477 (1975).

[178] Gu, C., Chen, Y., Zhang, Z., Xue, S., Sun, S., Zhong, C., Zhang, H., Lv, Y., Li, F., Huang, F., and Ma, Y. *Advanced Energy Materials* **4** (2014).

[179] Clarke, T. M., Jamieson, F. C., and Durrant, J. R. *The Journal of Physical Chemistry C* **113**, 20934–20941 (2009).

[180] Vissenberg, M. C. J. M. and Matters, M. *Phys. Rev. B* **57**, 12964–12967 (1998).

[181] Brondijk, J. J., Maddalena, F., Asadi, K., van Leijen, H. J., Heeney, M., Blom, P. W. M., and de Leeuw, D. M. *physica status solidi (b)* **249**, 138–141 (2012).

[182] Arkhipov, V. I., Heremans, P., Emelianova, E. V., and Bässler, H. *Phys. Rev. B* **71**, 045214 (2005).

[183] Arkhipov, V. I., Emelianova, E. V., Heremans, P., and Bässler, H. *Phys. Rev. B* **72**, 235202 (2005).

[184] Jiang, X., Harima, Y., Yamashita, K., Tada, Y., Ohshita, J., and Kunai, A. *Chemical Physics Letters* **364**, 616 – 620 (2002).

[185] Pingel, P., Schwarzl, R., and Neher, D. *Applied Physics Letters* **100** (2012).

[186] Pingel, P. and Neher, D. *Phys. Rev. B* **87**, 115209 (2013).

[187] van Bavel, S., Sourty, E., de With, G., Frolic, K., and Loos, J. *Macromolecules* **42**, 7396–7403 (2009).

[188] Goodman, A. M. and Rose, A. *Journal of Applied Physics* **42**, 2823–2830 (1971).

[189] Mihailetchi, V. D., Wildeman, J., and Blom, P. W. M. *Phys. Rev. Lett.* **94**, 126602 (2005).

[190] Coehoorn, R., Pasveer, W. F., Bobbert, P. A., and Michels, M. A. J. *Phys. Rev. B* **72**, 155206 (2005).

[191] Tessler, N., Preezant, Y., Rappaport, N., and Roichman, Y. *Advanced Materials* **21**, 2741–2761 (2009).

[192] Köhler, A. and Bässler, H. *Electronic Processes in Organic Semiconductors*. Wiley-VCH, (2015).

[193] Lange, I., Kniepert, J., Pingel, P., Dumsch, I., Allard, S., Janietz, S., Scherf, U., and Neher, D. *The Journal of Physical Chemistry Letters* **4**, 3865–3871 (2013).

[194] Kirchartz, T., Pieters, B. E., Taretto, K., and Rau, U. *Phys. Rev. B* **80**, 035334 (2009).

[195] Lane, P. A., deMello, J. C., Fletcher, R. B., and Bernius, M. *Applied Physics Letters* **83**, 3611–3613 (2003).

[196] Brewer, P. J., Lane, P. A., Huang, J., deMello, A. J., Bradley, D. D. C., and deMello, J. C. *Phys. Rev. B* **71**, 205209 (2005).

[197] Murata, K., Cina, S., and Greenham, N. C. *Applied Physics Letters* **79**, 1193–1195 (2001).

[198] Yang, W. S., Noh, J. H., Jeon, N. J., Kim, Y. C., Ryu, S., Seo, J., and Seok, S. I. *Science* **348**, 1234–1237 (2015).

[199] Paulke, A., Stranks, S. D., Kniepert, J., Schön, N., Snaith, H. J., Neher, D., and Brenner, T. J. K. *in preparation* .

Appendix

A.1 TDCF set-up and specifications

In TDCF, a short laser pulse in combination with a subsequent voltage pulse is used to measure generation and recombination of charge carriers in organic solar cells. During the course of this thesis, the TDCF set-up has been continuously improved. The majority of experiments in this thesis has been performed with the set-up outlined in Figure A.1. The pulsed excitation of the sample was provided by a diode

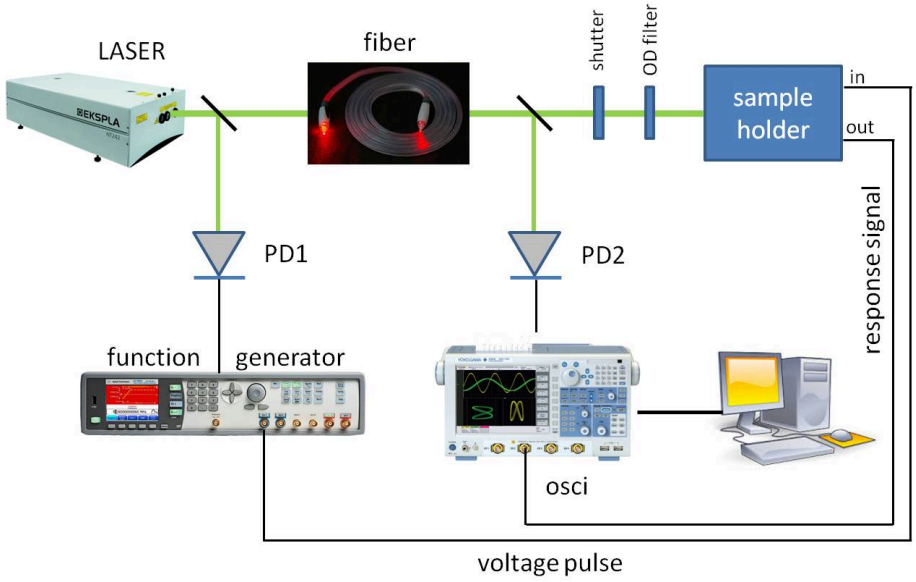

Figure A.1: Schematic presentation of the TDCF set-up. For a detailed description see text.

pumped, Q-switched Nd:YAG laser (NT242, EKSPLA). The pulse width was 5.5 ns and repetition rate was 500 Hz. The output wavelength of the laser could be tuned in between 400 - 680 nm and 750 - 2000 nm via an optical parametric oscillator (OPO). The intensity of the laser beam (green line) at the sample was adjusted with optical density (OD) filters.
The voltage pulse (V_{pre}, V_{coll}) was provided by a function generator (Agilent 81150A) with a very fast pulse rise time (2.5 ns) and low internal jitter (500 ps). To avoid the jitter of the laser electronics (10 ns) the function generator was directly triggered by the laser pulse via a fast photodiode (PD1, rise time 8 ns) positioned close to the laser output. To compensate for the rather long electronic processing time of the Agilent (480 ns) the laser pulses were optically delayed with a multimode fiber (LEONI, length 85 m). A second fast photodiode (PD2, rise time 300 ps) was placed after the fiber to trigger the oscilloscope (Yokogawa DL9140), which recorded the response current signal via a 50 Ω resistor in series with the sample. The reference dark measurement was taken by blocking the laser beam with a mechanical shutter.

A.2 Sample Preparation and Structure

The sample structures prepared in this work are shown in Figure A.2. All of the structures were prepared on 2.5 cm×2.5 cm glass substrates in part covered with transparent indium tin oxide (ITO) bottom electrodes. For the TDCF samples/solar cells and the hole-only devices, two different ITO structures were used as indicated below. All substrates were cleaned by ultrasonification in the following solutions for 15 min each: acetone, 3% Hellmanex solution (alkaline cleaning concentrate), de-ionized water and isopropanol. The substrates were rinsed with de-ionized water 10 times after the acetone and Hellmanex solution steps. Subsequently, the substrates were dried with nitrogen. To remove organic residues and increase the wettability of the surface, oxygen plasma treatment of the substrates was performed for 2 min at 200 W in a Technics Plasma 200-G system. Then a 60 nm layer of poly(3,4-ethylendioxythiophene):polystyrolsulfonate (PEDOT:PSS, Clevios AI 4083) was solution cast on to the substrates and subsequently heated at 180°C for 10 min under inert conditions. For the electron-only devices an Al bottom electrode (12 mm×25 mm) was evaporated on top of the PEDOT:PSS layer.
The active layer films (polymer/fullerene blends) were spin cast on to the bottom electrodes as detailed below. Finally, top electrodes were thermally evaporated through shadow masks, defining the active area (1 mm^2 for the TDCF samples/solar cells and 5 mm^2 for the single carrier devices). TDCF samples/solar cells were encapsulated with epoxy resin and a glass lid prior to air exposure.

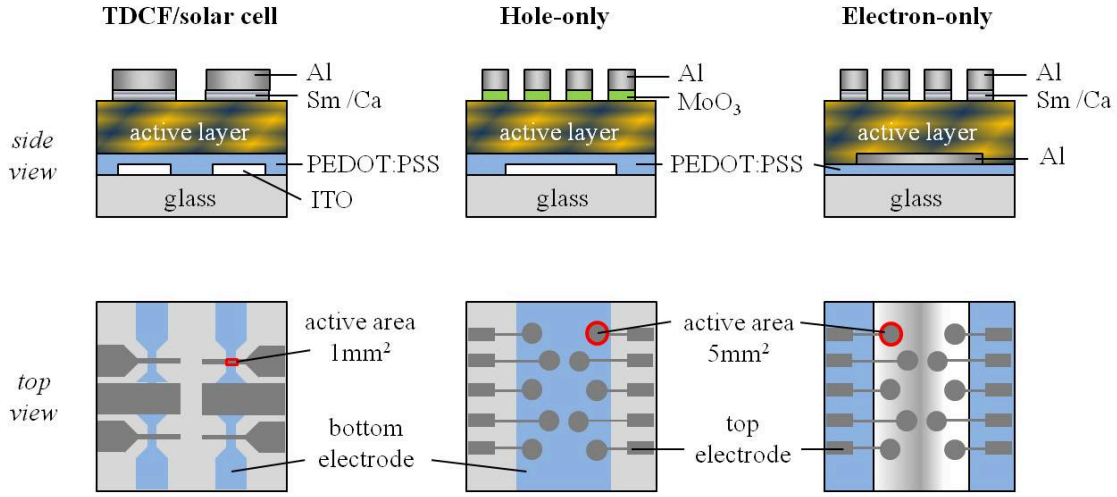

Figure A.2: Schematic of sample structures prepared for TDCF measurements (solar cells) and single carrier devices.

P3HT:PCBM blends

P3HT (Sepiolid 200, purchased from BASF) and PC[70]BM (purchased from Solenne) were separately solved in chloroform (CF), then mixed to a 1:1 (by weight) solution

with a concentration of 25 gL^{-1} and subsequently spin coated at 1000 rpm, yielding an active layer thickness of 200 nm. Devices referred to as 'annealed' were heated at 150°C for 15 min directly after spin coating. Top electrodes for solar cells and electron-only devices consisted of 20 nm Sm and 100 nm Al. Top electrodes for hole-only devices consisted of 20 nm MoO_3 and 100 nm Al. Different layer thicknesses for SCLC measurements were obtained by varying the concentration of the solution.

PTB7:PCBM blends

PTB7 (purchased from 1-material) and PC[70]BM (purchased from Solenne) were separately solved in chlorobenzene (CB), then mixed to a 1:1.5 (by weight) solution with a concentration of 25 gL^{-1} and subsequently spin coated at 1000 rpm, yielding an active layer thickness of 100 nm. In the case of devices referred to as 'with DIO' 3 vol-% 1,8-diiodooctane (DIO) were used as cosolvent in the CB solution. Top electrodes for solar cells and electron-only devices consisted of 5 nm Ca and 80 nm Al.

A.3 Derivation of Equation (4.5)

In the TDCF experiment, (injected) dark charge is not recognized as part of the collected charge as the dark current transient is subtracted from the transient under illumination. However, the dark charge carriers take part in bimolecular recombination with the photogenerated charge carriers and have to be taken into account when analyzing the recombination dynamics with delay dependent TDCF measurements. In the following the derivation of the iterative model including Q_{dark} (Equation 4.5 will be shown.
Under steady state conditions in the dark, injection, extraction and bimolecular recombination (BMR) of charge carriers are in equilibrium:

$$\frac{dn_D}{dt} = -kn_D^2 + (j_{D,in} - j_{D,out})/ed = 0, \tag{A.1}$$

where n_D is the dark carrier density (assuming equal hole and electron densities), k is the BMR coefficient, d is the device thickness, e is the electric charge and $j_{D,in}$ and $j_{D,out}$ are the injected and extracted dark current densities, respectively. Since the measured dark current density for voltages below the built-in volltage is very low, $j_{D,out}$ can be neglected (all injected charge carriers recombine in the device) and it follows:

$$\frac{j_{D,in}}{ed} = kn_D^2. \tag{A.2}$$

Now, the temporal evolution of the charge carrier density after illumination is considered:

$$\frac{dn_L}{dt} = -kn_L^2 + (j_{in} - j_{out})/ed, \tag{A.3}$$

where n_L includes all charge carriers after illumination (dark and photogenerated) and j_{in} and j_{out} are the injected and extracted current densities after illumination. It

is assumed that the injected current density in the dark and after illumination is the same $j_{in} = j_{D,in} = edkn_D^2$. The extracted current density is related to the extracted charge in the time interval Δt under prebias conditions $Aj_{out} = \Delta Q_{\mathrm{pre}}/\Delta t$, with A the device area. This leads to the expression:

$$\frac{dn_L}{dt} = -kn_L^2 + kn_D^2 - \frac{\Delta Q_{\mathrm{pre}}}{eAd\Delta t} \quad \text{or} \quad \frac{dQ_{L,coll}}{dt} = -keAd(n_L^2 - n_D^2) - \frac{\Delta Q_{\mathrm{pre}}}{\Delta t}. \tag{A.4}$$

$Q_{L,coll} = eAdn_L^2$ includes all charge in the device after illumination. However, the experiment determines

$$Q_{\mathrm{coll}} = Q_{L,coll} - Q_{\mathrm{dark}} = eAd(n_L - n_D) \tag{A.5}$$

by subtracting the capacitive peak including Q_{dark}. Assuming that the dark charge is constant $\frac{dQ_{\mathrm{dark}}}{dt} = 0$ it can be written:

$$\frac{dQ_{\mathrm{coll}}}{dt} = -keAd(n_L^2 - n_D^2) - \frac{dQ_{\mathrm{pre}}}{dt}. \tag{A.6}$$

n_L is not known. However, rearranging Equation (A.5) to

$$\frac{Q_{\mathrm{coll}}}{eAd} + n_D = n_L \tag{A.7}$$

and squaring gives an expression for $n_L^2 - n_D^2$:

$$n_L^2 - n_D^2 = \left(\frac{Q_{\mathrm{coll}}}{eAd}\right)^2 + 2\frac{Q_{\mathrm{coll}}}{eAd}n_D. \tag{A.8}$$

Equations (A.8) and (A.6) lead to:

$$\frac{dQ_{\mathrm{coll}}}{dt} = -k\left(\frac{Q_{\mathrm{coll}}^2}{eAd} + 2Q_{\mathrm{coll}}n_D\right) - \frac{dQ_{\mathrm{pre}}}{dt}. \tag{A.9}$$

Using $Q_{\mathrm{dark}} = eAdn_D$, the iterative analysis Equation (4.5) is obtained:

$$Q_{\mathrm{coll}}(t_{\mathrm{d}}+\Delta t) = Q_{\mathrm{coll}}(t_{\mathrm{d}}) - [Q_{\mathrm{pre}}(t_{\mathrm{d}}+\Delta t) - Q_{\mathrm{pre}}(t_{\mathrm{d}})] - \frac{k}{eAd}[Q_{\mathrm{coll}}^2(t_{\mathrm{d}}) + 2Q_{\mathrm{coll}}(t_{\mathrm{d}})Q_{\mathrm{dark}}]\Delta t. \tag{A.10}$$

A.4 RC time analysis for P3HT:PCBM devices

annealed

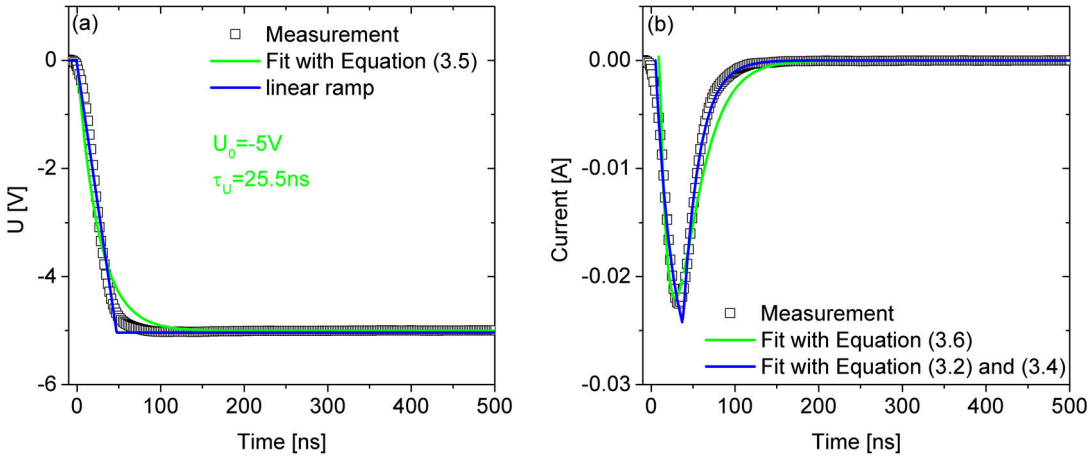

Figure A.3: Annealed device, 200 nm. (a) The measured voltage trace was approximated by a linear ramp (blue) and with an exponential function according to Equation (3.5) (green). The corresponding current transients are shown in (b). The approximation with the linear ramp and the fit with Equation (3.2) for the rising edge and Equation (3.4) for the falling edge give slightly better results than the fit with Equation (3.6), yielding the following parameters: $R = 70\Omega$, $C = 282$ pF, $RC = 19.7$ ns

as prepared

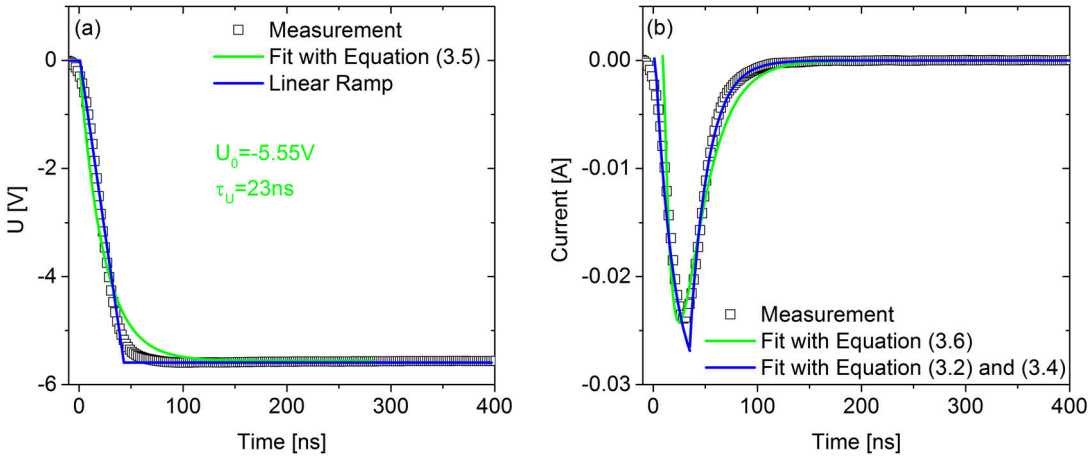

Figure A.4: As prepared device, 200 nm. Same analysis as above. Here, also the approximation with a linear ramp and subsequent fit with Equations (3.2) and (3.4) gives a better fit and more realistic results: $R = 70\Omega$, $C = 255$ pF, $RC = 17.8$ ns

A.5 J(E) for PTB7:PCBM electron-only devices

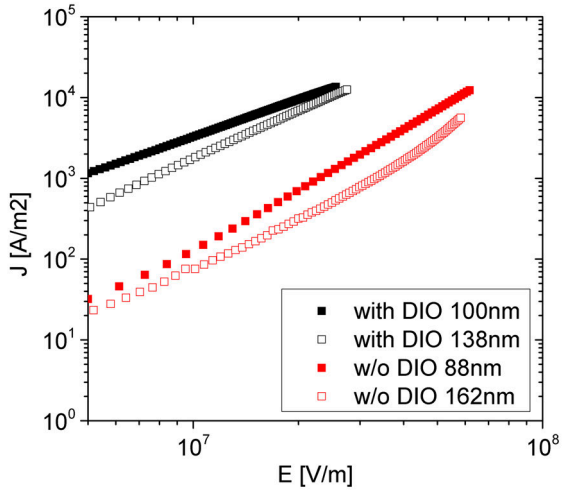

Figure A.5: The electron current density vs. electric field for two different layer thicknesses each scales with $1/d$ for both devices (with and w/o DIO) and can therefore be evaluated with Equation (4.8).

A.6 Influence of the delay between switch-off of the LEDs and application of the reverse bias in BACE experiments

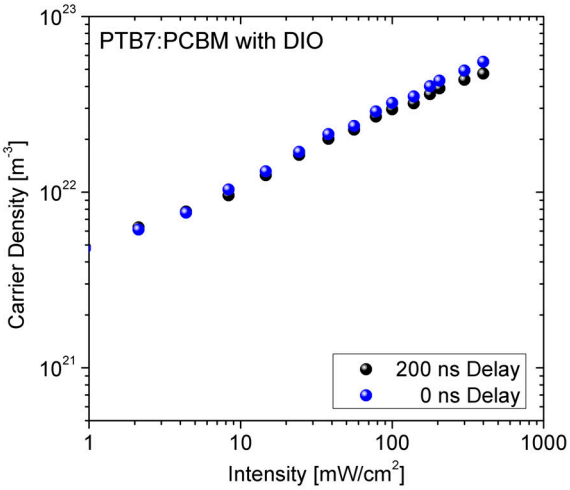

Figure A.6: Charge carrier density extracted in BACE with a 0 ns and 200 ns delay for PTB7:PCBM with DIO.

BACE experiments were performed with an either 0 ns or 200 ns delay between initiation of the LED switch-off and application of the reverse extraction bias. In

case of PTB7:PCBM blends with DIO, a longer delay leads to a slightly smaller amount of extracted charge particularly at high carrier densities, which is assigned to bimolecular recombination during the 200 ns delay. Hence, for blends with intermediate or high BMR rates it is important to start extraction immediatly after the LED switch.
In contrast, for annealed P3HT:PCBM no difference between the extracted carrier density is observed for the two different delay time.[193] Here, the low BMR coefficient limits the recombination losses during the delay. Furthermore, the amount of additional photogenerated charge during the 200 ns LED switch-off time is very small. A simple estimation confirms this assumption: For PTB7:PCBM with DIO (the blend with the highest generation rate) the generation rate at 1 sun (100 mW/cm^2) is approximately 1×10^{28} 1/m^{3}s. Assuming constant generation for 200 ns leads to a photogenerated carrier density of 2×10^{21} m^{-3}. This is more than one order of magnitude lower than the bulk carrier density at this illumination intensity.

A.7 Photocurrent transient with inhomogeneous carrier distribution

The steady state carrier distribution of a PTB7:PCBM device with DIO under one sun illumination, shown in Figure A.7 left, was fed into the transient simulation program. For the steady state simulation the same parameters as in Figure 5.3 were used. For the transient simulation, only the electrons were considered, which were extracted to the cathode with an extraction voltage of -3V. The integral of the arising photocurrent transient presented in Figure A.7 right is:

$$Q_{\text{int}} = 1.59 \times 10^{-10} \text{ C}$$

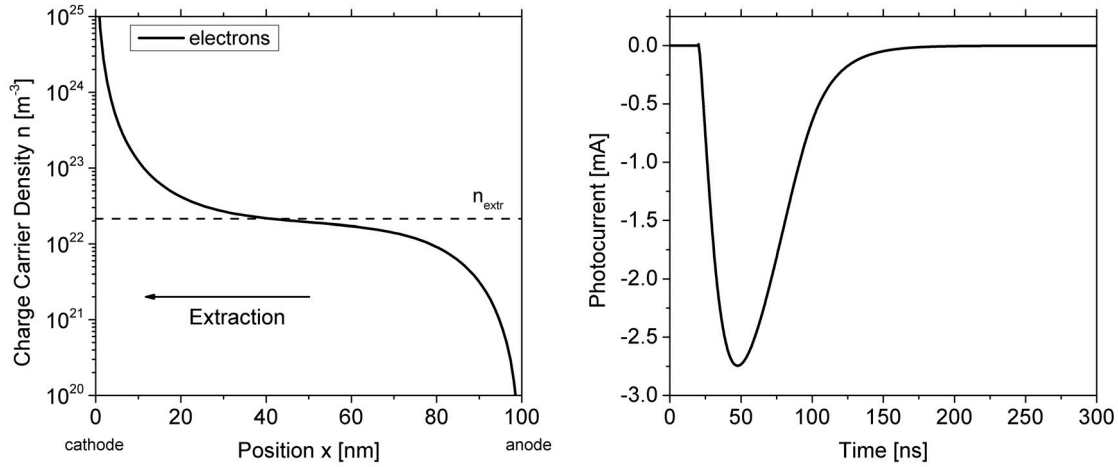

Figure A.7: Left: Steady state carrier distribution for a PTB7:PCBM device with DIO under one sun illumination (only electrons shown). Simulation parameters from Figure 5.3 (main text) were used. Right: Transient simulation of the photocurrent arising if electrons are extracted to the cathode. $V_{\text{extr}} = -3$ V, $\mu_e = 5 \times 10^{-4}$ cm^2/Vs, d=100 nm, A=1 mm^2.

For comparison, the extracted charge calculated from this distribution with Equation (5.3) and (5.4) is:

$$Q_{\text{int}} = 1.68 \times 10^{-10} \text{ C}$$

A.8 Determination of the effective bandgap in PTB7:PCBM devices

In order to determine the effective bandgap between the PTB7-HOMO and the PCBM-LUMO, the V_{OC} of the devices at multiple illumination intensities was analyzed as a function of the carrier density n using the fundamental approach:

$$V_{\text{OC}} = E_g + 2kT * \ln\left(\frac{n}{N}\right), \tag{A.11}$$

see reference [193], with the bandgap E_g and density of states N. For that purpose BACE measurements have been performed. The results are shown in Figure A.8. Using a density of states of $N = 10^{27}$ m^{-3} (the same as used in the simulations), the effective bandgaps can be estimated to 1.24 eV in the devices with DIO and 1.32 eV w/o DIO which is in very good agreement to 1.27 eV or 1.36 eV as used in the simulation.

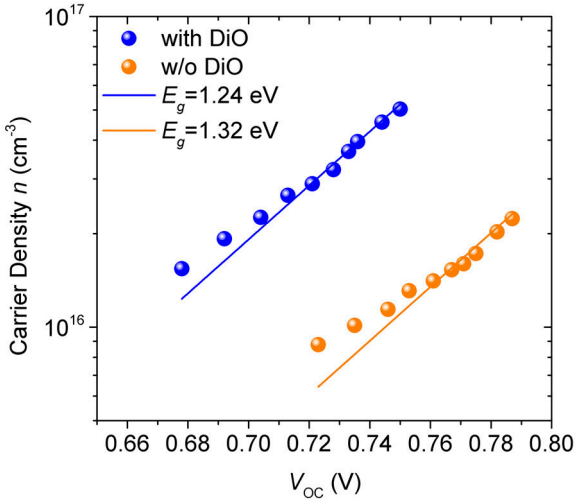

Figure A.8: Carrier density n vs. open circuit voltage V_{OC} as determined with BACE.

A.9 Influence of contact selectivity on decay dynamics

Transient simulations were performed for a 200 nm layer between symmetric contacts ($E_{\text{LUMO}} = -3.6$ eV, $E_{\text{HOMO}} = -4.8$ eV, $E_{\text{anode}} = E_{\text{cathode}} = -4.2$ eV). The time delay between the homogeneous insertion of electrons and holes and the application of the extraction bias of -5 V was varied between 20 ns and 10 μs. During the delay the bias was $V_{\text{pre}} = 0$ V. The integral of the total current transient (during delay and collection time) was evaluated as described in Section 4.3 and plots of

Q_{coll} and Q_{pre} as a function of the delay time were generated (Figure A.9). In both simulations the BMR coefficient was set to $k = 5 \times 10^{-18}$ m^{3}s^{-1}. Also, in both simulations the charge carriers were allowed to diffuse out of the device, while injection of charge carriers was blocked.
Now, in the first case selective contacts were assumed, meaning that electrons were only allowed to leave the device at the cathode and holes at the anode (black symbols). In the second case, both carriers were allowed to leave the device at both contacts, simulating non-selective contacts (red symbols). Figure A.9 shows, that in the case of non-selective contacts the decay of the carrier density in the device is much faster. Furthermore, the intergrated charge during the delay (Q_{pre}) is zero since the electron and hole diffusion currents cancel each other out. Both decay curves were fitted with bimolecular recombination according to Equation (4.4), yielding $k = 3 \times 10^{-18}$ m^{3}s^{-1} for selective and $k = 3 \times 10^{-17}$ m^{3}s^{-1} for non-selective contacts. In case of non-selective contacts, the apparent BMR coefficient is one order of magnitude higher than the true recombination coefficient.

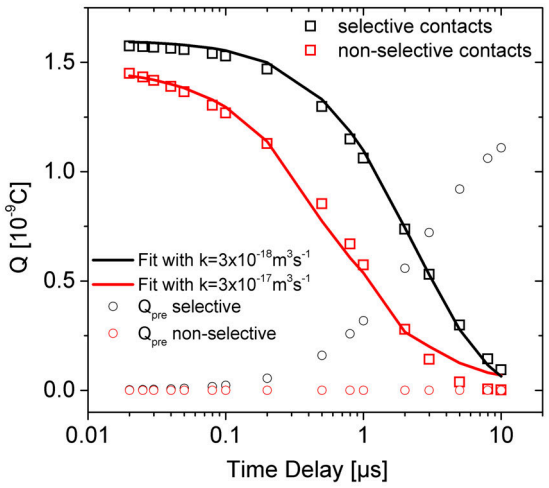

Figure A.9: Drift diffusion simulation (symbols) of the decay dynamics after a homogeneous inserted carrier density in case of selective and non-selective contacts. Simulation parameters were: $d = 200$ nm, $E_{\text{LUMO}} = -3.6$ eV, $E_{\text{HOMO}} = -4.8$ eV, $E_{\text{anode}} = E_{\text{cathode}} = -4.2$ eV, $V_{\text{pre}} = 0$ V, $V_{\text{coll}} = -5$ V, $k = 5 \times 10^{-18}$ m^{3}s^{-1}, $\mu_e = \mu_h = 5 \times 10^{-4}$ cm^2/Vs. Solid lines are BMR fits with Equation (4.4).

List of Publications

1. **J. Kniepert**, M. Schubert, J. C. Blakesley, D. Neher, "Photogeneration and Recombination in P3HT/PCBM Solar Cells Probed by Time-Delayed Collection Field Experiments", *J. Phys. Chem. Lett.*, 2, 700 **(2011)**

2. S. Albrecht, W. Schindler, J. Kurpiers, **J. Kniepert**, J. C. Blakesley, I. Dumsch, S. Allard, K. Fostiropoulos, U. Scherf, D. Neher, "On the Field Dependence of Free Charge Carrier Generation and Recombination in Blends of PCPDTBT/PC70BM: Influence of Solvent Additives", *J. Phys. Chem. Lett.*, 3, 640 **(2012)**

3. S. Albrecht, S. Janietz, W. Schindler, J. Frisch, J. Kurpiers, **J. Kniepert**, S. Inal, P. Pingel, K. Fostiropoulos, N. Koch, D. Neher, "Fluorinated Copolymer PCPDTBT with Enhanced Open-Circuit Voltage and Reduced Recombination for Highly Efficient Polymer Solar Cells", *J. Am. Chem. Soc.*, 134, 14932 **(2012)**

4. I. Lange, **J. Kniepert**, P. Pingel, I. Dumsch, S. Allard, S. Janietz, U. Scherf, D. Neher, "Correlation between the Open Circuit Voltage and the Energetics of Organic Bulk Heterojunction Solar Cells", *J. Phys. Chem. Lett.*, 4, 3865 **(2013)**

5. A. Foertig, **J. Kniepert**, M. Gluecker, T. J. K. Brenner, V. Dyakonov, D. Neher, C. Deibel, "Nongeminate and Geminate Recombination in PTB7:PCBM Solar Cells", *Adv. Funct. Mater.*, 24, 1306 **(2014)**

6. **J. Kniepert**, I. Lange, N. van der Kaap, L. J. A. Koster, D. Neher, "A Conclusive View on Charge Generation, Recombination, and Extraction in As-Prepared and Annealed P3HT:PCBM Blends: Combined Experimental and Simulation Work", *Adv. Energy Mater.*, 4, **(2014)**

7. I. Lange, S. Reiter, **J. Kniepert**, F. Piersimoni, M. Pätzel, J. Hildebrandt, T. Brenner, S. Hecht, D. Neher, "Zinc oxide modified with benzylphosphonic acids as transparent electrodes in regular and inverted organic solar cell structures", *Appl. Phys. Lett.*, 106, 113302 **(2015)**

8. **J. Kniepert**, I. Lange, J. Heidbrink, J. Kurpiers, T. J. K. Brenner, L. J. A. Koster, D. Neher, "Effect of Solvent Additive on Generation, Recombination, and Extraction in PTB7:PCBM Solar Cells: A Conclusive Experimental and Numerical Simulation Study", *J. Phys. Chem. C*, 119, 8310 **(2015)**

9. D. Bartesaghi, I. Perez, **J. Kniepert**, S. Roland, M. Turbiez, D. Neher, L. J. A. Koster, "Competition between recombination and extraction of free charges determines the fill factor of organic solar cells", *Nature Comm.*, 6 **(2015)**

Danksagung

Ich möchte mich bei allen Menschen bedanken, die auf verschiedenste Weise zur Entstehung und Fertigstellung dieser Arbeit beigetragen haben.

An erster Stelle steht hier natürlich Prof. Dieter Neher, dem ich herzlich für die Möglichkeit und das Vertrauen danke, die Arbeit in seiner Forschungsgruppe anfertigen zu dürfen. Dank der unzähligen wissenschaftlichen Diskussionen, deiner Ideen und Anregungen habe ich sehr viel über organische Solarzellen im Speziellen und das wissenschaftliche Arbeiten im Allgemeinen gelernt. Insbesondere das kritisches Hinterfragen auch kleinster Details haben einen relevanten, wissenschaftlichen Beitrag ermöglicht.

An zweiter Stelle gilt mein herzlicher Dank Prof. Elizabeth von Hauff und Prof. Carsten Deibel für die Übernahme der Gutachten dieser Arbeit.

Der gesamten Arbeitsgruppe Physik weicher Materie - und besonders den Mitdoktoranden Patrick, Marcel, Robert, Sahika, Steve, Ilja, Jona, Steffen, Andreas, Christian und Roberta - danke ich für die äusserst angenehme Arbeitsatmosphäre und die fortwährende gegenseitige Unterstützung und Hilfe bei Problemen. Die vielen wissenschaftlichen Diskussionen, aber auch vor allem der ausser-wissenschaftliche Austausch haben Büro und Labor zu Orten gemacht, an denen man gerne arbeitet. Unvergessen bleiben gemeinsame Konferenzbesuche ("Klassenfahrten") und sportliche Aktivitäten von Kanu fahren über Segeln, Golfen und Bogengolfen - was kommt als nächstes?

Mein besonderer Dank gilt Frank Jaiser - der mehr als nur einmal Retter in der Not war und bei Panikattacken (z.B. wenn sich eine Woche vor Abgabe das Dokument nicht mehr öffnen lässt) stets sofort zur Stelle war und **immer** alles wieder in Ordnung gebracht hat. Ohne dich wären inzwischen vermutlich alle Daten im Nirvana verschwunden.

Ebenfalls danke ich APu für die Unterstützung bei allen technischen und elektronischen Fragen und besonders dafür, dass du alle Probleme immer sofort mit höchster Motivation angegangen bist - geht nicht, gibt's bei dir nicht!

Desweiteren danke ich Jona für die kontinuierlichen Verbesserungen des TDCF Aufbaus und Messprogramms die wirklich das bestmögliche aus der Messmethode herausgeholt haben, die anschliessende Hilfe und Einarbeitung wenn ich dann ahnungslos davor sass und natürlich für eine gute Büronachbarschaft; Thomas für die wissenschaftlichen Diskussionen, die mich sehr weitergebracht haben, unsere Kaffeerunden mit fachsimpeln übers Häuserbauen und natürlich für das Korrekturlesen der Arbeit; Tobias für die spontane Übernahme der letzten Ex-4 Übungen, damit ich doch noch die Arbeit zu Ende schreiben kann; und Elke für allen Papierkram,

das Organisatorische und die Versorgung mit Süssigkeiten und Büroartikeln.

Prof. Jan Anton Koster danke ich für die Bereitstellung des Simsalabim Simulationsprogramms für die Steady State Simulationen, das einen wesentlichen Teil meiner Arbeit ausmacht und mein Verständnis weit voran gebracht hat und für die Diskussionen über die Ergebnisse. Niels van der Kaap danke ich für die Simulationen für das P3HT:PCBM Paper. Sebastian Bange danke ich für die Bereitstellung des transienten Simulationsprogramms und für die Unterstützung bei der Einarbeitung.

Ein besonders grosses Dankeschön geht an meine Mutter - Eveline Kniepert - für die vielen Stunden der Kinderbetreuung, so dass ich mit ruhigem Gewissen im Büro sitzen und an meiner Arbeit schreiben konnte. Ohne dich wäre die Arbeit nicht fertig geworden!

Und natürlich an Aaron - meinen wunderbaren Sohn - der mir jeden Tag zeigt, was im Leben wirklich wichtig ist. Das wirst du erst später lesen und verstehen können - diese Arbeit ist für dich!

An letzter Stelle, aber in Gedanken zuerst, danke ich Ilja - für die Erkenntnis, dass Steady State doch gar nicht so schlecht ist. Du bist ein grossartiger Wissenschaftler, unschätzbarer Kollege, Freund, Mentor, Partner, ein wundervoller Vater und natürlich (glücklicherweise) ein sehr talentierter Häuslebauer. Danke für alles!

Eigenständigkeitserklärung

Ich erkläre hiermit, dass ich diese Arbeit selbstständig verfasst und keine anderen als die angegebenen Hilfsmittel benutzt habe. Diese Arbeit wurde an keiner anderen Hochschule eingereicht.

Potsdam, den 11.09.15

Juliane Kniepert